Technische Universität München
TUM School of Engineering and Design

Unsteady Interference Effects on Passenger Vehicles in Open-Jet Wind Tunnels

Jonas Sebald

Vollständiger Abdruck der von der TUM School of Engineering and Design der Technischen Universität München zur Erlangung eines

Doktors der Ingenieurwissenschaften (Dr. Ing.)

genehmigten Dissertation.

Vorsitz: Priv.-Doz. Dr.-Ing. habil. Stefan Adami / Prof. Dr. Christian Stemmer

Prüfer*innen der Dissertation:

1. apl. Prof. Dr.-Ing. habil. Thomas Indinger
2. Assoc. Prof. Dr. Takuji Nakashima

Die Dissertation wurde am 25.07.2023 bei der Technischen Universität München eingereicht und durch die TUM School of Engineering and Design am 30.11.2023 angenommen.

Technical University of Munich
TUM School of Engineering and Design
Chair of Aerodynamics and Fluid Mechanics

Unsteady Interference Effects on Passenger Vehicles in Open-Jet Wind Tunnels

Jonas Sebald

Preface

As a research associate and Ph.D. student at the Chair of Aerodynamics and Fluid Mechanics of the Technical University of Munich, I dedicated several years to completing this dissertation.

I would like to express my appreciation to my supervisor, apl. Prof. Dr.-Ing. habil. Thomas Indinger, for his unwavering encouragement and support throughout the entire project. Under his guidance, I could dive deeply into various of research areas and achieve meaningful results.

I am also grateful to my esteemed colleagues from the industry partner Audi AG, Dr. Moni Islam and Dr.-Ing. Marco Kiewat, for their valuable contributions. Their insights into the field of vehicle aerodynamics engineering and their encouragement to focus on wind tunnel interference effects were instrumental in shaping the main topic of my Ph.D.

I extend my gratitude to my fellow researchers in the vehicle aerodynamics research group at the Chair of Aerodynamics and Fluid Mechanics of the Technical University of Munich. It was a pleasure collaborating with all of you. I would especially like to thank Jan Reiß and Philipp Schlichter. Our endless discussions, the many hours we spent in the wind tunnel and your support were incredibly precious.

I want to acknowledge the immense support and motivation provided by my family and friends, particularly my parents, Kirsten and Walter, who have been a constant source of encouragement in everything I do.

Lastly, I am profoundly grateful to my girlfriend, Lisa, the most important person in my life. Without her support, this work would not have been possible.

Abstract

A lot of research has been conducted to investigate the wind tunnel interference effects and their correction. To this date, a lot of this research is based on time-averaged results, like pressure distributions in the test section. Little research focuses on interference effects based on time-resolved flow characteristics, like frequencies of vortical structures or the fluctuation intensity in the test section. Especially in open-jet wind tunnels for automotive applications, the low-frequency buffeting caused by aeroacoustics resonance effects is a problem. These resonance effects can not only affect the structural integrity of the wind tunnel building but can also have an effect on the flow field around the tested vehicle.

This dissertation will give new insights into the interference between the wind tunnel eigenmodes and the flow around the vehicle. The resonance effects in the wind tunnel are present because of the wind tunnel duct and compressible aeroacoustic phenomena. A novel boundary condition for the CFD setup adds the wind tunnel eigenmodes to the simulation without the need to simulate the whole wind tunnel duct compressible.

This new CFD setup produces promising results for a generic test case and, therefore, it is used to enhance the numerical wind tunnel flow. Firstly, crucial deviations of the time-resolved flow field between the current CFD setup and experimental wind tunnel results are shown. The new boundary condition is then used to optimise the numerical flow. In the optimisation process, different approaches for the boundary condition, which introduces the wind tunnel modes into the CFD domain, are analysed. Different filtering and scaling methods of the wind tunnel fluctuations are tested and some flow phenomena described in previous literature about wind tunnel effects can be reproduced with the numerical simulation. In addition to that, it can be seen which frequencies have the most influence on specific flow phenomena. These are not only new insights into this research topic, but it also supports previous research hypothesis. After the optimisation process, the numerical wind tunnel flow has a high accordance with the experimental wind tunnel flow.

With the new method, the difference between a vehicle in an ideal numerical box flow and the flow in the numerical wind tunnel with the exact flow phenomena found in the experimental wind tunnel can be analysed. With this result, the effect of the wind tunnel modes on vehicle tests can be determined. Also, it can be shown which frequencies are coupled to the vortical structures of the vehicle and how the wind tunnel modes influence them. The results of this chapter show that it is essential to include the wind tunnel modes in numerical simulations. Especially when a comparison to the experimental flow is conducted. Furthermore, this new method enables further research about vortical structures in the wake of the vehicle.

Abbreviations

AAWT	Audi Aeroacoustics Wind Tunnel
ARC	Active Resonance Control System
CFD	Computational Fluid Dynamics
DES	Detached Eddy Simulation
DDES	Delayed Detached Eddy Simulation
DNS	Direct Numerical Simulation
FFT	Fast Fourier Transformation
LES	Large Eddy Simulation
PSD	Power Spectral Density
RANS	Reynolds-averaged Navier-Stokes equations
WTA	Wind Tunnel A of TU Munich

Nomenclature

Latin Letters

A	$[\ V^2\ ]$	King's Law parameter
A_I	$[\ m^2\ ]$	inlet area
A_N	$[\ m^2\ ]$	nozzle outlet cross-section
A_F	$[\ m^2\ ]$	frontal area
b	$[\ m\ ]$	nozzle exit width
B	$[\ \frac{V^2 s}{m}\ ]$	King's Law parameter
c	$[\ \frac{m}{s}\ ]$	speed of sound
D	$[\ m\ ]$	cylinder diameter
D_h	$[\ m\ ]$	hydraulic nozzle diameter
f	$[\ Hz\ ]$	frequency
$f_{r,d}$	$[\ Hz\ ]$	resonance frequency of the wind tunnel duct
$f_{r,ts}$	$[\ Hz\ ]$	resonance frequency of the test section chamber
$f_{r,ts\text{-}c}$	$[\ Hz\ ]$	cavity-like resonance frequency of the test section chamber
h	$[\ m\ ]$	nozzle exit height
H_C	$[\ m\ ]$	cylinder height
k	$[\ \frac{m^2}{s^2}\ ]$	turbulent kinetic energy
L	$[\ m\ ]$	wind tunnel duct length
L_{jet}	$[\ m\ ]$	wind tunnel jet length
$l_{x,y,z}$	$[\ m\ ]$	dimensions of the test section chamber
l_n	$[\ m\ ]$	Helmholtz-resonator neck length
l_T	$[\ m\ ]$	test section length
l_{wheel}	$[\ m\ ]$	wheelbase
n	$[\ -\ ]$	King's Law parameter
n_w	$[\ -\ ]$	number of half-wavelengths
Re	$[\ -\ ]$	Reynolds number
r_n	$[\ m\ ]$	Helmholtz-resonator neck radius

St	[-]	Strouhal number
t	[s]	time
Tu	[-]	turbulence intensity
u	$[\frac{m}{s}]$	wind speed
V	[m^3]	section chamber volume

Greek Letters

ρ	$[\frac{kg}{m^3}]$	density
ν	$[\frac{m^2}{s}]$	kinematic viscosity
$\tilde{\nu}$	$[\frac{m^2}{s}]$	modified turbulent viscosity
Φ	$[\frac{kg}{s}]$	mass flow of cell faces

Content

1 Introduction

For decades, aerodynamicists have aspired to reduce the aerodynamic drag of vehicles. Reducing the aerodynamic drag is a key component to enhancing the efficiency of a vehicle. This applies to all vehicles like trains, trucks and passenger vehicles. Especially for production passenger vehicles, it is important to have high driving efficiency. In times when resources and energy sources are very limited and costly, the development of efficient vehicles has a great impact. A lot of development and optimisations are needed to get an efficient vehicle with low aerodynamic drag. This optimisation takes place in wind tunnels but is also supported by the help of numerical simulations. Both development tools have their advantages and must be linked together in the optimisation process of the vehicle. But these tools also have some disadvantages, which need to be taken into account when choosing a certain tool for a specific task. One disadvantage is the interference effects of a wind tunnel, which potentially distort the measurement result. The disadvantage of a numerical simulation is the result quality, in the sense of deviations from the real physical result of a wind tunnel test. This dissertation will give an overview of the latest research on wind tunnel interference effects, focusing mainly on time-resolved flow phenomena and resonance effects. Furthermore, the quality of time-resolved numerical results is significantly improved. This helps to reconcile wind tunnel tests and numerical simulations to develop efficient vehicles.

1.1 Motivation

A lot of research has been conducted to investigate the wind tunnel interference effects and their correction. The correction is needed to factor out any wind tunnel effects in the measurement results. In the following chapter, an overview of the well-known wind tunnel interference effects and the corresponding research is given. To this date, a lot of this research is based on time-averaged results, like pressure distributions in the test section. Little research has been conducted on interference effects based on time-resolved flow characteristics, like frequencies of vortical structures or the fluctuation intensity in the test section. Especially in open-jet wind tunnels for automotive applications, the low-frequency buffeting caused by aeroacoustics resonance effects is a problem. These resonance effects with a specific frequency depend on characteristic dimensions of parts of the wind tunnel and are called wind tunnel eigenmodes. These resonance effects can not only affect the structural integrity of the wind tunnel building but can also have an effect on the flow field around the tested vehicle. This will be shown in the next chapter in more detail. Only little research has been conducted about the interference between the low-

frequency wind tunnel eigenmodes and the vortical structures arising from flow separations at the vehicle.

This dissertation will give new insights into the interference between the wind tunnel eigenmodes and the flow around the vehicle. The resonance effects in the wind tunnel are present because of the wind tunnel duct and compressible aeroacoustic phenomena. That‘s where the problem begins: to save computational costs in vehicle development, only a partial model of the physical wind tunnel can be simulated and the used solver is based on an incompressible assumption. Therefore a method is needed which adds the wind tunnel eigenmodes to the simulation without the need to simulate the whole wind tunnel duct compressible.

Then the new method and the correctly predicted time-resolved wind tunnel flow can be used to evaluate the influences the wind tunnel modes have on the flow around the vehicle.

1.2 Transient Interference Effects in Automotive Wind Tunnels

The purpose of automotive wind tunnel tests and measurements is to optimise the aerodynamic characteristics of a vehicle while driving on the street. In the wind tunnel, it is possible to simulate the conditions of the driving vehicle, like the wind speed and the angle of attack, in a controllable environment. This helps to investigate various driving situations. Automotive wind tunnels have a closed loop duct. The duct contains a fan and the accelerated air is transported with the help of turning vanes to the test section. In front of the test section, a nozzle accelerates the air to the final wind speed needed for the measurement. The investigated vehicle is positioned in the test section. The test section in automotive wind tunnels is inside an open room (plenum). Therefore, between the fast-moving jet coming from the nozzle and the stationary air of the plenum, a shear layer results. After the test section, the air is collected by the collector, decelerated by the diffusor and guided back to the fan by turning vanes. With the addition of a rolling road system, which simulates the relative velocity between the vehicle and the street, the flow condition in the wind tunnel is very similar to the flow condition on the street. An exemplary layout of an automotive wind tunnel is depicted in Figure 6. However, the flow condition in the wind tunnel is not completely identical to the street condition. Various effects come into play here. Effects like traffic and other vehicles driving near the investigated vehicle or atmospheric wind conditions are causing a certain level of turbulence in the air. These effects found on the street deviate from the wind tunnel flow, which is assumed as an ideal flow with a low level of turbulence and a constant wind speed. Various investigations are conducted on the influence of traffic and atmospheric wind conditions on wind tunnel results. Cogotti [1] summarizes

numerous investigations and shows a device for the wind tunnel which can simulate the traffic and atmospheric wind for specific scenarios. In this presented dissertation, the focus is not on the effects shown in [1] and the flow around the vehicle is considered without traffic and atmospheric wind. Nevertheless, these deviations between street driving and wind tunnel tests should be mentioned to get a complete overview. Another important deviation between the street driving and wind tunnel tests is the wind tunnel and its geometry itself. Compared to the almost infinite room for the air on the street, the nozzle and the test section of the wind tunnel limit the flow around a vehicle. Because of this limitation of the flow, different effects can be observed in the wind tunnel, which are causing different deviations in the wind tunnel flow compared to the flow on the street. These effects are the focus of this work and a detailed overview of the state of the art will be given.

In the last decades, a lot of research has been conducted regarding interference effects in wind tunnels and their correction. Some of the first results are derived from Lock [2] and Glauert [3], who investigated the interference effects in closed-wall and open-jet test sections for aeronautical studies. One of the first investigations on open-jet wind tunnel interference effects and their correction for automotive applications are conducted by Mercker and Wiedemann [4]. In the work of [4], the main interference effects of wind tunnels on tested vehicles are described. Additionally, they give correction formulae to compensate for the interference effects of the measured aerodynamic forces. As mentioned before, the flow in a wind tunnel needs to be as similar to street conditions as possible. Due to the limited size of a wind tunnel, the flow around a vehicle behaves differently in the wind tunnel compared to the street condition. These deviations have to be corrected for the wind tunnel measurements. These differences are summarized by [4] with five interference effects (1-5) and will be described in the following.

The jet-expansion effect (1) is caused by the limited size of the nozzle and therefore the limited size of the jet flowing out of the nozzle. When the finite jet, with its limited size, flows into the test section with a vehicle positioned there, the jet creates a shear layer and is deflected by the vehicle. In the shear layer, the outer streamline of the jet has to correspond to the ambient pressure of the test section. Since the distance from the outer streamline to the vehicle is finite in the wind tunnel, a greater pressure is present at the outer distance of the finite jet compared to the pressure for the same distance from the vehicle in an infinite jet, like on the street. The curvature of the streamline of the deflected jet has to increase to balance the ambient pressure at the outer streamline. This increased curvature lets the jet expand and the outer streamline moves further away from the vehicle. With the greater volume of the jet, the velocity in the jet around the vehicle decreases to fulfil the continuity of the flow. With the decreased velocity around the vehicle, the aerodynamic drag measured is too low. Furthermore, this expansion of the jet can be increased by the jet-deflection effect (2). The closer the vehicle is positioned to the nozzle, the greater the deflection of the jet.

Another interference effect is caused by the nozzle blockage (3). When a vehicle is positioned near the nozzle, the pressure region in front of the vehicle reaches into the nozzle. This pressure region in the nozzle partially displaces the nozzle flow and is considered as a blockage effect inside of the nozzle. Due to the displacement of the flow, the velocity in the nozzle is increased and the distribution of the wind speed across the nozzle cross-section is altered. This leads to different aerodynamic force measurement results compared to the free stream of the nozzle. Similar to the nozzle blockage effect is the collector blockage effect (4). The flow inside of the collector is displaced by the wake of the vehicle and therefore similar problems as with the nozzle blockage occur.

The last interference effect is the horizontal buoyancy in the test section (5). The horizontal buoyancy is caused by a pressure gradient in the test section from the nozzle to the collector. This pressure gradient originates at the nozzle and in front of the collector. From the nozzle onwards, an increase in pressure can be observed when the static pressure in the jet at the nozzle exit cannot sufficiently adapt to the ambient pressure in the test section. At the collector, the increase in pressure is caused by the decelerating flow in front of the collector. This decrease in wind speed leads to a higher static pressure. This pressure gradient can be measured in the empty test section. The increased pressure in front of the vehicle and behind it leads to different aerodynamic forces compared to an ideal flow without the pressure gradient.

The five inference effects (1-5) described by [4] are schematically visualized in Figure 1.

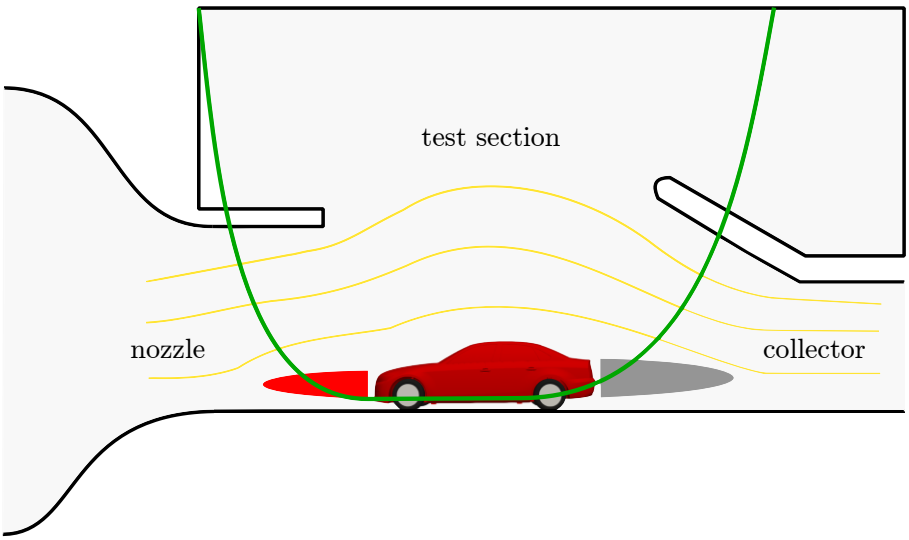

Figure 1: Schematic visualization of wind tunnel interference effects. Orange: jet-expansion (1) and jet-deflection (2), red: nozzle blockage (3), grey: collector blockage (4), green: pressure gradient (5).

Based on the work of [4], further research has been conducted to optimise the correction methods. The nozzle blockage correction method has been investigated and optimised over the past years, like in Mercker et al. [5] and Wickern et al. [6]. The influence of the pressure gradient on the vehicle and on its wake has been investigated by Mercker et al. [7] and Mercker et al. [8]. Additionally, the influence of boundary layer suction in front of the test section on the pressure gradient has been investigated by Wickern et al. [9]. In Wickern [10], an approach to a self-correcting wind tunnel by balancing different blockage and pressure gradient effects is given. These correction methods and interference effects are based on the assumption of a stationary constant flow in the wind tunnel. In this work, the focus is on transient flow phenomena in the wind tunnel and their influence on the vehicle. Nevertheless, the aforementioned interference effects are important to get an overview of all potential deviations between wind tunnel tests and street conditions. For further information about the stationary time-averaged interference effects and correction methods in the wind tunnel and a more detailed literature overview, the reader is referred to Wickern [11] and Collin [12].

Especially the aforementioned empty test section gradient effects are influenced by the temporal development and characteristics of the shear layer. The shear layer itself is a highly unsteady flow phenomenon and originates at the nozzle exit, where the fast flow of the jet meets the almost stationary flow of the test section chamber. The flow separation process at the nozzle exit and the temporal development of the shear layer have a great impact on the flow characteristics in the test section. Next to the influence on gradient effects in the test section, the flow separation and the shear layer can cause resonance effects in the wind tunnel. These resonance effects lead to low-frequency buffeting in the wind tunnel, which is not only a problem for the structural stability of the building [13] or aeroacoustics measurements, but also influences aerodynamic measurements. These transient flow phenomena in an open-jet wind tunnel and their effect on aerodynamic vehicle measurements are the focus of this work. In the following, an overview of the latest research regarding transient nozzle and shear layer investigations as well as open-jet wind tunnel buffeting and its influence on the aerodynamic testing of a vehicle are presented.

One of the first thorough investigations of the low-frequency buffeting of an open-jet wind tunnel was conducted in 1997 by Holthusen et al. [13]. The investigation was driven by the fact that the German-Dutch Wind Tunnel had problems with structural vibrations at high wind speeds. These vibrations were caused by the wind tunnel buffeting. They were so severe that they had to reduce the maximum wind speed of the wind tunnel tests. The goal of their investigation is to find a way to reduce wind tunnel buffeting. For that, the wind tunnel buffeting must be understood. In [13], the main mechanisms are described. The rotation of the fan creates periodic pressure fluctuations in the whole wind tunnel duct. This periodic fluctuation is called the blade passing frequency and is present in the whole wind tunnel duct. Furthermore, the vortex shedding at the nozzle

exit creates a specific fluctuation frequency. The vortices separating at the nozzle exit create large-scale structures, which are transported downstream in the shear layer of the open-jet test section causing pressure fluctuations. When these vortical structures hit the collector at the end of the test section, an edge-tone can occur. This tone can cause a feedback effect at the nozzle exit. This effect additionally forces and amplifies the vortex shedding. Like the flow through a tube, the flow through the wind tunnel duct has a resonant frequency. In the case that the vortex shedding frequency at the nozzle coincidences with the resonant frequency of the wind tunnel duct, a resonance in the wind tunnel occurs. Holthusen et al. [13] show that with specific geometries, so-called tetrahedrons, in the nozzle exit, the structural vibrations and therefore the resonance of the wind tunnel buffeting can be reduced. They also show that the shear layer with the tetrahedrons is thinner and the wind speed of the jet increases by 6% for a constant fan speed. Especially the last findings will be of high interest in the following and in this research work in general.

In 1999 Arnette et al. [14] investigated low-frequency buffeting of open-jet wind tunnels for the new Chrysler wind tunnel. They show that the low-frequency pulsations of the test section are due to the cavity-like resonance effect in the test section and the tube-like resonance effect of the whole wind tunnel duct. They also show that when the shear layer structures are fluctuating with a frequency which coincidences with one of the resonance frequencies of the test section or the wind tunnel duct, the buffeting increases. They also show that the resonant frequencies are linked to the dimensions of the test section, the jet length and the collector geometry, and that the resonances for certain wind speeds can be altered by changing the dimensions of the test section and the wind tunnel duct.

For a better understanding, Wickern et al. [15] investigated in 2000 the low-frequency wind tunnel buffeting in a model- and a full-scale wind tunnel. They agreed on the basic theory that wind tunnel buffeting occurs when the frequency of the vortical structures of the jet shear layer coincidences with the resonant frequencies of the wind tunnel geometry. Instability waves can be observed at a free jet exiting a nozzle. This also applies to the jet of an automotive wind tunnel. These instabilities are evolving to vortical structures in the shear layer around the open jet in the test section. The vortical structures are mainly axisymmetric around the open jet.

In Figure 2, the ring vortex around the jet in the shear layer of the 3/4 open jet of an automotive wind tunnel is visualized with arrows indicating the direction of rotation. This picture should be seen as a schematic illustration of the periodic vortical structures for a better understanding.

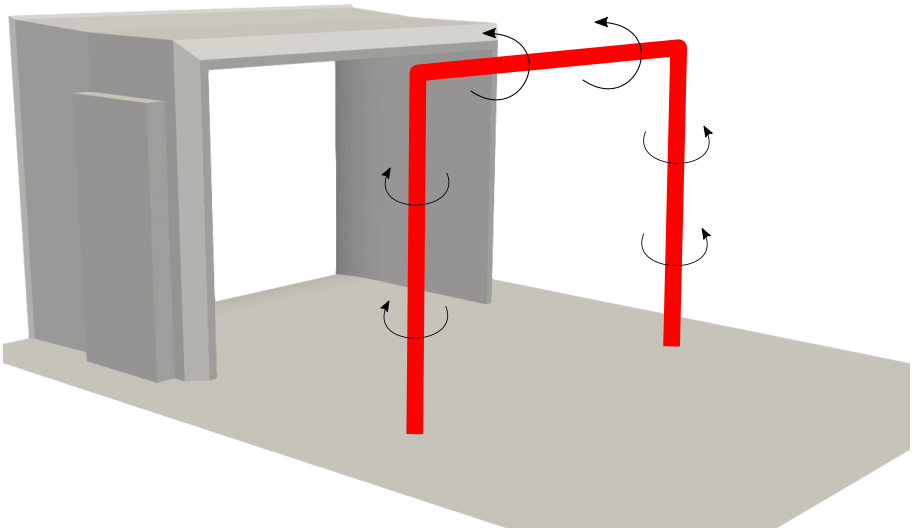

Figure 2: Schematic illustration of the ring vortex (red) of the shear layer, based on Wickern et al. [15].

These vortical structures of, e.g. Figure 2 of the ring vortex, can be described with a specific Strouhal number, similar to von Karman vortices. The frequency of the structures in the shear layer is dependent on the hydraulic diameter of the nozzle and the wind speed in the core of the jet. With the hydraulic diameter D_h of

$$D_h = \frac{2 \cdot h \cdot b}{h+b} \tag{1}$$

with h being the height of the nozzle and b being the width of the nozzle, the Strouhal number for the vortex shedding at the nozzle is defined as

$$St = \frac{f \cdot D_h}{u} \tag{2}$$

In equation (2), f is the vortex shedding frequency at the nozzle exit and u the wind speed in the core of the jet. Wickern et al. [15] suggest that the Strouhal number of the vortex shedding for an automotive wind tunnel with a 3/4 open jet should be $\sqrt{2}$ times smaller than the Strouhal number of a completely open jet. This is due to the floor of the test section, which is needed for the road simulation for the wind tunnel tests. The floor is the reason that in automotive wind tunnels, there are no complete open jets but only 3/4 open jets. Taking the floor of the test section as a mirror of an image approach of the potential flow into account, an open jet with double the cross-section is the result. For the original cross-section, the Strouhal number must be smaller by $\sqrt{2}$. With this

considered, the Strouhal number of the vortex ring is at around St=0.34. Usually, the fluctuations in a pressure or velocity spectrum have a broad maximum at around St=0.34. But when there is a resonance mechanism in the wind tunnel flow, the broad maximum changes to a sharp peak in the spectrum. The following resonance mechanisms can be present in an automotive wind tunnel.

In [15], similar resonance effects of a wind tunnel are stated as in the investigations of [13] and [14]. The test section chamber and the wind tunnel duct offer the opportunity for acoustic resonances. The test section chamber can act like a Helmholtz resonator, with the nozzle or the collector acting as a resonator. The test section chamber can also be looked at as a cavity-type resonance. The wind tunnel duct has resonance characteristics like a tube. When the vortex shedding at the nozzle coincides with a resonant frequency of the tunnel duct, a standing pressure wave is present in the wind tunnel duct. This pressure wave leads to an additional excitement of the vortex shedding at the nozzle exit, which is thereby intensified. The resonance frequency of the wind tunnel duct is calculated like an organ pipe resonance along the pipe axis with neglected corrections for the ends of the wind tunnel duct. The resonance frequency is dependent on the duct length and is characterized by the standing waves along the duct axis. The eigenfrequency of the duct is defined as

$$f_{r,d} = \frac{n_w \cdot c}{2 \cdot L} \tag{3}$$

with c as the speed of sound c=340m/s, the duct length L and the number of half-wavelengths in the duct n_w=1,2,3,...

The other two resonant mechanisms are correlated to the test section chamber. The Helmholtz-type resonance effect is dependent on the test section chamber volume and the length of the neck, namely the nozzle or collector/diffusor length. The eigenfrequency of the test section chamber $f_{r,ts}$ can be calculated like

$$f_{r,ts} = \frac{c \cdot r_n}{2\pi} \sqrt{\frac{\pi}{V \cdot \left(l_n + \pi \cdot \frac{r_n}{2}\right)}} \tag{4}$$

with V as the test section volume, the neck length l_n and the neck radius r_n. This approach neglects the end correction for the neck of the resonator. The second resonance effect of the test section chamber can be calculated as cavity resonance with

$$f_{r,ts\text{-}c} = \frac{c}{2\sqrt{\left(\frac{l_x}{n_x}\right)^2 + \left(\frac{l_y}{n_y}\right)^2 + \left(\frac{l_z}{n_z}\right)^2}} \tag{5}$$

and l being the dimensions of the test section chamber and n=1,2,3,...

It is worth mentioning that these equations are simplified and some neglections are present. The resonance frequency equations (3), (4) and (5) are only valid for a zero mean flow through the duct. The coupling of the test section chamber air volume and the open ends of the wind tunnel duct are neglected.

The last resonance mechanism, which is described in [15], is the edge-tone-type feedback mechanism. This resonance mechanism is caused by vortical structures of the shear layer hitting the collector. The periodic vortical structures of the shear layer can then create an edge-tone at the collector. The pressure wave of the edge-tone can travel upstream back to the nozzle, where the pressure fluctuations further excite the vortex shedding at the nozzle exit. When the edge-tone frequency coincides with the vortex shedding, a resonance is present.

If the vortex shedding at the nozzle is influenced by resonant effects, e.g. the edge-tone feedback or standing waves in the wind tunnel duct, the vortex shedding frequency is no longer proportional to the wind speed, like in equation (2). The vortex shedding frequency is, in this case, only slightly increasing with the wind speed and is locked into the resonance frequency, as mentioned in [15].

Wickern et al. [15] investigate the flow of a model-scale wind tunnel to verify the resonance equations and the resonant flow phenomena described before. The key findings are that two pressure fluctuations with distinctive peaks are found and can be related to two standing waves in the wind tunnel duct. A third frequency peak of the pressure spectrum is assumed to be linked to the Helmholtz-type resonance in the test section chamber. They further mentioned that the findings indicate that it is relevant to model the whole wind tunnel duct for resonance investigations. Modelling only parts of the wind tunnel could lead to false results when investigating the resonance effects, which lead to low-frequency wind tunnel buffeting. Furthermore, Wickern et al. [15] now introduce an active resonance control system (ARC) which suppresses the wind tunnel resonances by adding pressure fluctuations with a loudspeaker, which are in anti-phase to the pressure fluctuations of the wind tunnel resonances. They show that the ARC suppresses the resonance effects as well as vortex generators in the nozzle. An overall good agreement can be found by comparing the model-scale results with the full-scale wind tunnel. The distinctive resonance frequencies of the model-scale wind tunnel can be linked to the full-scale experiments with a frequency shift proportional to the wind tunnel dimensions.

Wickern et al. [15] continue with the evaluation of the influence of wind tunnel resonances on aerodynamic results. They found that for the wind speeds where the resonance effects are the strongest, high deviations for the measured integral forces of the vehicle can be observed. They further compare the force coefficients of a vehicle for different wind speeds with and without the ARC system. They showed that with the ARC system, which reduces the resonant pulsations of the wind tunnel, the force coefficients are more constant, and no

high deviations are present for different wind speeds. The explanation of [15] is that when the wind tunnel flow is in resonance, the vortex shedding at the nozzle exit is intensified, as mentioned before. This additional excitement at the nozzle also leads to an excitement of the shear layer. Wehrmann [16] shows that with the higher excitement of the shear layer, a higher level of mixing causes the shear layer to get wider and the entrainment of the shear layer to increase. The higher entrainment in the jet leads to a pressure build-up in front of the collector. This pressure build-up is measured by [15]. This additional pressure in front of the collector leads to lower measured drag coefficients. This effect amplifies the existing wind tunnel interference caused by the pressure distribution in the test section. That the pressure build-up is in front of the collector is also shown by the increased lift, mainly on the rear axle. Comparing the results with and without ARC, the front axle lift is not influenced as much as the rear axle lift. [15] also showed that with the ARC system, the resonance effects can be reduced, the additional pressure build-up in front of the collector is minimized and the influence on the drag values is decreased.

This shows that the resonance effects and the wind tunnel pulsations have a huge influence on the force coefficients measured in a wind tunnel. The ARC system manages to reduce the influence of the resonances, but low-frequency pulsations are still present in the wind tunnel flow. Their influence must be further investigated.

Rennie [17] investigated the aforementioned edge-tone feedback mechanism in more detail. He found that this mechanism is crucial for the resonance effects in the test section chamber. He shows that the vortical structures in the shear layer travel at around 65% of the speed in the core of the jet. How and when the vortical structures hit the collector is important for the presence of the feedback resonance effect. The time when the vortical structures hit the collector is defined by the wind speed and the test section length. He gives the following equation to calculate the frequency of the edge-tone:

$$f_e = \frac{1}{\left(\frac{1}{n}\right) \cdot \frac{L_{jet}}{0.65 \cdot u} + \frac{L_{jet}}{c\text{-}u}} \tag{6}$$

with L_{jet} being the length of the jet, u being the wind speed, c being the speed of sound and n=1,2,3,...

Rennie [17] suggests that the test section length is also an important length scale, which should be considered for investigations of low-frequency wind tunnel resonances. He also showed that when the vortex shedding at the nozzle is in resonance, the frequency is no longer proportional to the wind speed but is locked into the resonance frequency.

How important the edge-tone feedback resonance effect is can be seen in the investigations of Lacey [18] and Rennie et al. [19]. Lacey suggests a slanted collector design. With the slanted collector, the vortical structures of the shear layer are not hitting the collector at the same time and therefore the feedback of

the edge-tone does not hit the nozzle simultaneously. This stops the resonance at the nozzle exit and the feedback tone does not excite the vortex shedding over the whole nozzle and detunes the resonance frequency. The approach of Rennie et al. [19] is to add a breather gap between the collector and the diffusor. They found that this gap helps to reduce the resonance mechanism of the edge-tone feedback and achieved lower levels of low-frequency pulsations. Both state that reducing the low-frequency pulsations of the wind tunnel helps to get consistent results for various wind speeds.

Another investigation by Evert et al. [20] shows interesting findings regarding the resonance effects and low-frequency pulsations of automotive wind tunnels. They found that the resonance wind speed for specific wind tunnel eigenmodes is dependent on the type of vehicle positioned in the test section. They tested a racing car, a notchback and an estate back vehicle. For the different cars, the maximum peaks of the wind tunnel resonance frequencies are at different wind speeds. Also, they found a correlation between the frontal area of the vehicle and one specific wind tunnel resonance frequency. Dependent on the frontal area, the resonance frequency is slightly shifted. Corresponding to [17], Evert et al. [20] found a dependency on the resonance frequencies on the test section length as well. They altered the position of the collector and found a shift of the resonance frequency proportional to the test section length. Given the fact that the resonance frequencies of the wind tunnel are dependent not only on its geometry alone but also on the type and dimension of the tested vehicle and on the collector position, Evert et al. [20] suggested an optimised control system for the ARC of [15], which takes all these variables into account. Finally, they assumed that the standing wave within the wind tunnel duct is mainly responsible for the vortex shedding resonance and not the edge-tone feedback mechanism.

In the following years, a lot of research has been conducted on solutions to reduce the low-frequency pulsations for the resonant wind speeds. The research of Amandolese et al. [21] suggests that adding flaps at the nozzle exit helps to reduce low-frequency pulsations. Similar results are shown by Wang et al. [22]. They added a breather gap to the nozzle and varied the angle of the collector. Additionally, they added a Helmholtz-type resonator pipe on top of the test section of their model-scale wind tunnel. All these measures lowered the intensity of the wind tunnel buffeting. Bao et al. [23] showed the influence of vortex generators at the nozzle exit on the wind tunnel buffeting and the turbulent kinetic energy. Both can be reduced with specific vortex generators. Jin et al. [24] showed that a standing wave is present in the test section chamber. The wavelength of the standing wave is dependent on the width of the test section chamber. A resonance effect can be seen when the resonance frequency of the standing wave coincides with the frequency of the edge-tone feedback resonance. They managed to lower the buffeting level by not only adding vortex generators at the nozzle exit but also managed to alter the resonance frequency of the standing wave by altering the width of the test section chamber of the model-scale wind tunnel. Jia et al. [25] investigated the resonance characteristics of a

model-scale wind tunnel. By exciting the vortex shedding at the nozzle exit with pulsed jets with the resonance frequency of the wind tunnel duct, the resonance effect can be amplified. They showed that with an excitement of the vortex shedding with higher frequencies, the large vortical structures of the shear layer can be disturbed. This partially prevents the forming of the vortex rings, as shown in Figure 2, and the size of the vortical structures is reduced. Thereby the level of buffeting is also decreased. Lastly, Jin et al. [26] found that the standing waves in the wind tunnel duct are excited by the edge-tone feedback mechanism. This excitement can be altered by the inlet cross-section of the collector. With an increased inlet cross-section of the collector, they were able to reduce the low-frequency buffeting.

A more detailed investigation of the vortex shedding at the nozzle has been conducted in 2018 by Schoenleber et al. [27]. They investigated the vortex at the nozzle shedding and found some new insights into the shear layer and its vortical structures. In contrast to [15], they claim that the Strouhal number of the vortex shedding based on the hydraulic nozzle diameter D_h is at around St=0.48. In their measurements, they found a constant Strouhal number of St=0.46 for the vortex shedding. Furthermore, they describe waves arising from the nozzle edge, which further downstream evolve to large vortices at the outside of the shear layer. This observation leads to a new understanding of the development of the shear layer. In this study, the influence of the nozzle geometry has also been investigated. It is stated that the pressure distribution of the test section for the nozzle without vortex generators is dependent on the wind speed. For certain wind speeds, a pressure build-up in front of the collector can be seen. This can be explained by the resonance effect of the shear layer for the configurations without vortex generators, which leads to higher entrainment caused by the higher excitement of the shear layer in resonance. This effect is reduced for measurements with vortex generators in the nozzle. These findings correspond to the aforementioned work of [15].

Jia et al. [28] investigated in 2019 the shear layer of a 3/4 open-jet wind tunnel. They described a vortex shedding at the nozzle. The smaller vortical structures travel downstream and a pairing of the vortical structures to a large vortex can be seen at the distance of one hydraulic nozzle diameter. They also found that the pressure fluctuations in the test section chamber are related to pressure fluctuations of the vortical structures in the shear layer. This can be seen in the decomposition of the velocity field. There the low-frequency wind tunnel buffeting corresponds to the frequency of the vortical structures of the shear layer.

In 2021 Schoenleber et al. [29] showed time-resolved measurements of a passenger vehicle in a model-scale wind tunnel. They found that the low-frequency buffeting of the wind tunnel can be measured by the surface pressure probes of the vehicle. At the scale, the low-frequency buffeting could not be measured that clearly. They assume that this is caused by the eigenfrequencies of the scale itself. With the scale oscillating at her own eigenfrequencies, the wind

tunnel frequencies cannot be measured. In [29], it is also stated that the Strouhal number of the wind tunnel buffeting above a certain wind speed is not proportional to the increasing wind speed. This corresponds to the lock-on effect of the low-frequency wind tunnel to resonant frequencies shown in [15] and [17].

All these investigations demonstrate that wind tunnel buffeting is not only problematic for the structural integrity of the wind tunnel itself but has an influence on the aerodynamic measurement results. On the one hand, by affecting the pressure distribution in the test section because of resonance effects and amplified excited shear layers and, on the other hand, by the fluctuation of the incoming flow itself. The latter effect has been the subject of research on a similar topic. Many researchers investigated the influence of crosswinds or turbulent incoming flow on the vehicle's aerodynamic characteristics. In a way, this is comparable to the wind tunnel flow itself but exaggerated. In the crosswind investigations, the incoming flow is added with certain fluctuations. Even if one assumes an ideal constant inflow for the wind tunnel test, the low-frequency buffeting is always causing the incoming flow to fluctuate to a certain extent. In studies like [1], [30], [31], [32], [33], [34], [35] and [36], a strong influence of the crosswind and incoming flow characteristics on the aerodynamic measurements is shown. In [34], Yamashita et al. show a dependency of force coefficients on the fluctuating incoming flow. They get different deltas for the aerodynamic force coefficients between different diffusor angles of a vehicle depending on the fluctuations of the incoming flow. Even wind speed fluctuations, namely pulsations of the flow in its main flow direction (x-direction), have an influence on the aerodynamic results. Especially this effect is interesting because this kind of fluctuation is similar to the fluctuation of the wind tunnel flow caused by the low-frequency buffeting. Stoll et al. [35] show that not only the generated crosswind but also the dynamic behaviour of the wind tunnel jet is important for the analysis of unsteady aerodynamic characteristics. Fei et al. [36] investigate the influence of fluctuating incoming flow on the empty test section and the vehicle measurements. They found that an increasing amplitude of the incoming flow fluctuation leads to an increase in pressure in front of the collector. This is in accordance with the assumption of [15] that a more excited flow or shear layer leads to more entrainment and an increase of pressure in front of the collector. They also showed an influence of the angle and frequency of the incoming flow on the aerodynamic measurements. With these findings, the influence of wind tunnel buffeting and the fluctuations of the incoming flow on aerodynamic measurement results cannot be ruled out and must be investigated.

Also, Sebald et al. demonstrate in [37] and [38] the relevance of the low-frequency buffeting of the wind tunnel for the aerodynamic results. They compare numerical and experimental flow field data of a passenger vehicle. The key findings are that comparing experimental data of wind tunnel tests with numerical data shows some deviation, especially for time-resolved data. They state that is mainly caused by the presence of the low-frequency wind tunnel buffeting in wind tunnel tests and their absence in numerical simulations. In [37],

a frequency shift in the wake of the passenger vehicle between the numerical and experimental data can be seen. This frequency shift can be caused by the vortex shedding frequencies of the vehicle lock-on to the low-frequency wind tunnel buffeting frequencies. Also, a deviation between the turbulent kinetic energy in the wake is stated. In [38], they introduced a novel approach to include the low-frequency wind tunnel fluctuations in the numerical simulation. With the wind tunnel frequencies, the comparability of the numerical and experimental results is enhanced. Additionally, a great influence on gradients of the test section is shown. This shows that wind tunnel buffeting has an influence on aerodynamic results and needs to be investigated.

A lot of research has been conducted on unsteady flow phenomena in the wake of passenger vehicles. The focus of this research was mainly on the vortex shedding processes at the rear of the car. This research also tried to identify certain frequencies, respectively Strouhal numbers in the wake, which can be associated with specific structures in the wake of the vehicle. For example, Duell et al. [39] investigated the vortical structures behind a simplified bluff body and suggest two main Strouhal numbers for the vortices in the wake. Also, Sims-Williams et al. investigated in [40] the wake of a simplified notchback vehicle. They found that the frequencies of the vortex shedding and of the vortical structures in the wake are similar to those of a fastback vehicle. In [41], Barros et al. showed for a simplified bluff body that the vortical structures in the wake can be excited with pulsed jets. They found a dependency of the pulsing of the jets on the fluctuation intensity in the wake. When the pulsed jets are in resonance with the natural frequency of the vortical structures, the vortex shedding can be amplified. Gilhome et al. [42] conducted similar research but with a production notchback vehicle. They found two main frequencies for the vortical wake structures. These frequencies match the natural frequencies of other flow phenomena like leading edge separations and backward-facing steps. Kawakami et al. [43] optimised the driving performance of a production hatchback vehicle with vortex generators on the side of the rear. They observed that adding these vortex generators reduced the fluctuation intensity of the vortical structures of low Strouhal numbers and improved the driving performance of the vehicle. Lately, Bock [44] investigated the coherent vortical structures in the wake of a simplified bluff body and compared them to the structures of a production estate back vehicle. Sims-Williams et al. [45] observed that the Strouhal numbers of the vortical structures in the wake of their simplified vehicle model do not scale proportionally to the model scale. They tested two different model scales, namely 12.5% and 40%, in two different wind tunnels and found that the Strouhal numbers are not proportional to the model scale or a length scale of the vehicle, respectively. They suggested the theory that these frequency shifts are caused by the wind tunnel flow. Both wind tunnels have different characteristics regarding the low-frequency eigenmodes. This means that the low-frequency pulsations of the wind tunnels are at different frequencies. The vortical structures are excited by the low-frequency pulsations of the wind tunnel flow and a lock-on phenomenon is expected. Hence, the

frequencies and Strouhal numbers in the wake of the vehicle are dependent on the low-frequency pulsations of the wind tunnel. This effect can be underlined by the findings of Sebald et al. [37], where they found a discrepancy between wake frequencies of numerical and experimental data. In the numerical data, the low-frequency wind tunnel pulsations are not considered. Without the low-frequency wind tunnel pulsations in the numerical simulation, it is not possible to have the same lock-on phenomenon as in the wind tunnel test. This means that considering the wind tunnel pulsations in the numerical simulations, the lock-on phenomenon might be simulated and the discrepancies in the frequencies can be reduced.

Overall, this shows the relevance of the influence of wind tunnel eigenfrequencies on the vortical structures in the wake of a vehicle. It is worth mentioning that the list of investigations on unsteady phenomena in the wake of passenger vehicles does not claim to be complete but is intended to show exemplary in which areas research was carried out.

Concluding, the amount of effort and research invested in low-frequency buffeting and its suppression shows the relevance for wind tunnel testing. Since all research tries to reduce the low-frequency fluctuations, little knowledge is gathered about the influence of the remaining pulsations. Furthermore, previous research tries to link frequencies of vortical structures in the wake of the vehicle to characteristic length scales. These attempts were often unsuccessful and a hypothesis about the interference between wind tunnel buffeting and vehicle modes is given.

1.3 Outline and Objective

This dissertation elaborates on a novel boundary condition for the numerical simulation enabling investigations on time-resolved interference effects between wind tunnel eigenmodes and the vortical structures of a vehicle. Having computational cost in mind for an industrial application, it can be too time-consuming and complex to simulate the whole wind tunnel duct with a compressible solver. This is mostly due to the higher number of cells needed in the bigger CFD domain of the whole wind tunnel duct compared to a partial model. But in theory, this would be needed to analyse the aeroacoustic resonance effects of the wind tunnel. This work shows how the novel boundary condition is able to analyse the wind tunnel modes in an incompressible simulation with only a partial model of the wind tunnel.

In the previous chapter, the different wind tunnel resonance mechanisms and their influence on the flow are described together with potential influences on vehicle tests. After describing in chapters 2.1 and 2.2 the experimental and numerical methods, which are used in the presented work, these basic phenomena and the interference effects in the form of lock-on effects are reproduced in

chapter 2.3 for a generic cylinder test in different wind tunnels. For this test case, a numerical analysis is conducted in chapter 3.1 with a novel boundary condition for the CFD setup.

This new method produces promising results for the cylinder test case and therefore it is used to enhance the numerical wind tunnel flow. In chapter 3.2, crucial deviations of the time-resolved flow field between the current CFD setup and experimental wind tunnel results are shown. The new boundary condition is then used to optimise the numerical flow. In the optimisation process, different approaches for the boundary condition, which introduces the wind tunnel modes into the CFD domain, are analysed. Different filtering methods and scaling methods of the wind tunnel fluctuations are tested and some flow phenomena described in previous literature about wind tunnel effects can be reproduced with the numerical simulation. In addition to that, it can be seen which frequencies have the most influence on specific flow phenomena. These are not only new insights into this research topic, but it also supports the previous research hypothesis. After the optimisation process, the numerical wind tunnel flow has high accordance with the experimental wind tunnel flow.

The enhanced numerical wind tunnel flow is then used in chapter 4 to investigate the influence of the wind tunnel eigenmodes on the wake of a vehicle. With the new method, the difference between a vehicle in an ideal numerical box flow and the flow in the numerical wind tunnel with the exact flow phenomena found in the experimental wind tunnel can be analysed. With this result, the effect of the wind tunnel modes on vehicle tests can be determined. Also, it can be shown which frequencies are from the vortical structures of the vehicle and how they are influenced by the wind tunnel modes. The results of this chapter show that it is essential to include the wind tunnel modes in numerical simulations. Especially when a comparison to the experimental flow is conducted. Furthermore, this new method enables further research about vortical structures in the wake of the vehicle.

In the end, in chapter 5, a conclusion of the newly gained insights is presented and an outlook for possible further investigations is given.

2 Experimental and Numerical Methods

It is essential to better understand the unsteady inference effects of automotive wind tunnels. This helps not only to optimise the CFD simulations but also to get a deeper insight into the behaviour of wind tunnels. Experimental and numerical investigations are conducted to analyse the unsteady flow phenomena, which are present in the wind tunnel and around the passenger vehicle inside the test section. Especially the interference between the wind tunnel flow and the vehicle flow will be investigated.

In the following chapters, the experimental and numerical methods used in this dissertation are introduced. The wind tunnel facilities, reference models and the numerical setup of the investigation are described. Lastly, the numerical setup is optimised to correctly predict the unsteady flow phenomena.

2.1 Experimental Methods

Experimental results are the foundation for this research and are the starting point for the optimisation of the numerical setup. Different measurement techniques in different wind tunnels are used to build a basis for the validation of the numerical setup. The main goal of the CFD optimisation in this research is to predict the flow field around a passenger vehicle in the wind tunnel with high accuracy. Therefore, it is crucial to have a significant amount of information about the flow around a vehicle. Especially unsteady experimental results are important for the validation of the time-resolved flow field. The experimental methods that are used are described in the following chapter.

2.1.1 Wind Tunnel Facilities

The most important tool for aerodynamic research and development is the wind tunnel. In this work, three different wind tunnels with different specifications and flow characteristics are used. A model-scale wind tunnel and the Wind Tunnel A (WTA) at the Technical University (TU) Munich and a full-scale automotive wind tunnel at AUDI AG are used for this work. Especially the model wind tunnel of the TU Munich has significantly different wind tunnel eigenmodes due to its size compared to the other wind tunnels. This enables an investigation of the influence of different resonance frequencies and eigenmodes of a wind tunnel on the flow field around an object.

Model Wind Tunnel of TU Munich

The model-scale wind tunnel is depicted in Figure 3. It has a relatively small nozzle outlet cross-section of A_N=0.056m² and a test section length of around l_T=0.5m. Wind speeds from up to 25m/s can be measured. In comparison to the

other wind tunnels, which are 3/4 open jet wind tunnels, this wind tunnel can be described as a full open jet wind tunnel. However, it has a mounting plate in the test section, which is mainly outside of the flow. This plate restricts the flow's expansion, so the wind tunnel flow is partially comparable to a 3/4 open jet wind tunnel. The objects to be measured and measurement equipment can be positioned on the mounting plate. The model wind tunnel has a turbulence intensity of Tu<0.2% and will be used for a generic test case.

Figure 3: Model-scale wind tunnel at TU Munich

Wind Tunnel A of TU Munich

The wind tunnel A (WTA) of the TU Munich is larger than the model-scale wind tunnel. It has a nozzle outlet cross-section of A_N=4.32m² and a test section length of l_T=4.8m. It has a 3/4 open test section and can reach wind speeds of up to 65m/s. At the nozzle exit, it has a turbulence intensity of Tu<0.2%. In this work, this wind tunnel will only be used for a generic test case and for comparison to the model-scale wind tunnel. More details about the wind tunnel are described by Mack [46]. In Figure 4, the nozzle of the wind tunnel is depicted.

Figure 4: The nozzle and parts of the test section from the WTA of the TU Munich

Audi Aeroacoustics Wind Tunnel

The Audi Aeroacoustics Wind Tunnel (AAWT) is a full-scale automotive wind tunnel [47]. It is a 3/4 open jet wind tunnel with a nozzle outlet cross-section of A_N=11m^2. It has a variable test section length of l_T=9.0-10.0m. The variability is achieved by a movable collector. In this work, the collector is fixed to a position with a test section length of l_T=9.5m. Wind speeds of up to 83.33m/s are possible with a turbulence intensity of Tu<0.3%. It has an external scale, which has an accuracy of 2.25N and is positioned in a turntable with a diameter of 6.7m. The AAWT has a boundary layer suction and a five-belt rolling road system for optimal ground simulation. In this work, both features are not used. All measurements are conducted with a static ground and without boundary layer suction. This helps reduce the complexity between the CFD setup and the measurement conditions in the AAWT. The CFD setup will be discussed later in more detail. All the mentioned information and more details about the performance of the AAWT are described in [47] by Wickern and Lindener.

In Figure 5, a vehicle in the AAWT test section can be seen together with the traversing arm, which is used for hot-wire measurements in the wake of the vehicle. Sebald et al. [37] show that with this traversing arm and a hot-wire probe, it is possible to measure transient flow structures. They could not see the mechanical oscillations of the traversing arm in the hot-wire measurement signal. Therefore, the measured oscillations or fluctuations are caused by the flow field and not by the traversing arm itself. Hence, this measurement method will be used to gain information on the transient flow field behind a vehicle in the AAWT.

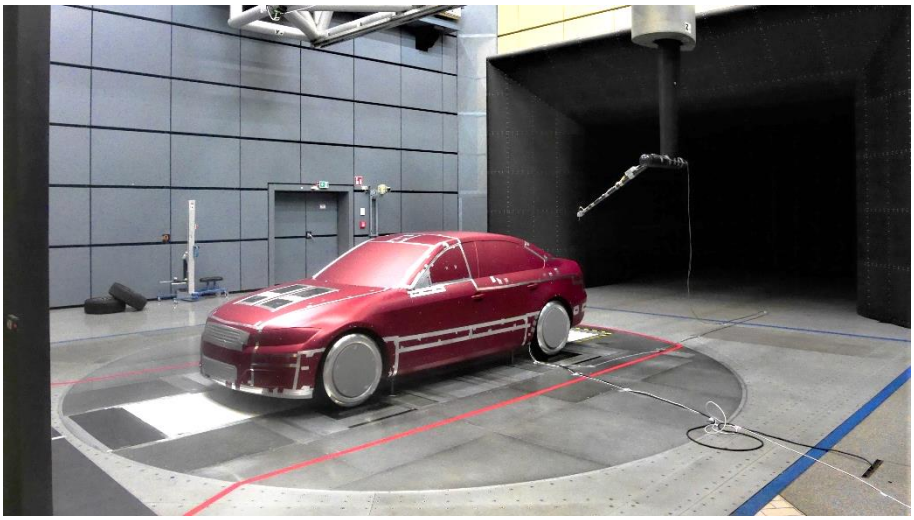

Figure 5: Vehicle in the Audi Aeroacoustic Wind Tunnel.

For the later investigations, it is necessary to know the layout of the AAWT. This is depicted in Figure 6 based on the AAWT plan given by Wickern and Lindener in [47].

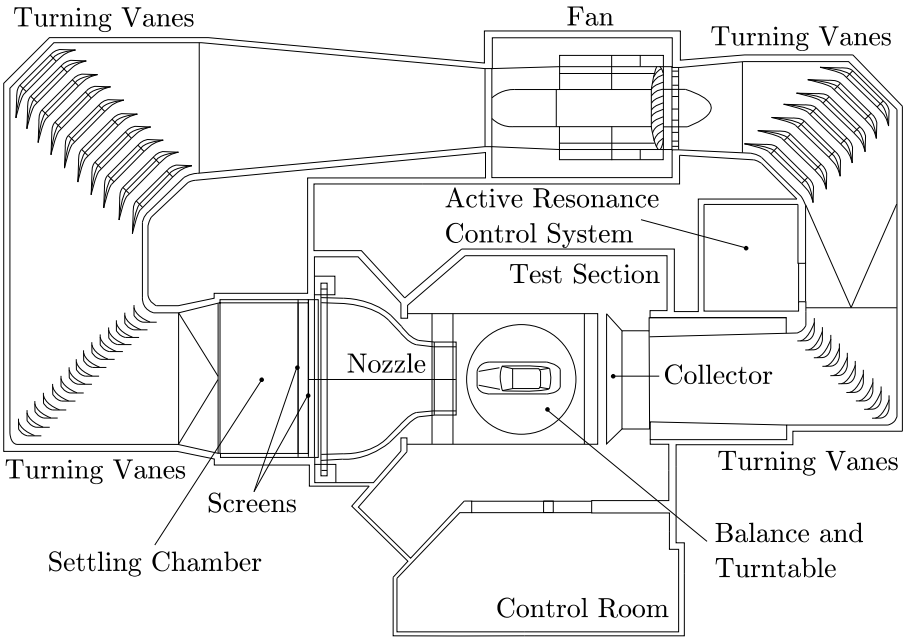

Figure 6: AAWT layout based on Wickern and Lindener [2]

In this layout, the whole wind tunnel duct is shown, including the fan, turning vanes, settling chamber, nozzle, test section and collector. One special part of the AAWT is the active resonance control system (ARC). This system helps to

reduce wind tunnel pulsations. Wickern et al. describe the wind tunnel pulsations and the active resonance control system in [15]. They show three low-frequency eigenfrequencies in the AAWT. These resonance frequencies are mostly attributed to standing waves in the duct of the wind tunnel, depending on the wind speed. The resonances are excited by vortex shedding processes at the nozzle exit. Wickern et al. also mention that these frequencies are changing with altering wind speeds. For a wind speed of 38.89m/s, which is the wind speed for most of the conducted measurements, the pulsations of the AAWT are at around 2.5Hz, 4.2Hz and 6.7Hz. These frequencies of the AAWT eigenmodes will be discussed later in more detail. With the ARC, a large part of the low-frequency pulsations can be damped without adding additional noise to the flow. This is necessary because of the influence of wind tunnel pulsations on aerodynamic and aeroacoustics measurements, which is shown in [15].

For a quick comparison of the used wind tunnel facilities, the key specifications are given in Table 1.

Table 1: Wind tunnel specifications overview

		Model wind tunnel	**WTA**	**AAWT**
Nozzle cross-section	A_N	0.056m²	4.32m²	11m²
Test section length	l_T	0.5m	4.8m	9.0-10.0m
Turbulence intensity	Tu	<0.2%	<0.2%	<0.3%
Max. wind speed	$\max(\vec{u})$	25m/s	65m/s	83.33m/s

2.1.2 DrivAer Reference Vehicle

For the conducted investigations in the wind tunnel, a passenger vehicle is needed. This research is based on the DrivAer reference model, which was introduced in 2012 by Heft et al. [48]. The DrivAer is a generic car model, but in contrast to other generic models like the Ahmed-Body [49], this is a very realistic vehicle model. This helps to conduct more realistic and more meaningful investigations of the flow around a passenger vehicle and therefore contributes to closing the gap between generic and production vehicle models [48]. Apart from the generic geometry, the model has the advantage that numerous shapes and configurations can be investigated. It is possible to alter the rear end of the vehicle to get a fastback, notchback and estate back rear end. Additionally, two different underbodies are available. One of them is a realistic underbody from an internal combustion vehicle with a gearbox and an exhaust and the other one is

a generic flat surfaced underbody. It is also possible to conduct measurements with and without side-view mirrors. All these variations can be found in [48]. The first manufactured DrivAer model was a 1:2.5 scale model at the TU Munich. Over the years, numerous extensions were added to the model, especially in the engine compartment, as shown in Mack et al. [50] and Wittmeier et al. [51], to make the characteristics of the model even more realistic. In 2017 Hupertz et al. [52] introduced the full-scale model of the DrivAer. In this dissertation, another full-scale DrivAer model will be used. It is owned by Volkswagen AG and corresponds to the geometry presented in [52].

In this research, the DrivAer geometry with the notchback rear end and the generic flat underbody will be used. This configuration of the DrivAer has a frontal area of A_F=2.2m^2 and a wheelbase of l_{wheel}=2.786m. Additionally, the side mirrors are removed and the grille in the front and the engine bay outlets in the wheel arches are completely closed. A 0.01m lip in the front at the underbody for the whole width is added to the vehicle to ensure a defined flow separation on this edge. Deviations between the numerical and experimental geometry are reduced due to the strongly simplified vehicle configuration. Detailed information about the numerical setup and vehicle configuration and potential deviations are discussed later.

One main variation in the vehicle configuration is the option to have it set up with or without wheels. To further simplify the vehicle geometry, a setup without wheels and with closed wheel arches is investigated. This setup of the DrivAer without wheels in the AAWT is depicted in Figure 7 and the vehicle with wheels is depicted in Figure 8.

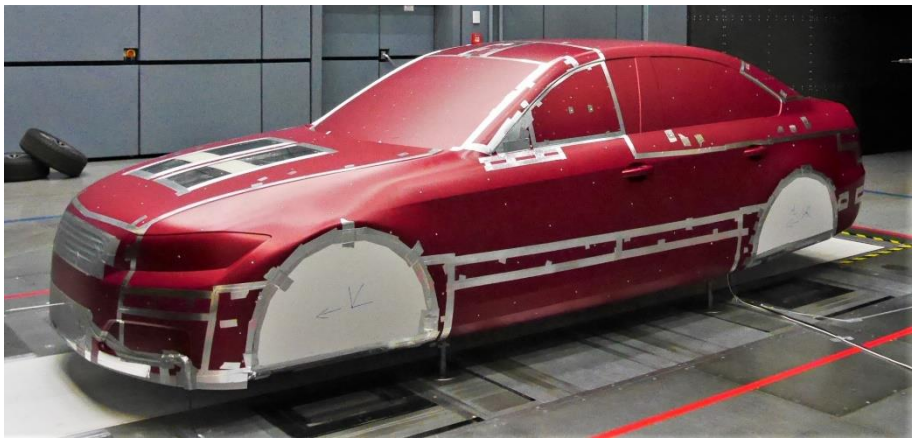

Figure 7: DrivAer without wheels and with closed wheel arches in the AAWT.

Figure 8: DrivAer with aluminium wheels and closed rims in the AAWT.

The configuration of Figure 8 with wheels uses no ordinary rubber wheels but wheels almost entirely made out of aluminium. Not only the rim itself but also the tire is aluminium made. Only a small layer of rubber with generic longitudinal grooves is added to increase the friction between the wheels and the belts of the rolling road system. This helps to reduce inference effects from the rubber tire, which are caused, for example, by the deformation of the tire. Reiss et al. [53] show that it is critical to include the deformation under rotation of the tire in the numerical simulations to get results which are comparable to the wind tunnel experiments. With the aluminium wheels, it is possible to avoid a potential geometrical deviation between the numerical and experimental deformation. Additionally, all measurements are conducted without ground simulation, therefore the wheels are not rotating. To further reduce interference effects of the tires, a flat cover is mounted on the rim so the flow through the rim is blocked.

2.1.3 Measurement Equipment

Not only because of its numerous geometric variants but also because of its measurement equipment, the aforementioned DrivAer model is ideal for scientific investigations. Many pressure probes are distributed over the whole vehicle. With these surface probes, the pressure distribution over the vehicle can be measured. The location of the pressure holes corresponds to the DrivAer models of [48] and [52] and is partially depicted in Figure 9. The information on the pressure distribution is very helpful for the comparison of numerical and experimental data. It gives a deep insight into the quality of the numerical setup and whether the flow over the vehicle is predicted correctly.

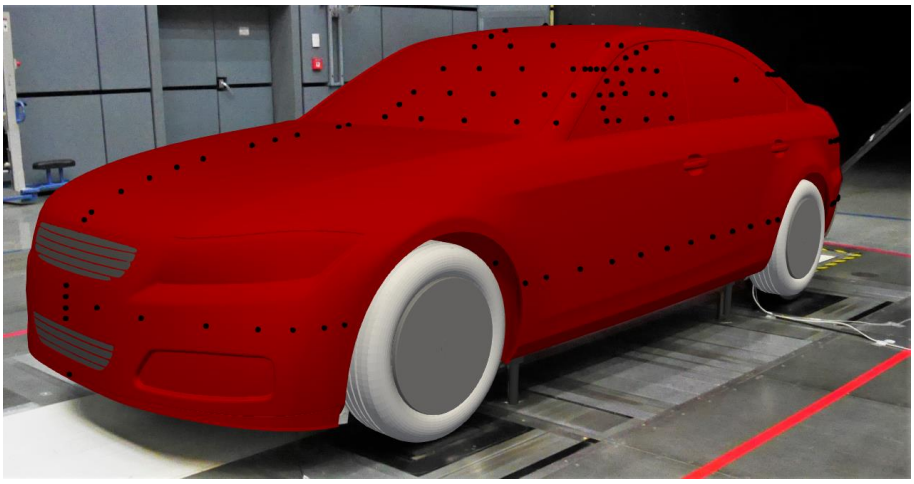

Figure 9: Surface pressure probes (black dots) visualized on the used DrivAer configuration

The pressure holes are connected to six *ESP-32-DTC* pressure scanners from *A-TECH Instruments LTD.* [54]. The pressure scanners contain piezoresistive silicon pressure sensors, which measure the differential pressure related to a reference pressure. The accuracy of the pressure measurement is at +/-0.1% for the full pressure range of +/-6,895Pa. Additionally, the sensors have a digital temperature compensation to further increase the accuracy of the sensor output regarding the calibration. For more detailed information, the reader is referred to the manufacturer's datasheet [54]. The six pressure scanners are connected to a *DTC Initium System* [55]. The system has an accuracy of +/-0.05% and converts the measurement signals of the pressure scanners to a digital signal, which is transmitted via ethernet to the measurement computer [55]. At the computer, the pressure measurement is conducted for one minute with a sampling rate of 40,000Hz. Then a temporal mean value is computed for each pressure channel. Although the sampling rate at the measurement computer is very high, it cannot be expected to measure time-resolved data at the pressure scanner due to the long hoses between the scanner and the surface probes.

Another pressure measurement system which is used in this work is a *Baratron*-based system from *MKS Instruments*. This system is used to measure the pressure of a Prandtl probe in the empty test section of the AAWT. The Prandtl probe is depicted in Figure 10. It consists of a differential pressure transducer and a high-accuracy signal conditioner. The signal conditioner is the *Type 670 Signal Conditioner* from *MKS Systems* [56]. This display unit reads the pressure information from the *698A12TRA Baratron* differential pressure transducer [57]. This pressure transducer has a pressure range from +/-6,666Pa with an accuracy of +/-0.05% for the entire pressure range and is temperature controlled. For further details of the *Baratron* system, the reader is referred to [56] and [57].

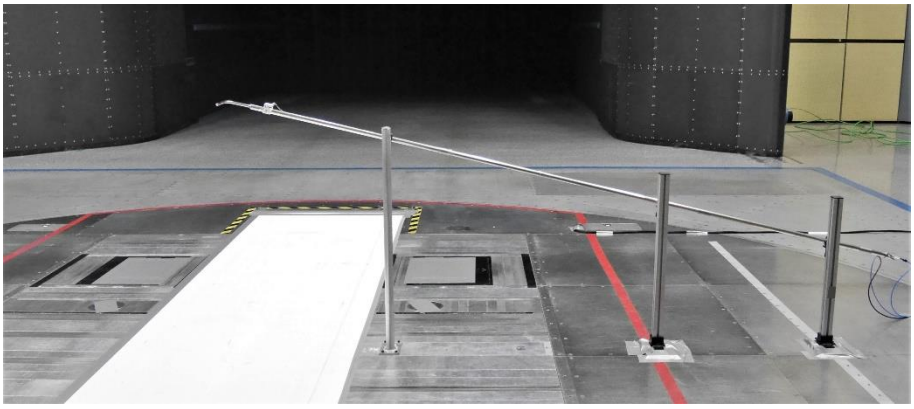

Figure 10. Prandtl probe in the empty test section of the AAWT

The third pressure measurement tool is the *SET 9324* module [58]. It has six measurement channels and one reference pressure channel for differential pressure measurement. It has a pressure range from +/-5000Pa and an accuracy of +/-0.5% [58]. It is used to measure the pressure on the back of the cylinder in the generic cylinder experiments later in this work.

In addition to the pressure measurements, integral force measurements of the DrivAer model are also carried out. These are conducted in the AAWT with its external scale. As mentioned before, the scale has an accuracy of 2.25N and a repeatability of 0.45N [47]. With the frontal area of the DrivAer and an exemplary wind speed of 38.89m/s, an accuracy of Δc_x=+/-0.001 for the force coefficients of the vehicle can be assumed.

The last measurement tool for this research is a single-wire hot-wire anemometer. It is a constant temperature hot-wire anemometer system from *DANTEC DYNAMICS*. The hot-wire temperature is controlled by the *MiniCTA 54T42* [59]. A single-wire hot-wire probe is connected to the *MiniCTA* and is used to measure the speed and fluctuation of the flow. The sampling rate for all measurements is set to 4,096Hz. Regarding the Nyquist criterion, this sampling rate is enough to measure the aerodynamic relevant fluctuations, which are expected to have frequencies lower 2,048Hz. Since the output of the *MiniCTA* is

only an analogue current, a calibration of the probe is needed for the measurements. The hot-wire is calibrated in the empty test section of the AAWT before each measurement session. One exemplary calibration curve and the process of calculating the wind speed out of the output voltage of the *MiniCTA* can be found in Appendix A. All measurements are temperature corrected because small temperature fluctuations of the wind tunnels for long measurements cannot be prevented. This helps to get high accuracy and repeatability of the measurements.

The single-wire hot-wire probe has only a restricted spatial resolution and different directions of the flow cannot be separated. Additionally, depending on the position of the hot-wire probe, the different directions are weighted differently. Becker [60] gives information about the weighting of the spatial directions. For the mounting position of the hot-wire in this work, the factors of Table 2 can be derived from [60]. These spatial weighting factors must be considered, especially when comparing measurement results. For this study, the x-direction is the direction of the main flow, the y-direction is the horizontal direction of the main flow and the z-direction is vertical. This means that the wire is oriented in z-direction.

Table 2: Spatial weighting of the hot-wire probe based on [60] for the used hot-wire position

Spatial direction	**x-direction**	**y-direction**	**z-direction**
Weighting factor	1.0	1.2	0.2

The stand for the hot-wire and a closeup of the single-wire hot-wire probe with the probe support are depicted in Figure 11.

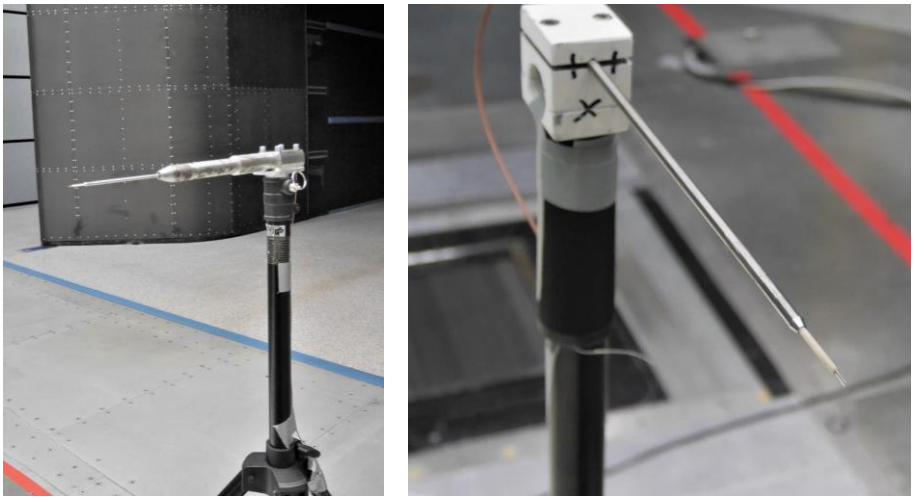

Figure 11: Single-wire hot-wire probe and the stand of the measurements in the AAWT (left), closeup of the single-wire hot-wire probe and the probe support (right).

2.2 Numerical Methods

Numerical simulations give the advantage of having information about the entire flow field without the need for complex measurement methods. That allows for efficient and detailed investigations of the flow field. A key factor in getting meaningful results out of numerical investigations is that the predicted flow field corresponds to the physics of the experimental flow field. A numerical setup, which is able to predict the complex and unsteady flow phenomena around a passenger vehicle, is therefore needed. Time-resolved simulation methods must be chosen but are often very computationally expensive. Methods like the *Direct Numerical Simulation* (DNS) or the *Large Eddy Simulation* (LES) can compute the time-resolved flow field without the need for any additional simplification or modelling but are not suitable for this research because of the high demands on computing capacity. An appropriate trade-off between the computational efficiency and the accuracy of results is the *Delayed Detached-Eddy Simulation* (DDES). This hybrid method uses LES in separated regions away from the wall in combination with *Reynolds-averaged Navier-Stokes equations* (RANS) in regions with wall proximity. More details about the used simulation method, software and parameters are given in the following chapter.

2.2.1 Delayed Detached-Eddy Simulation

One method to compute the flow field is using simplified Navier-Stokes-Equations. This is done with the RANS simulation method. The RANS method delivers a steady-state solution of the flow field while the time-resolved and unsteady turbulence of the flow field is modelled. To investigate time-resolved flow field data, the RANS method on its own is therefore not suitable. The LES method is able to compute the time-resolved flow and turbulence down to the length scale of the grid but is very costly regarding computational capacities. For vortical structures with a length scale smaller than the grid scale, the LES uses a sub-grid scale turbulence model.

The *Detached-Eddy Simulation* (DES) method uses RANS and LES to get time-resolved flow field data with high accuracy and less computational effort compared to the LES. This method was introduced by Spalart et al. [61]. The DES uses the RANS and LES modelling for different regions of the simulation. In regions near a wall, like the surface of the vehicle, the RANS method is used to compute the flow, especially within boundary layers. For regions distant from walls, the LES method is used. An additional advantage of the DES method is that wall models can be used in the RANS regions. These wall models are able to predict the boundary layer flow with high accuracy for a coarser mesh. This helps to reduce the cell count and further reduces the computational effort.

As a criterion for the switch between the RANS and LES methods, Spalart et al. [61] use only the wall distance. Therefore, the switch between the methods

does not depend on the flow characteristics but just on the grid. With this criterion alone, it can occur that for thick boundary layers, the LES method is used to compute the boundary layer. Due to the usage of wall models, the grid near a wall is too coarse for the LES method to correctly predict the boundary layer. Furthermore, the modelled turbulent viscosity in this region is too low and cannot be evened out by Reynolds stresses due to the coarse mesh. The incorrect modelling of the turbulent viscosity could lead to a separation of the flow. This effect is described by Menter et al. [62] as grid-induced separation. To solve the problem of grid-induced separation, Spalart et al. [63] introduced the DDES, which takes not only the grid scale but also the local flow characteristics into account. Flow characteristics, which are considered, are the local eddy viscosity and velocity gradients. These flow characteristics, in addition to the wall distance and grid-scale criterion, ensure that the LES method is not active in thick boundary layers.

The DDES simulations in this work are conducted with a Spalart-Allmaras turbulence model for the computing of the turbulent viscosity in the RANS region, as recommended by [64]. For the modelling of the sub-grid scale turbulent viscosity of the LES region, a Smagorinsky-like turbulence model is used [61]. Near the wall, the Spalding wall function, as described by Shih et al. [65], is used as all-y^+-treatment. With the mentioned turbulence models and DDES method, simulations of complex geometries in high Reynolds number flows, like a vehicle in the wind tunnel, can be performed with a good prediction quality. Furthermore, Spalart [66] states that the combination of RANS and LES is state-of-the-art for the kind of simulations conducted in this work.

2.2.2 Simulation Setup

In this work, the open-source software *OpenFOAM*® is used to conduct the DDES simulations. The used version is the v2012 distributed by *ESI-OpenCFD* [67]. Islam et al. [68] showed that DES simulations with *OpenFOAM*® are able to predict the flow field for automotive aerodynamics in good agreement with experimental results. The simulation method in this work is based on [68] with the extension of the DES to the DDES. The aforementioned benefits of the DDES are therefore utilized for the investigations of the flow field. The DDES method is well suited for CFD simulations of the vehicle flow in a wind tunnel, as stated by Collin [12].

The basis for the DDES is a spatially discretized numerical grid inside of a simulation domain. In this work, the finite volume method is used to get a finite count of volumes. This method has numerous advantages, which explain its use in automotive aerodynamics. For each volume, the equation of the underlying system is solved and the sum of mass flow going into one volume is equal to the outgoing mass. This helps to ensure a global mass conservation for the simulation. Furthermore, discretizing the simulation in finite volumes allows a good fitting

of the generated mesh of volumes on complex geometries like a passenger vehicle. The discretizing in this work is done with the volume meshing application *snappyHexMesh* by *OpenFOAM*® [67]. In general, a hexa-dominant volume mesh is generated with prism layers parallel to surfaces. The size of the prism layers on surfaces is selected so that good results can be achieved with the used Spalding wall function. Thus, the non-dimensional wall distance is in the range of $30 \leq y^{+} \leq 300$.

The simulation process is split into different parts. At first, the potential flow solution is computed with *applyBoundaryLayer* and *potentialFoam* [67] to initialize the flow field of the domain. Based on this flow field, the incompressible DDES simulation is started using the PISO algorithm (*Pressure-Implicit with Splitting of Operators*) [67]. At the start of the DDES simulation, a time step of $\Delta t = 10^{-3}$s is used to allow the flow inside the domain to develop for a physical time of 1s in a short period of time regarding the computational capacities. After the first second of computation, the time step is reduced to $\Delta t = 10^{-4}$s to increase the accuracy and temporal resolution of the computed flow. This last part of the simulation is computing 8s of physical time, but only the last six seconds are used for the analysis of the flow field. This structure of the simulation gives good results with an acceptable demand on computational capacities. This is shown in the following, e.g. with Figure 12.

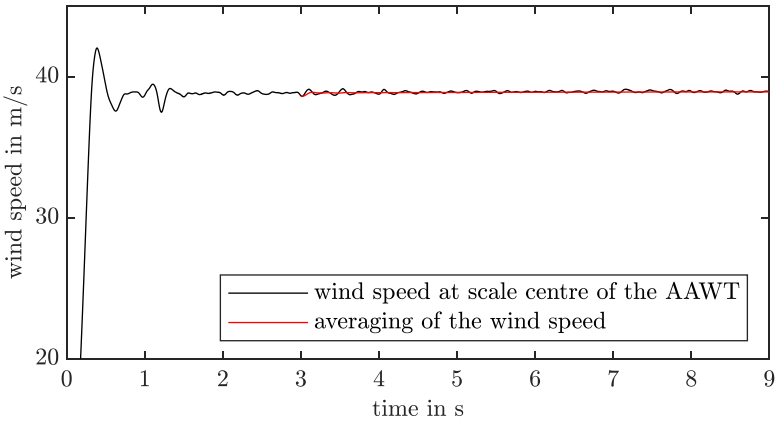

Figure 12: Wind speed fluctuations at the centre of the scale of the AAWT for the simulation time of 0:9 seconds. Averaging of the wind speed of 3:9s in red.

In Figure 12, the wind speed at the centre of the wind tunnel scale in z=1.0m is plotted. There one can see at the beginning, between 0 and 1s, the development of the wind speed. The wind speed in the test section is gradually increasing to the set wind speed of 38.89m/s. At t=1s, the time step is switched from $\Delta t = 10^{-3}$s to $\Delta t = 10^{-4}$s. Shortly after the time step switch, the wind speed overshoots the target wind speed, followed by a drop in velocity. This is the reason why the

averaging of the flow field parameters and the analysis of the flow field start at t=3s. Until 3s, the overshoot caused by the time step switch is levelled out and should not influence the results of the numerical simulation analysis. In red, the development of the time-averaging for the wind speed is given for the analysed period of time.

To further demonstrate that an analysis of the numerical flow field from t=3s to t=9s is valid, the temporal development of the pressure distribution in the test section is given in Figure 13.

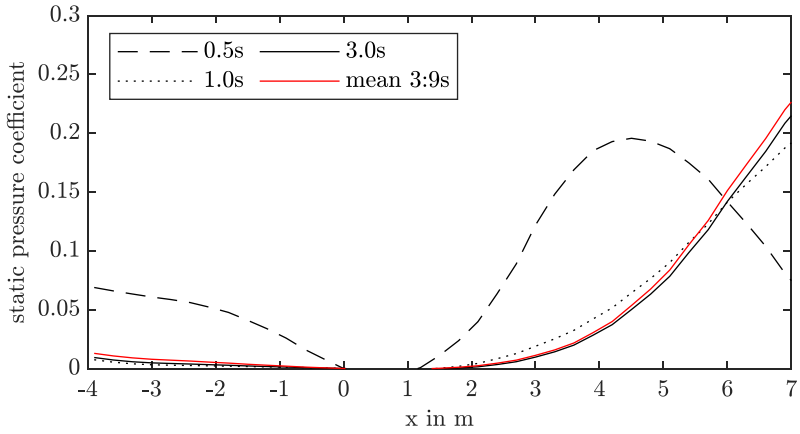

Figure 13: Temporal development of the pressure gradient at different simulation time steps in the test section of the AAWT. From the nozzle in the collector in the middle at y=0m and at a height of z=1.0m.

The temporal development of the static pressure distribution in the test section of the AAWT, depicted in Figure 13, shows how the flow field is evolving. Because the pressure distribution is dependent on the formation of the shear layer and the velocity distribution in the test section, a quasi-stationary state of the pressure distribution indicates that all these flow phenomena are fully developed and can be analysed. In Figure 13, the pressure distribution for specific time steps is given. At the initial time steps, which are plotted with dotted lines, a higher deviation from the quasi-stationary time-averaged pressure distribution coloured in red can be seen. This means that at this stage of the simulation, the flow field in the test section is not yet fully developed. Looking at the gradient with a solid black line, the pressure distribution of t=3s correlates well with the final time-averaged solution, coloured in red. This indicates that from t=3s on, the flow field in the wind tunnel is fully developed and can be analysed. With this strategy of flow field development and analyses, a sufficient span of physical time can be investigated with a moderate demand on computational capacities.

In this work, mainly three different numerical setups are used. Namely, a partial model of the AAWT with an empty test section. The partial model of the AAWT with the DrivAer in the test section. And lastly, a big generic box as a

domain to simulate the ideal flow over the DrivAer model without any wind tunnel interferences. A partial model in this context means that not the whole wind tunnel duct is simulated, but only the part from the settling chamber to the diffusor of the wind tunnel. The different domains and setups will be described in more detail later in this work. The most important information about the used CFD setups and settings of the computation with *OpenFOAM*® are given in Table 3.

Table 3: CFD setup specifications and information for the DrivAer model with wheels.

		AAWT with empty test section	**AAWT with DrivAer**	**Box with DrivAer**
Volume Cell count		$52 \cdot 10^6$	$97 \cdot 10^6$	$54 \cdot 10^6$
Core number			960	
Density	ρ		$1.1584 \frac{kg}{m^3}$	
Kinematic Viscosity	ν		$1.5711 \cdot 10^{-5} \frac{m^2}{s}$	
Turbulence Length	L_{turb}		0.01m	
Turbulence Intensity	Tu		0.5%	
Time step (start)			$0s \leq t \leq 1s$; $\Delta t = 10^{-3}s$	
Time step (final)			$1s \leq t \leq 9s$; $\Delta t = 10^{-4}s$	
Averaging interval			t=3-9s	

The following boundary conditions are used in the CFD setups. At the inlet, a velocity is set with a zero-gradient condition for the pressure. At the outlet, an inletOutlet condition is set and adjusted to the inlet velocity. For the pressure at the outlet, a fixed-value condition of zero is set. For the Box CFD setup, the walls and the roof of the box have a symmetry type boundary condition, which prevents the forming of a boundary layer. The symmetry boundary condition is also applied for the parts of the floor distant from the vehicle. In the AAWT CFD setups, the part between the real AAWT geometry and the inlet and outlet patch are treated as symmetry boundaries. The inlet and outlet patch of the AAWT CFD setups are moved away from the real geometry to prevent any

disturbances of the inlet and outlet boundaries with the wind tunnel flow. All other boundaries of the domain are treated as friction walls. The walls have a zero-gradient condition for the pressure, a fixed-value condition of zero for the velocity and a fixed-value of zero for the $\tilde{\nu}$ of the Spalding wall function. With these boundary conditions, a stable simulation with the conservation of mass inside the domain is possible. No further boundary conditions are necessary as all measurements are conducted without rotating wheels and without ground simulation. Therefore, the ground and the wheels of the vehicle in the CFD are also treated as stationary friction walls.

In Table 4, the used discretization schemes for the different physical terms are given based on the *OpenFOAM*® software [67]. For the pressure p, the velocity u, the turbulent viscosity $\tilde{\nu}$ of the Spalart-Allmaras turbulence model and the mass flow through the faces of the cell Φ the following solver schemes are used.

Table 4: Discretization schemes of the CFD in *OpenFOAM*® [67]

Type of Scheme	*OpenFOAM*® Keyword
Time scheme	backward
Gradient schemes	
p	Gauss linear
u, $\tilde{\nu}$	cellLimited Gauss linear
Divergence schemes	
Φu (start)	Gauss Gamma
Φu (final)	Gauss GammaV
$\Phi\tilde{\nu}$	Gauss Gamma

2.3 Generic Test Case and CFD Validation

To validate the simulation setup and to show basic unsteady flow phenomena, a generic test case of a cylinder will be used. A comparison between two different wind tunnels based on two cylinder geometries is made to identify differences in the time-resolved flow field. This comparison will be made with the help of CFD as well. To evaluate how well the time-resolved flow field phenomena can be predicted by the used CFD setup.

First, flow field data is measured in the WTA of the TU Munich. Given the diameter of the two cylinders of D=0.06m, respectively D=0.09m and a height of H_C=0.4m, the experiment is conducted with a very low nozzle blockage. With the nozzle outlet cross-section of A_N=4.32m², the nozzle blockage ratio is 0.55% for the 0.06m cylinder and 0.83% for the 0.09m cylinder. In Figure 14, the general mounting of the cylinder and the measurement equipment is shown. The cylinder is mounted at the nozzle exit. Due to the fact that the cylinder is mounted on top of the scoop, which removes the boundary layer, the boundary layer has a negligible influence on the results.

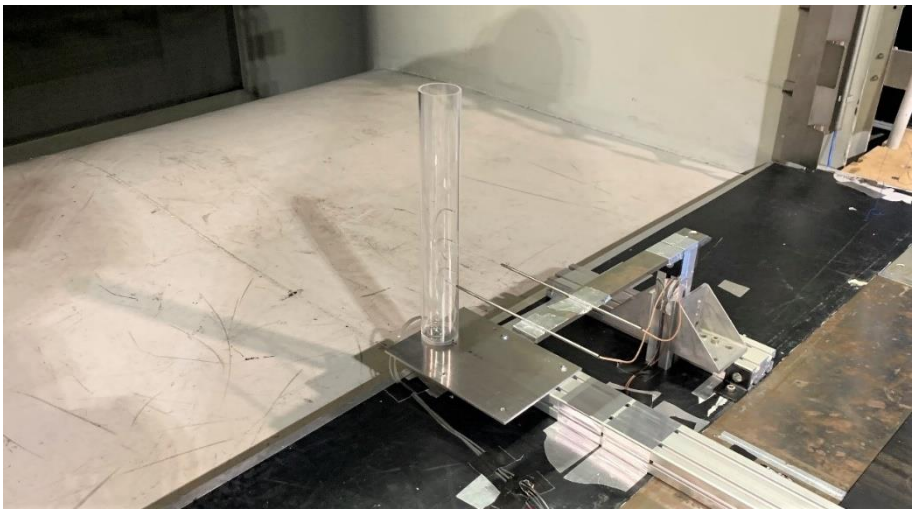

Figure 14: Cylinder in the WTA of TU Munich.

Two hot-wire probes are positioned 1.5D downstream of the centre of the cylinder. One hot-wire probe is positioned in the centre plane behind the cylinder. The other hot-wire probe is positioned 0.1m left next to the centre probe. The positioning of the hot-wire probes is shown in Figure 15. For this experiment, two single-wire hot-wire probes are used. Both are connected to the *MiniCTA*. The hot-wire probes measure the time-resolved flow field at the height of H_C=0.2m with a sampling rate of 4,096Hz. With the height of H_C=0.2m, the hot-wire probes are 0.2m distant from the top of the cylinder and the floor. This distance helps to further reduce the influence of the boundary layer and three-dimensional flow phenomena on top of the cylinder. Additionally, three pressure probes are at the backside of the cylinder to measure the base pressure of the cylinder. The pressure probes are connected to the *SET 9324* module. This module is also used to measure the pressure of a Prandtl probe to calculate the wind speed at the nozzle exit. In each wind tunnel, the measurements are conducted with wind speeds between around 5m/s and 23m/s. With the diameters of the cylinders, this results in a Reynolds number of $1.9 \cdot 10^4 < Re < 1.3 \cdot 10^5$. The measurement duration is set to 20 seconds.

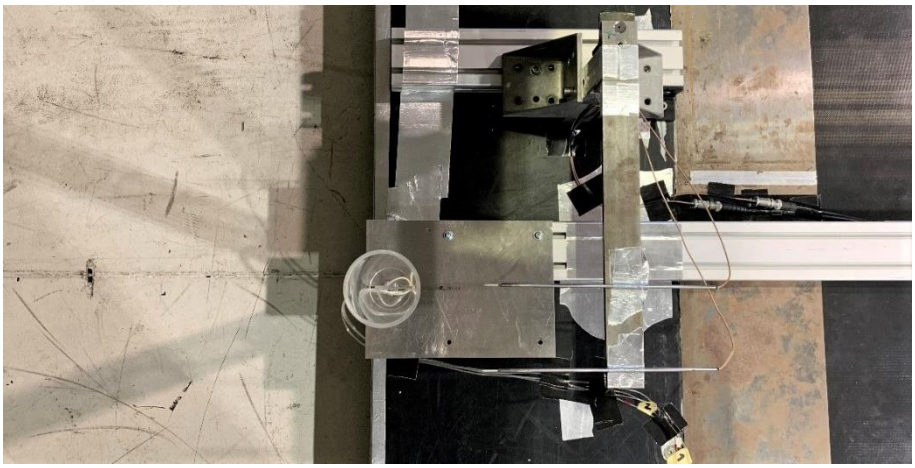

Figure 15: Top view of cylinder in the WT A of TU Munich.

The WTA is used as a reference measurement for the cylinder investigation with the assumption that the flow of the cylinder is not influenced by any interference effects. Especially not influenced by lock-on phenomena coming from wind tunnel eigenmodes near the cylinder frequencies. It is important to analyse the eigenmodes of the WTA to ensure that they are not near the cylinder frequencies. In Figure 16, the eigenmodes of the WTA are depicted.

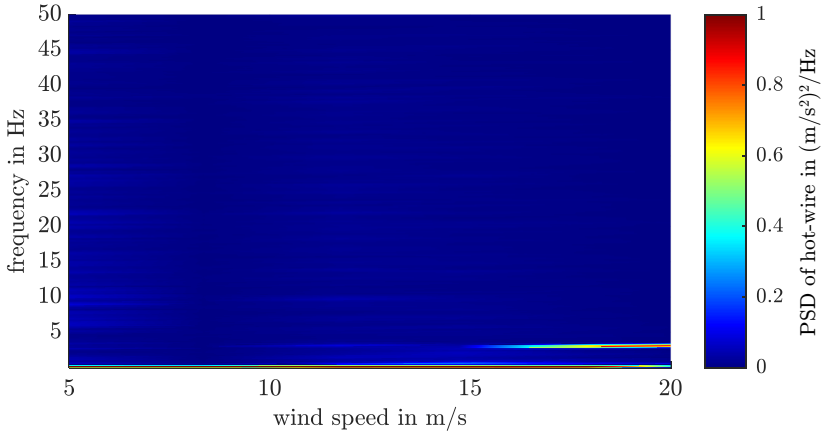

Figure 16: Spectrogram of the empty WTA test section of TU Munich for the outside hot-wire probe.

For a wind speed of 20m/s, the wind tunnel pulsation has a frequency of around 3.5Hz. This is far from the cylinder frequencies and no influence or a lock-on effect of the vortex shedding frequency should be present. For all the spectrograms, the PSD is normalized to the maximum of the respective measurement.

In Figure 17 and Figure 18, the frequency spectrogram of the velocity fluctuations measured by the hot-wire probe in the wake of the D=0.06m and D=0.09m cylinder are depicted. At all wind speeds, the flow separation is with a turbulent boundary layer. The peaks in this spectrogram of Figure 17 should represent the vortex shedding frequencies of the 0.06m cylinder in the WTA of TU Munich. The vortex shedding frequencies lead to a Strouhal number of St=0.16. Since the Strouhal number is in correspondence to values of the literature and no other fluctuations should be present in the measurement setup, it can be assumed that the spectrogram peaks are connected to the cylinder wake frequencies. The one peak at around 3.5Hz at 20m/s is caused by the wind tunnel eigenmodes, as seen in Figure 16.

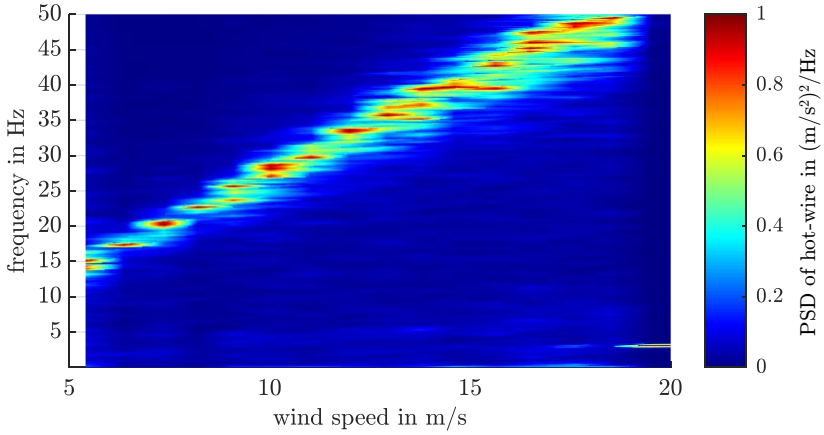

Figure 17: Spectrogram of the wake of the D=0.06m cylinder in the WTA of TU Munich for the outside hot-wire probe.

That this measurement setup leads to the cylinder frequency can be seen in the measurements of the D=0.09m cylinder in Figure 18. If the measured peaks are caused by the vortex shedding of the cylinder, the Strouhal number should remain equal for both cylinders. The peaks in this spectrogram of Figure 18 should represent the vortex shedding frequencies of the D=0.09m cylinder in the WTA of TU Munich. The vortex shedding frequencies lead to a Strouhal number of St=0.16 as well. Hence, this corresponds to the Strouhal number of the D=0.06m cylinder and shows that for both cylinders, mainly the wake frequencies are measured.

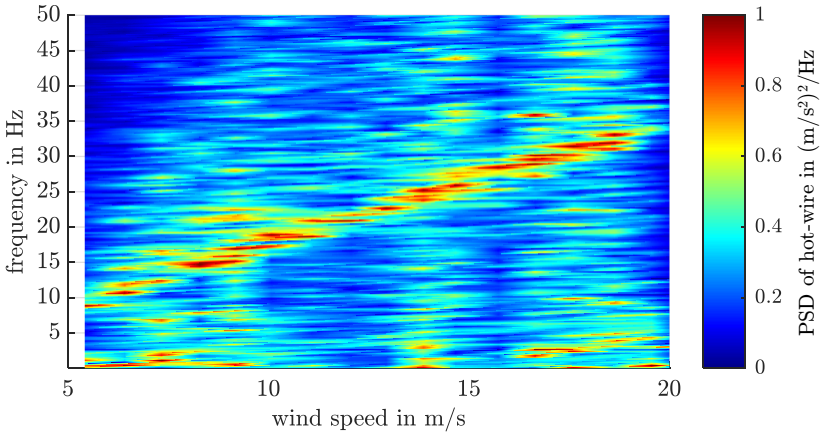

Figure 18: Spectrogram of the wake of the D=0.09m cylinder in the WTA of TU Munich for the outside hot-wire probe.

This shows that in ideal conditions, the Strouhal number for both cylinders is the same. Additionally, the frequencies of the vortex shedding are not influenced by wind tunnel pulsations. These are much lower than the cylinder frequencies.

A high correspondence of the numerical results can be observed by comparing the experimental results with a numerical simulation. The general parameters of the CFD setups are the same as described in 2.2.2. Only the geometric boundaries are adapted to correspond to the experimental setups. A simulation in a generic box domain is conducted to validate the WTA experiments. This box has a length of 72m with the cylinders positioned in the middle at 36m. Its inlet area is A_I=2160m² and therefore the nozzle blockage ratio for both cylinders results in around 0.002%. This nozzle blockage is so small that no interference effects can be expected. With this simulation setup, it can be investigated if the WTA flow is comparable to an ideal flow field without wind tunnel interference effects. The floor of the box has a slip boundary condition to avoid the formation of a boundary layer. This is in correspondence to the experimental setup where the boundary layer is removed right in front of the cylinders by the scoop of the wind tunnel. A mesh refinement around the cylinder is applied to reach a sufficient spatial discretisation. This refinement region is depicted in Figure 19. All simulations are conducted at 15m/s to reduce the numerical effort.

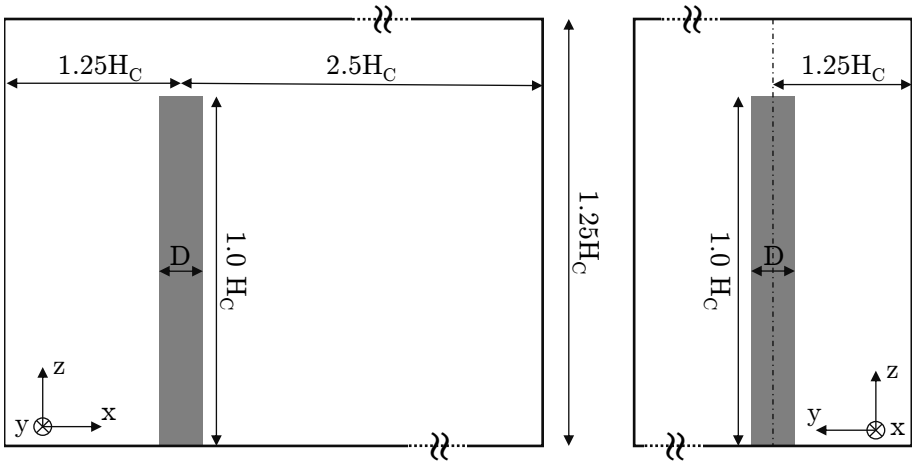

Figure 19: Refinement region around the cylinder for the numerical simulations. Edge length of the refined cells: 2.9mm. Dark grey: cylinder in refinement region.

With the depicted refinement region, an overall number of around 38 million volume cells are derived. Like in the experimental measurements, a physical time of 20 seconds is simulated. An extra four seconds are simulated at the start to allow the flow field to fully develop. The Fast Fourier Transform (FFT) result for the D=0.06m cylinder of the CFD is depicted in Figure 20.

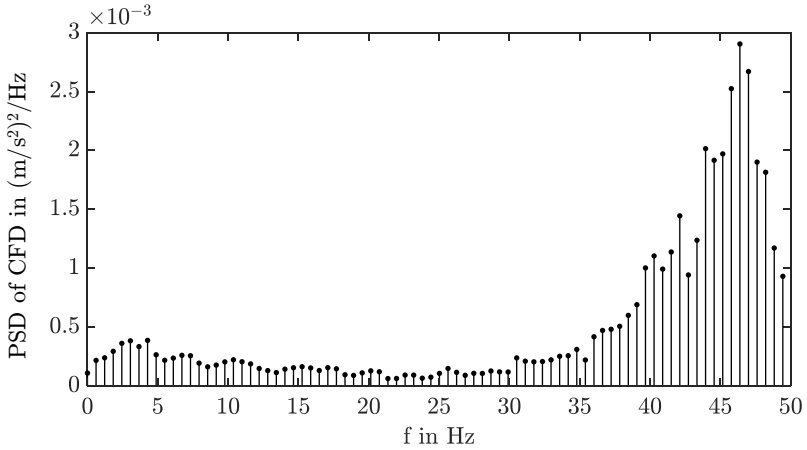

Figure 20: FFT of the CFD velocity in the wake of the D=0.06m cylinder at 15m/s in the Box CFD setup.

Comparing the FFT peak in Figure 20 of the CFD probe point at a wind speed of 15m/s with the measured peak of the WTA, the following can be found. The CFD predicts a Peak at 46Hz. The wake measurement in the wind tunnel suggests a peak at 41Hz. The CFD data is post-processed with the same weighting factors for the hot-wire data as the experiment. The deviation between

41Hz and 46Hz could be caused by the cylinder surface, experimental setup, CFD setup and hot-wire movement. In the CFD setup for these cases, neither the wind tunnel geometry nor the inflow conditions are considered. This could further explain the deviation of the frequencies. Besides the mentioned uncertainties, an overall good agreement can be found. In the next step, the results for D=0.09m of Figure 21 are analysed.

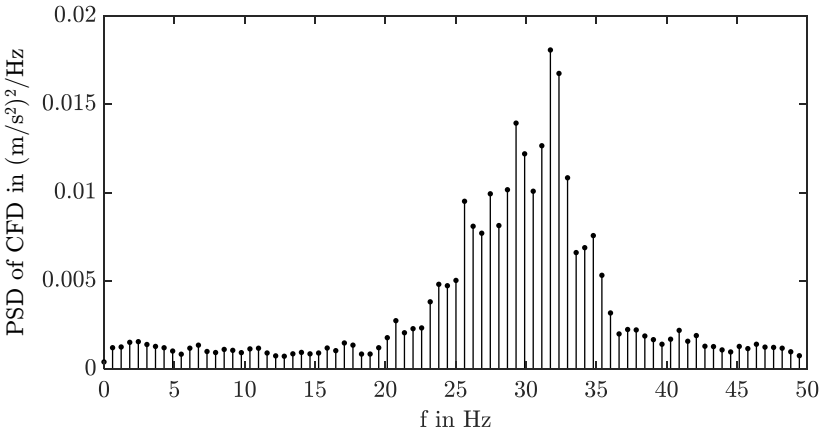

Figure 21: FFT of the CFD velocity in the wake of the D=0.09m cylinder at 15m/s in the Box CFD setup.

Also, for the D=0.09m cylinder, the CFD gives a good result. The CFD predicts a peak at 32Hz, depicted in Figure 21. The wake measurement in the wind tunnel suggests a peak at 27Hz. With the given CFD results, the Strouhal number of the D=0.06m and D=0.09m cylinder is St=0.184 and St=0.192, respectively. Apart from small deviations, two main conclusions can be drawn. Firstly, the Strouhal numbers for both cylinders are almost constant in the ideal simulation with the Box CFD setup, according to the measurements in the WTA. And secondly, taking the aforementioned causes for the deviations into account, the used CFD setup can predict the wake frequencies of a blunt body with overall good accuracy.

Comparing now the results of the WTA with the model wind tunnel derives interesting findings. The setup of the cylinder in the model wind tunnel is depicted in Figure 22 and Figure 23. In the model wind tunnel, the cylinders are mounted 0.185m behind the nozzle exit on a plate. The mounting plate is underneath the nozzle exit and the boundary layer should have a negligible influence on the measured data. With the height of H_C=0.4m, the top of the cylinder is outside of the flow and three-dimensional flow phenomena should be negligible like in the WTA. With a nozzle exit cross-section of A_N=0.056m², the nozzle blockage is 20.5% for the D=0.06m cylinder and 30.7% for the D=0.09m cylinder. Given the high nozzle blockage ratios, it cannot be assumed that the flow is not influenced by blockage effects. This influence will be investigated with the help of numerical simulations. The results will be discussed later. The

positioning of the hot-wire probes related to the cylinders is the same as in the WTA measurements.

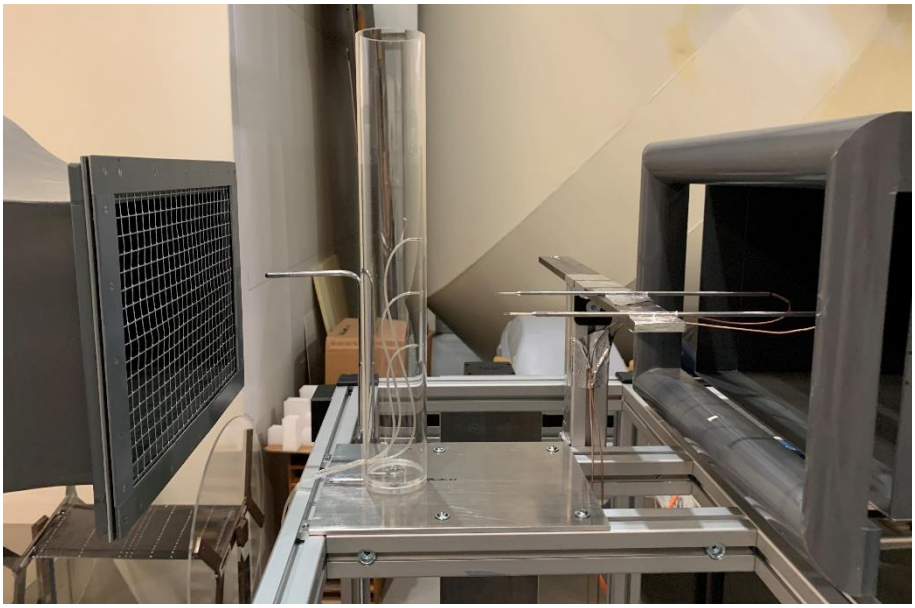

Figure 22: Side view of the cylinder in the model wind tunnel.

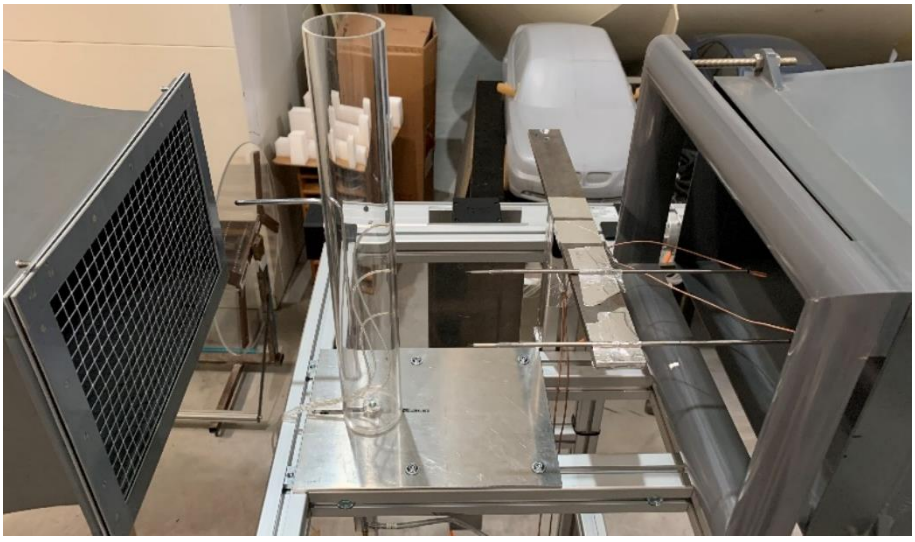

Figure 23: Top side view of cylinder in the model wind tunnel.

As for the investigation in the WTA, it is important to know the eigenmodes of the model wind tunnel for the empty test section. The eigenfrequencies of the model wind tunnel are depicted in Figure 24.

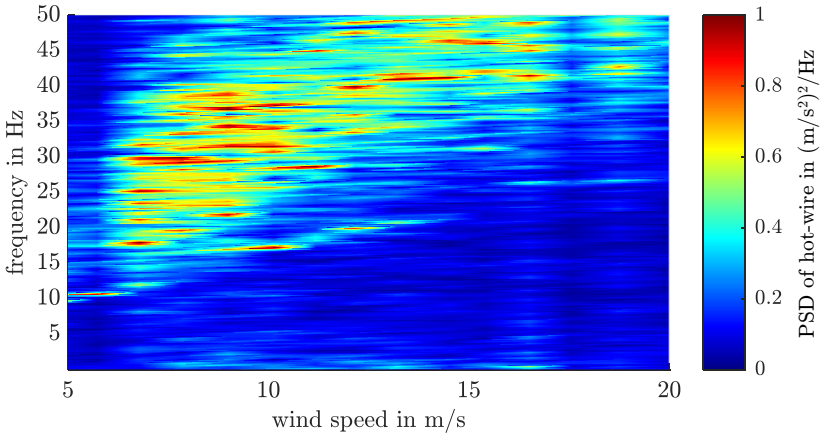

Figure 24: Spectrogram of the empty model wind tunnel test section for the outside hot-wire probe.

In the case of the model wind tunnel, the frequencies of the empty test section are near the natural cylinder frequencies. In literature, a lock-on phenomenon is often described for cases of cylinders in excited flows. Barbi et al. [69] and Konstantinidis et al. [70] excite the inflow of a cylinder experiment with specific frequencies and a lock-on of the cylinder vortex shedding frequency on the inflow frequencies can be observed. For the cases with the lock-on effect, alternating vortex shedding processes are found. Feng et al. [71] made similar findings by exciting the vortex shedding with a pulsed jet at the rear of a cylinder. Due to the fact that the wind tunnel frequencies are near the natural frequencies of the cylinder, an influence on the cylinder frequencies is likely. Additionally, altering vortex shedding processes and a lock-on of the cylinder frequency on the wind tunnel inflow frequencies can be present as in the aforementioned investigations. The results of the D=0.06m cylinder measurements in the model wind tunnel are depicted in Figure 25.

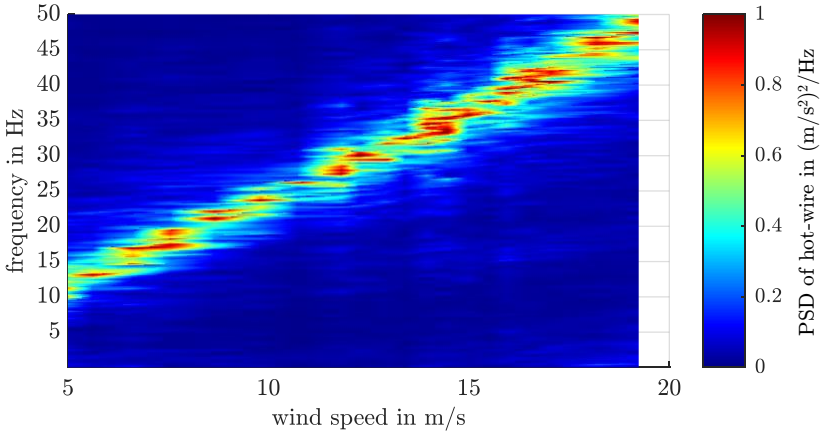

Figure 25: Spectrogram of the wake of the D=0.06m cylinder in the model wind tunnel for the outside hot-wire probe.

The spectrogram in Figure 25 is similar to the measurement in the WTA. The only difference is a slight shift in the cylinder wake frequencies. Compared to the Strouhal number of St=0.16 for the WTA, the D=0.06m cylinder in the model wind tunnel shows a Strouhal number of St=0.14. On the one hand, this deviation can be caused by the difference in the measurement setup and mainly due to the different dimensions of the wind tunnels. On the other hand, the frequency shift could be caused by a lock-on effect between the cylinder and the wind tunnel pulsations, as mentioned in [15], [17] and [45]. To further validate this hypothesis, the spectrogram of the D=0.09m cylinder of Figure 26 is analysed.

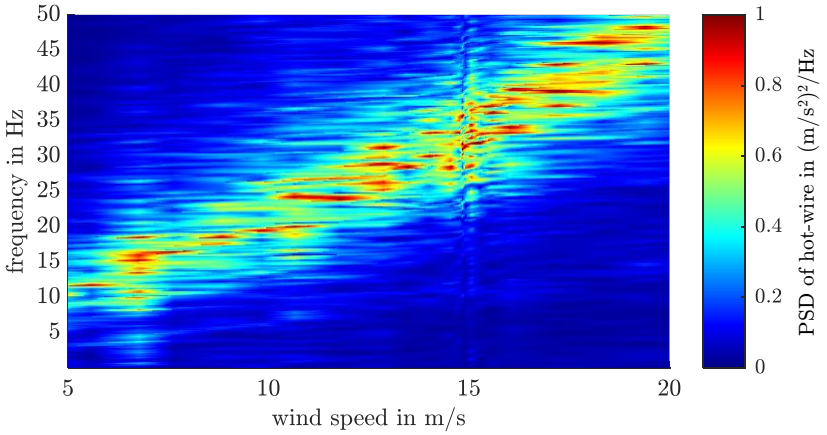

Figure 26: Spectrogram of the wake of the D=0.09m cylinder in the model wind tunnel for the outside hot-wire probe.

In Figure 26, the spectrogram of the wake from the D=0.09m cylinder is shown. As for the D=0.06m cylinder, the frequencies of the cylinder wake are shifted compared to the results from the WTA. This time the shift is even bigger. With a Strouhal number of St=0.20 compared to St=0.16 from the WTA. A lock-on effect of the cylinder wake on the wind tunnel eigenmodes could cause this shift of the Strouhal number. The lock-on effect could also be seen by the fact that the frequencies of both cylinders in the model wind tunnel are very similar. Relying on the lock-on effect, this would mean that the natural cylinder frequencies are shifted because of the wind tunnel frequencies, which are near the cylinder frequencies. This could be an explanation for the different Strouhal numbers in the wake of the cylinder in the model wind tunnel. For the D=0.06m, cylinder the natural frequencies and the eigenfrequencies of the wind tunnel are similar and a resonance effect can be expected. This resonance can be seen by the sharper peaks in the D=0.06m cylinder spectrogram of Figure 25 compared to the relatively wide peaks of the D=0.09m cylinder in Figure 26, which are not in resonance.

To verify that the influence is mainly caused by the model wind tunnel pulsations, the following aspects are investigated. At first, the inflow characteristics are compared. From hot-wire measurements of the empty test

section, the turbulence intensity of both wind tunnels can be calculated. In each wind tunnel, the turbulence intensity is Tu<0.2%. Therefore, the influence of the level of turbulence of the wind tunnel flow can be neglected. But in the time-resolved data of these measurements, an important difference can be found. The temporal evolving structures in the hot-wire signals, analysed with a FFT, show major differences between both wind tunnels. The FFT results for the hot-wire in the middle of the nozzle are depicted in Figure 27.

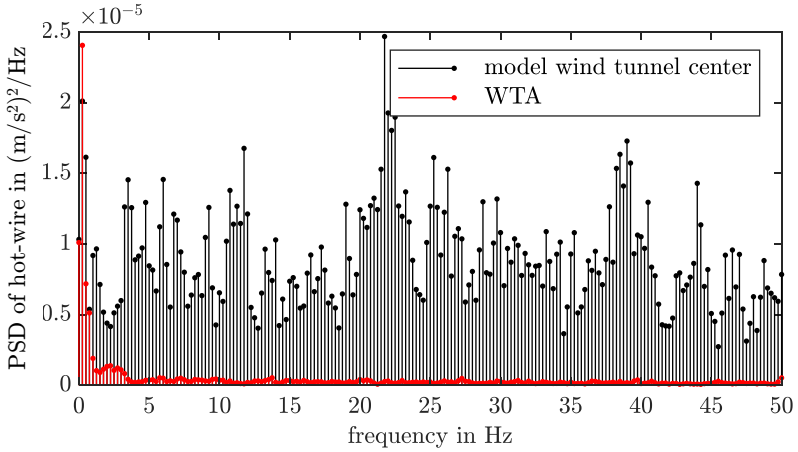

Figure 27: FFT of empty test section flow measured by the hot-wire in the middle for both wind tunnels at 15m/s.

In Figure 27, one can see, despite having a similar turbulence intensity, the fluctuations of the model wind tunnel have a higher PSD over a larger frequency spectrum compared to the WTA, especially for the fluctuations with higher frequencies. The WTA has only low-frequency eigenmodes, but the model wind tunnel has eigenmodes with higher frequencies, e.g. the main peak at 22Hz. The result for the moved hot-wire is depicted in Figure 28.

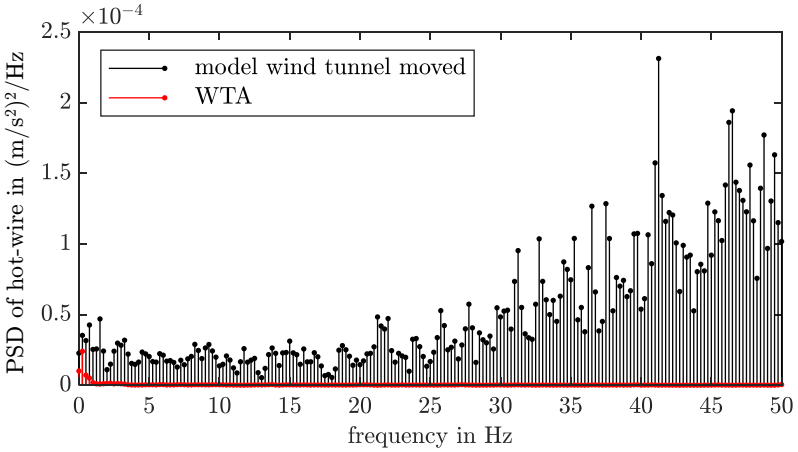

Figure 28: FFT of the empty test section flow measured by the outwards moved hot-wire.

In Figure 28, the power spectral density for the empty test section of both wind tunnels measured with the 0.1m outwards moved hot-wire probe is shown. In the model wind tunnel, the cylinder is nearer to the shear layer and therefore the shear layer has a much higher effect on the cylinder flow. There one can see that the model wind tunnel has highly energetic structures, especially in the range of the cylinder frequencies, e.g. the main peak at 41Hz. These structures with high-power spectral density could lead to a lock-on effect.

To verify that the flow phenomena measured in the model wind tunnel are not only caused by the dimension of the model wind tunnel and blockage effects, a CFD investigation is conducted. First, a simulation of the cylinder with the geometry of the model wind tunnel nozzle and the collector is analysed. For this simulation, a constant inlet velocity of 15m/s is chosen. This helps to evaluate the influence of the wind tunnel geometry since no wind tunnel pulsations are present in the flow field due to the constant inlet velocity. In the second step, the influence of the wind tunnel pulsations is investigated by adding the two main eigenmodes of the model wind tunnel, namely 22Hz and 41Hz, via a time-varying inlet velocity. With this investigation, the influence of the geometry and eigenmodes of the wind tunnel can be differentiated.

The overall parameters, refinement region and boundary conditions for the following CFD investigation are equal to the aforementioned simulations of the cylinders in the Box CFD setup. Different to the Box CFD setup is the added nozzle and collector geometry of the model wind tunnel, which leads to the nozzle blockage ratios of the experimental measurements in the model wind tunnel. All geometries are inside the refinement region used for the CFD analysis of the cylinders in the WTA, depicted in Figure 19. The CFD setup for the model wind tunnel is depicted in Figure 29.

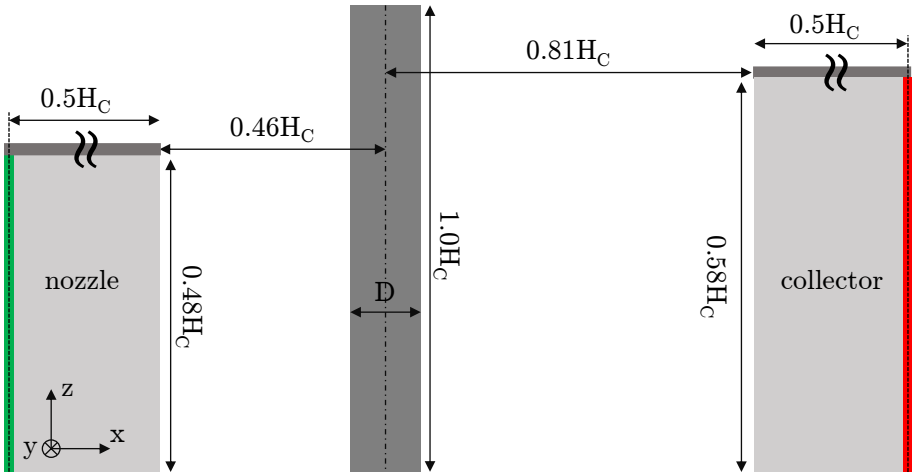

Figure 29: CFD setup with the nozzle and collector geometry of the model wind tunnel. Green: inlet area, red: outlet area, dark grey: cylinder.

With the geometries of the nozzle and collector of the model wind tunnel, the results depicted in Figure 30 can be derived.

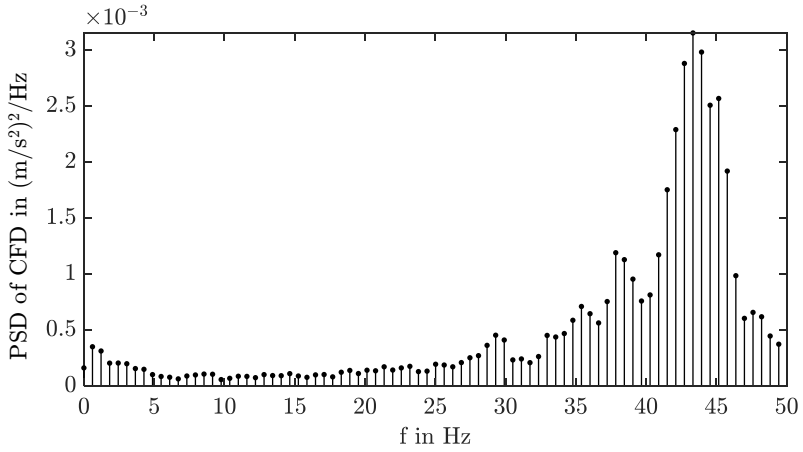

Figure 30: FFT of the CFD velocity in the wake of D=0.06m cylinder with the model wind tunnel geometry.

In Figure 30, one can see that the geometry of the model wind tunnel does not lead to the lock-on effect. A very similar main peak as in the Box CFD setup of Figure 20 can be seen. The small deviation of 3Hz between the model wind tunnel CFD setup and the Box CFD setup can be caused by the influence of the shear layer near the cylinder for the model wind tunnel setup. The influence is small, which can be due to the low intensity of the shear layer. The FFT result for the D=0.09m cylinder is depicted in Figure 31.

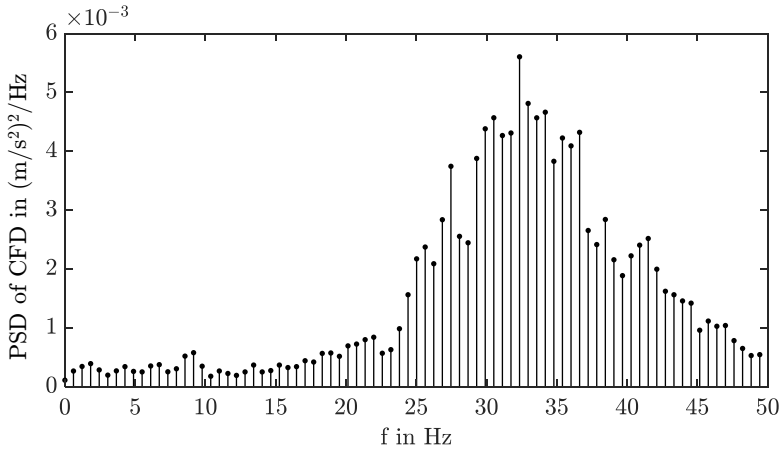

Figure 31: FFT of the CFD velocity in the wake of D=0.09m cylinder with the model wind tunnel geometry.

In Figure 31, it can be seen that the geometry of the model wind tunnel does not lead to the observed lock-on effect. Nearly the same main peak as in the Box CFD setup of Figure 21 is present. The small deviation of 1Hz between the model

wind tunnel CFD and the Box CFD is negligible and shows that the influence of the model wind tunnel geometry is not the cause of the cylinder frequency shift. Even though the D=0.09m cylinder is now more influenced by the shear layer of the model wind tunnel than the D=0.06m cylinder, the frequencies have a higher agreement with the Box CFD setup. Therefore, the influence of nozzle blockage, or shear layer distance to the cylinder, is not the cause of the frequency shift. Another wind tunnel interference effect must cause the frequency shift. This further interference effect is analysed in the following chapter.

3 Unsteady Wind Tunnel Interference Effects in CFD

The numerical simulation is an important tool for the aerodynamic development of a passenger vehicle. To get the most out of it, it is necessary that the results and the flow field prediction of the numerical simulation correlate with the results of the wind tunnel. In the numerical simulation in the previous chapter, the geometry of the model wind tunnel combined with a constant inflow does not lead to the shifted frequencies in the wake of the cylinder. Therefore, another effect must be responsible for the frequency shift observed in the cylinder wake. This effect could be linked to low-frequency wind tunnel eigenmodes. In this chapter, a novel inlet boundary condition for the CFD setup is introduced based on the generic cylinder test case. With this new boundary condition, the unsteady wind tunnel interference effects can be investigated with CFD. The CFD setup with the new inlet boundary condition is then validated and optimised on the basis of the AAWT with an empty test section.

3.1 Transient Inlet Boundary Condition for the CFD Setup

In the FFT results of the empty test section of the model wind tunnel, depicted in Figure 27 and Figure 28, one can see two dominant peaks. The first one is at around 22Hz and the second one is at 41Hz. Adding these frequencies as superpositioned sine waves at the inlet of the CFD setup of the model wind tunnel leads for the D=0.06m cylinder to the result depicted in Figure 32. This method of adding sine waves at the inlet boundary condition of the CFD setup is discussed in more detail in section 3.2.

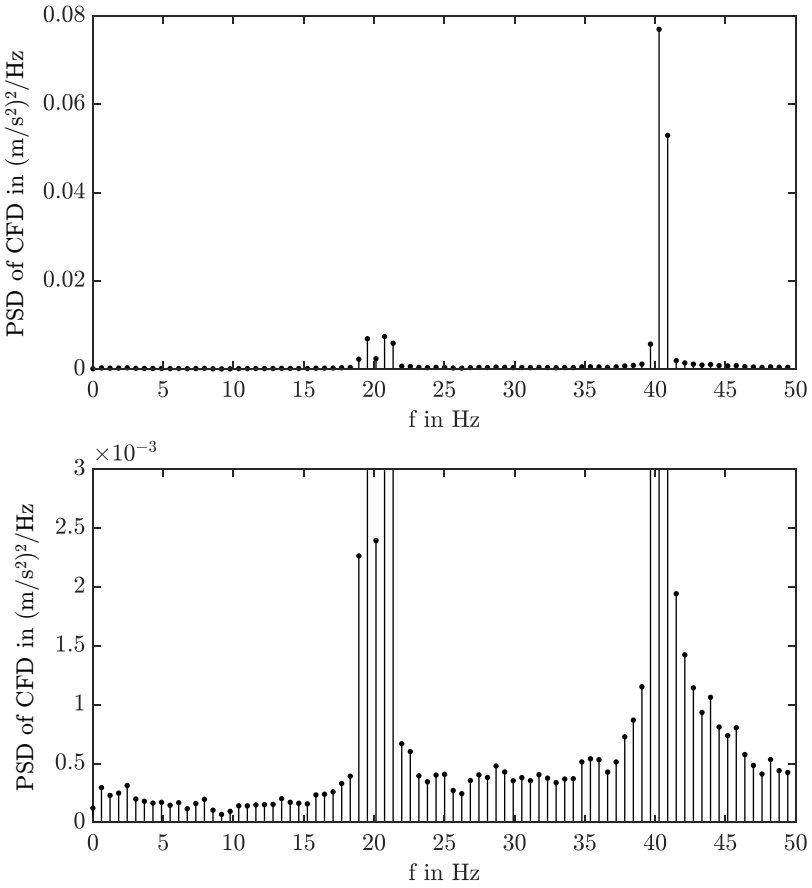

Figure 32: FFT of the CFD velocity in the wake of the D=0.06m cylinder with the model wind tunnel geometry and fluctuating inlet (top). Bottom: y-axis resolution corresponding to Figure 30 to show the shifted frequencies.

The main peak for the cylinder wake is now moved to the inlet frequency of 41Hz. In the bottom part of Figure 32, it can be clearly seen that not only the inlet frequency is a dominant peak, but compared to Figure 30, the whole peak for the cylinder frequency is moved towards the 41Hz peak. This could be caused by the lock-on effect. Additionally, with the fluctuating inflow, one can also see that the peak is much sharper than the peak of the constant inflow CFD, much more like in the experimental results. All in all, the CFD result of the model wind tunnel corresponds better to the experimental result. This result shows that the lock-on phenomenon of the cylinder frequencies in the model wind tunnel is caused by the wind tunnel pulsations. In the spectrogram of Figure 24 one can see that the main peak at 15m/s is at around 37Hz.

The FFT result for the D=0.09m cylinder in the optimised CFD setup with the main peaks of the model wind tunnel is depicted in Figure 33.

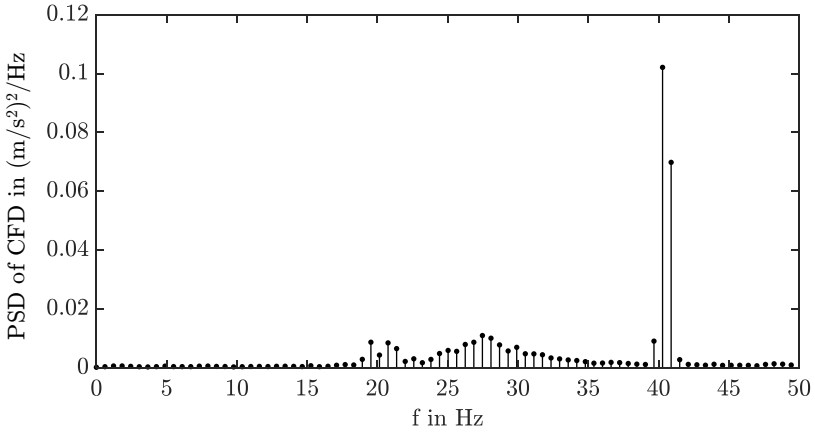

Figure 33: FFT of the CFD velocity in the wake of the D=0.09m cylinder with the model wind tunnel geometry and fluctuating inlet.

In Figure 33, the frequency analysis of the D=0.09m cylinder with the fluctuating inlet is given. With the two frequencies 22Hz and 41Hz from the experimental inflow, at the inlet boundary condition, a frequency shift of the cylinder wake can be observed. Besides the two peaks at 22Hz and 41Hz coming from the inflow, a peak at 27Hz can be seen. This is the shifted cylinder frequency compared to the 32Hz of the constant inflow setup of Figure 31. Two major differences to the D=0.06m cylinder can be stated. Firstly, the frequency of the D=0.09m cylinder is not near both inflow frequencies, but nevertheless, a shift of the wake frequency is seen. Compared to the lock-on effect of the D=0.06m cylinder, the shifted wake frequency is not corresponding to one of the inflow frequencies. Secondly, the peak at 27Hz is not as sharp as the 41Hz peak of the D=0.06m cylinder. This could be due to the fact that the frequency is not locked onto the inflow frequency, as stated in [15]. Also, the not-so-sharp peak of the wake corresponds well with the experimental results given in Figure 25. The peaks in the spectrogram for the D=0.09m are wider than the peaks of the D=0.06m cylinder. Because of the wide range of frequencies in the spectrogram of Figure 25, it is not easy to compare the CFD results. The CFD results for the D=0.09m cylinder in the model wind tunnel show a high agreement with the wide peak range of the experiment, but interestingly enough, a frequency shift and therefore a dependency on the inflow frequencies can be found for the D=0.09m cylinder as well. Optimising the parameters at the inlet could further enhance the correspondence between the numerical and experimental FFT results.

The lock-on of the cylinder wake to the wind tunnel eigenmodes is well represented by using the fluctuating inflow in the CFD setup. In addition to the frequency shifts in the FFT spectra, an influence on the wake structure can also be found in the CFD. In Figure 34, isolines for three specific velocity values of the D=0.06m cylinder wake are plotted. The black lines are the wake contours of the constant inflow. In the case of the fluctuating inflow, the lines are plotted in red. At the isoline of 10m/s, it can be seen that the overall length of the wake in the x-direction is very similar for the fluctuating and constant inflow. A major difference is the width of the wake in the y-direction. The wake with the fluctuating inflow is wider compared to the constant inflow. This can be caused by two flow phenomena. On the one hand, the fluctuating inflow leads to a lock-on phenomenon and alters the flow structure of the wake. This is in accordance with the frequency shift, which can be seen in the FFT spectra. The alternating wake structure due to the lock-on effect can also be seen for the isolines of 5m/s and 8m/s. These lines are different between the fluctuating and constant inflow, which means that the velocity distribution in the wake is different between the forced and natural wake of the cylinder. Another explanation for the different wake structures can be the additional excitement of the wake's shear layer by the additional fluctuations of the wind tunnel pulsations. This higher level of shear layer excitement can also lead to stronger mixing of the shear layer and could cause a wider cylinder wake. Overall, the fluctuations caused by the wind tunnel flow have an influence on the wake of the cylinder and it is crucial to analyse the interference in more detail.

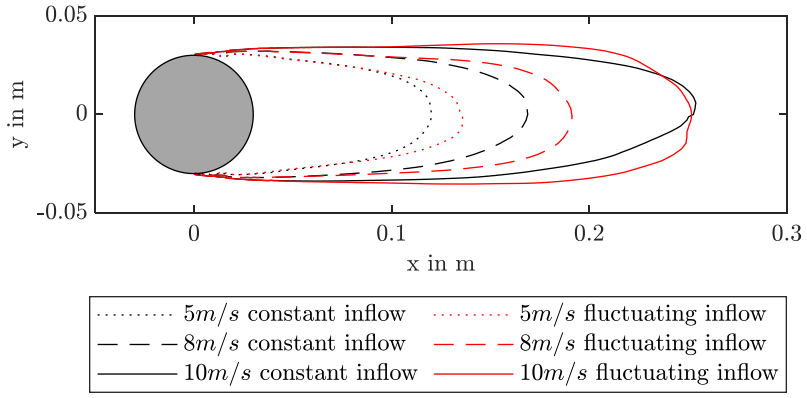

Figure 34: Wake comparison of D=0.06m cylinder. Isolines for 5m/s, 8m/s and 10m/s. Black: constant inflow, red: fluctuating inflow.

Comparing the base pressures of the two cylinders in both wind tunnels supports the hypothesis that the wakes of the cylinders are influenced by a lock-on effect. With the lock-on effect in the model wind tunnel, different base pressures are measured compared to the ideal flow in the WTA. This can be seen in Figure 35. In this comparison, it is worth mentioning that the base pressures

of the model wind tunnel experiments can be affected by the pressure gradient of the model wind tunnel. Therefore, the overall level of pressure between both wind tunnels is only partially comparable. However, what can be seen is that the base pressure behaviour for different wind speeds of the D=0.09m cylinder in the model wind tunnel is comparable to the measurements in the WTA. The 0.06m cylinder, which is mostly affected by the eigenfrequencies of the model wind tunnel, has a different base pressure development with increasing wind speed compared to the other three curves. This leads to the assumption that also in this investigation regarding the base pressure, the wind tunnel pulsations are critical for the flow around the cylinder.

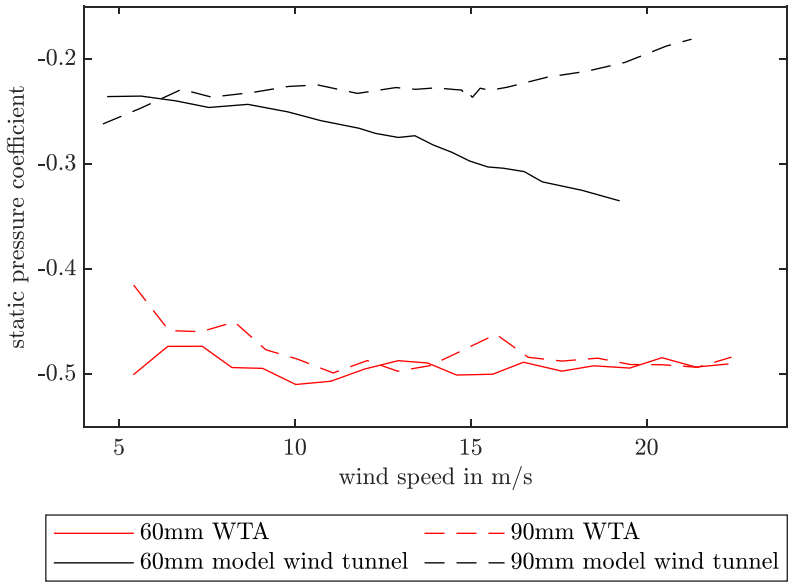

Figure 35: Comparison of the base pressures for both cylinders in both wind tunnels.

This investigation on the wake of the cylinder in different wind tunnels shows that the background flow of the wind tunnel leads to frequency shifts. The eigenfrequencies of the model wind tunnel in the cylinder test are causing a lock-on effect of the cylinder wake to the wind tunnel pulsations. This phenomenon is not correctly predicted by the current CFD setup because the low-frequency wind tunnel pulsations are not simulated. The first try of adding sinewaves to the velocity boundary condition for the generic cylinder test shows that the frequency shift and therefore the lock-on effect can be approximately reproduced. In combination with the findings and recommendation of Sebald et al. [38] to include wind tunnel pulsations for correctly predicted flow fields in a wind tunnel, an optimisation of the current CFD setup is needed. In the case of the generic cylinder test, this optimisation is done with an adapted velocity boundary

condition. This new boundary condition allows the velocity at the inlet of the nozzle to fluctuate with two added sine waves. This enables the flow out of the CFD nozzle to fluctuate with two frequencies, similar to the flow of the experimental model wind tunnel. First results show that a higher correlation of the cylinder wake frequencies to the experimental frequencies can be achieved by adding the sine waves with the eigenfrequencies of the model wind tunnel. Also, the need for further optimisation is shown because the correlation between the numerical and experimental results of the time-resolved flow field is improved, but still, a deviation remains. Further optimisation of the CFD setup for the vehicle investigations is based on the AAWT with an empty test section and the eigenmodes of the AAWT.

3.2 Validation and Optimisation of the Updated CFD Setup

A huge deviation is caused by the wind tunnel pulsations, which are not present in the current CFD setup. Therefore, the frequency shift they are causing is not simulated in the CFD setup. An optimisation of the CFD boundary conditions is needed to correctly predict the transient numerical flow field. In the following chapters, a new boundary condition and its influence on the flow field and aerodynamic results are investigated. The comparison of the new CFD results with experimental data and its evaluation closes the chapter.

For the comparison of the experimental data, it is necessary to include the geometry of the wind tunnel. This is important because of the wind tunnel interference effects described in chapter 1.2, which are related to the wind tunnel geometry. In the works of Jiang et al. [72] and Josefsson et al. [73], it is shown that including the geometry of the wind tunnel in the CFD increases the correlation between the numerical and experimental results. Therefore, in this work, a partial model of the AAWT geometry is used as domain for the CFD optimisation. This ensures that the interference effects of the wind tunnel geometry itself are represented, leaving the low-frequency eigenmodes and pulsations as one of the last flow phenomena to add to the AAWT CFD setup.

For the optimisation of the CFD setup, the empty test section of the AAWT will be used. The empty test section has the advantage that the computational effort is relatively low due to the lower number of cells compared to the simulation with a vehicle in the test section, see Table 3. Furthermore, a second advantage is that without a vehicle in the test section, deviations between the numerical and experimental setup are reduced. Not only smaller differences in the geometry between the vehicle and the virtual vehicle model can be avoided, but also the complex flow field of a passenger vehicle is excluded for the basic CFD setup optimisation. So, the main focus is only on the wind tunnel flow itself and is not interfered by the vehicle flow.

As a basis for the evaluation of the optimised CFD setup, different measurements are conducted in the empty test section of the AAWT. With the hot-wire probe and the Prandtl-probe, which are described in chapter 2.1.3, gradients in the test section and in the shear layer of the wind tunnel jet are measured. The time-averaged and time-resolved measurement results help to compare all types of flow characteristics in the wind tunnel. All measurements are conducted at a wind speed of 38.89m/s and are temperature corrected. This is necessary because the measurements take place on different days and a constant temperature cannot be ensured. To simplify the boundary conditions for the CFD comparison, the rolling road system of the AAWT is disabled and the suction of the boundary layer is covered. This results in a simple stationary floor, which can easily be simulated. More details of the boundary conditions and the wind tunnel geometry are given in the following chapter.

In Figure 36, the empty test section of the AAWT is shown, photographed from the nozzle exit looking at the collector. In the lower part of the image, the black mats can be seen, which are used to cover the boundary layer suction.

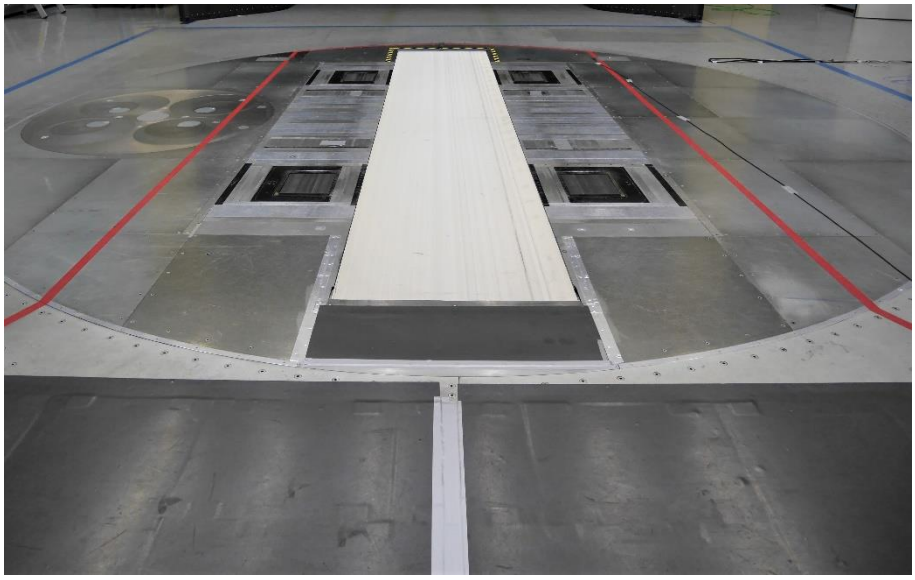

Figure 36: Floor of the empty test section of the AAWT. Photographed from the nozzle exit looking to the collector. Black mats to cover the boundary layer suction.

3.2.1 Empty Test Section Simulation Setup

For the simulations of the AAWT geometry, a partial model of the wind tunnel is used. This model contains the settling chamber, the nozzle, the test section, the collector and the diffusor. The inlet of the CFD domain is the area upstream of the settling chamber. It is located 19.4m in front of the reference

point of the CFD domain in the x-direction. The reference point is the centre of the wind tunnel scale turning table at a height of z=1.0m above the floor and in the middle in the y-direction, namely y=0m. From the reference point, which is considered as x=0m, the nozzle exit is at x=-4.0m and the collector starts at x=5.5m. The boundary conditions for the walls of the domains are described in chapter 2.2.2. Due to the stationary floor of the experiment and the closed boundary layer suction, all walls are defined as friction walls in the CFD setup. The inlet and outlet regions are defined with a velocity boundary conditions. The wind speed at the inlet is set corresponding to the contraction ratio of the nozzle, that the velocity u_∞ is 38.89m/s at the reference point. The resulting velocity distribution in a side view of the CFD domain of the AAWT with empty test section can be seen in Figure 37.

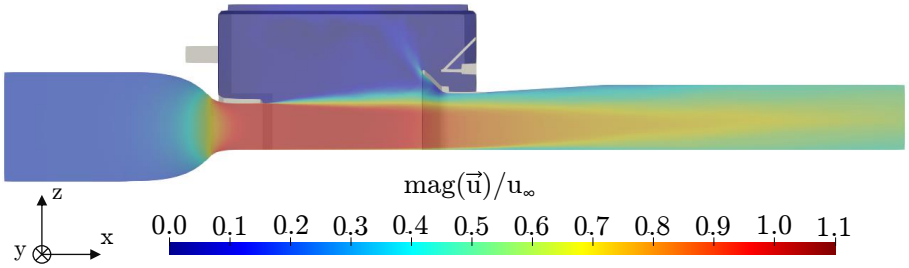

Figure 37: Side view of the CFD domain of the AAWT with empty test section. Distribution of the velocity magnitude at y=0m.

This CFD domain contains approximately 52 million volume cells, which are mainly in hexahedral form. For the test section itself and for the shear layer starting at the nozzle exit, additional refinement regions are needed to correctly simulate the small vortical structures at the start of the shear layer of the wind tunnel jet. The refinement regions are in accordance with Collin [12], where a good agreement of the simulated shear layer with the experimental results from wind tunnel measurements is shown. The mesh at y=0m is depicted in Figure 38 with a coarse overview of the whole domain at a) and a detailed view of the refinement regions at b). The smallest cells have an edge length of 2.9mm.

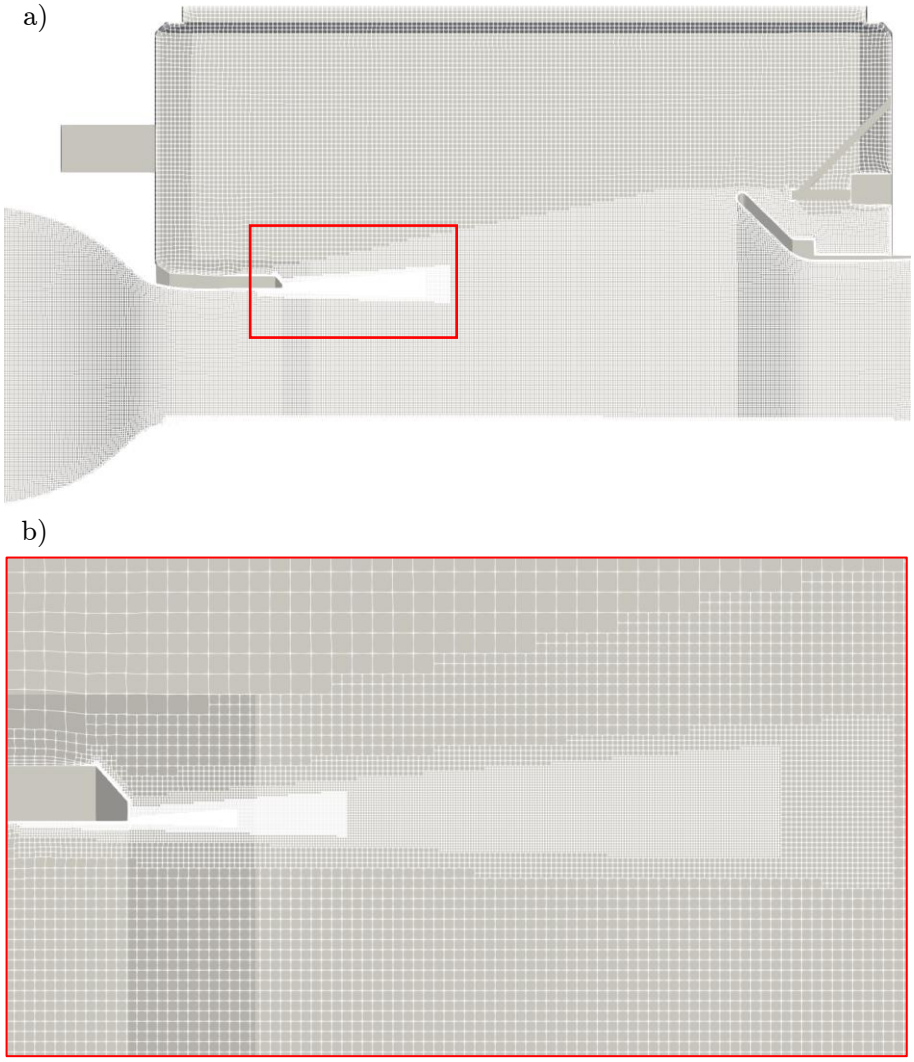

Figure 38: Mesh of the AAWT CFD domain. a) overall mesh in the domain and b) detailed view on the refinement regions of the shear layer.

3.2.2 Experimental and Numerical Results

After introducing the CFD domain of the empty test section AAWT, now flow field characteristics like gradients, which are used for the validation of the CFD setup, will be explained. The first flow field characteristic of the wind tunnel used as a reference is the pressure distribution along the test section at y=0m. The pressure distribution is influenced by the shear layer, the nozzle exit, the boundary layer at the floor and the pressure build-up in front of the collector. Having a pressure distribution in the CFD, which correlates with the experimental measurements, means that the overall flow of the CFD has a good

agreement with the wind tunnel experiment. The pressure distribution for the AAWT is given in Figure 39.

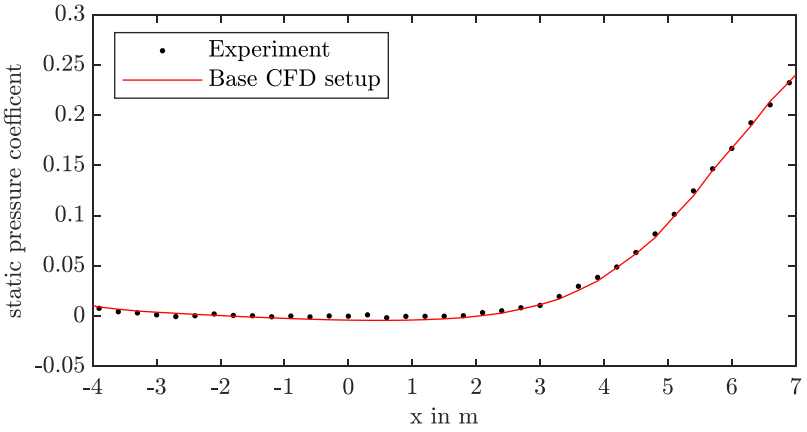

Figure 39: Pressure distribution of the AAWT test section in y=0m and z=1.0m.

The pressure distribution in the AAWT is based on the static pressure coefficient. The distribution starts at x=-4.0m at the nozzle exit and ends at x=7.0m in the diffusor of the AAWT. The pressure gradient, like all following gradients is measured at a height of z=1.0m. As mentioned before, the reference point for all graphs at x=0m is the AAWT scale centre. The black dots represent the measurement points in the AAWT experiment. The boundary layer suction is covered and deactivated for all measurements and simulations. Because of that, no increase in pressure at the nozzle exit can be seen. Downstream of the nozzle exit, the static pressure coefficient is relatively constant until the pressure build-up in front of the collector. This pressure build-up starts at around x=2.0m. In Figure 39, the numerical results are derived from the simulation setup described in chapter 2.2.2. This setup is seen as the base reference and the starting point of the following CFD optimisation and is therefore called "Base CFD setup". The pressure distribution of the CFD has an overall good agreement with the experimental data. Therefore, the quality of the numerical prediction of the overall flow field of the AAWT experiment is good. To further validate the simulation setup and the boundary conditions, the wind speed in the test section is evaluated in Figure 40.

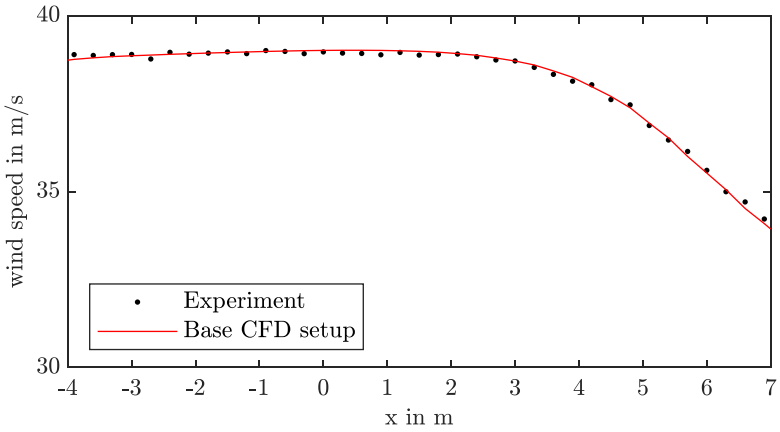

Figure 40: Wind speed in the test section of the AAWT in y=0m and z=1.0m.

The wind speed of the CFD corresponds well with the experimental results of the AAWT. In this graph as well, the black dots are the measurement points of the experiment. Deviations can be seen at the beginning and at the end of the gradient at x=-4.0m and x=7.0m. These deviations are smaller than 0.5% and can be caused by small fluctuations of the averaged wind speed of the AAWT measurement. Despite these small deviations, an overall good agreement of the wind speed in the test section for the numerical and experimental data can be found. This means that the boundary conditions are capable of predicting the correct wind speeds.

The gradients of Figure 39 and Figure 40 are based on time-averaged flow field results. As mentioned before, in this work, the focus is on the time-resolved flow field and the transient interference effects of wind tunnels. Therefore, the two given gradients are a good measure for the validation of the time-averaged flow field but are not suitable for time-resolved investigations. One main flow characteristic, which is of high interest, is the level of fluctuations in the jet of the wind tunnel. These fluctuations are present in the wind speed of the jet and can be characterized by different parameters. One parameter can be the intensity of the fluctuation. This intensity can be evaluated, e.g. with the turbulent kinetic energy, which takes the fluctuations of the wind speed around an average flow speed into account. The turbulent kinetic energy (TKE) is defined as

$$k=\frac{1}{2}\left(\overline{(u')^2}\right) \tag{7}$$

with

$$u'=u-\bar{u} \tag{8}$$

being the difference of the instantaneous velocity from the mean flow speed. In this case, the TKE of the experiment is based on the measurement results of the single-wire hot-wire probe. Therefore, the fluctuations are spatially resolved in only one dimension. To enable a comparison of the one-dimensional TKE of the experiment with the CFD results, the weighting factors of Table 2 are applied to the corresponding velocity components of the simulation to get the same one-dimensional TKE results. The TKE of the experiment and the base CFD setup are given in Figure 41. There a deviation of the TKE gradient of the CFD from the experimental results can be seen. The single measurement points have a variance between them. This is mainly caused by the limited measurement time for each point. Extending the measurement time should even out the huge discrepancies between the different measurement points. But since wind tunnel capacities are very limited and costly, the measurement time for the many points had to be shortened. To get a comparable curve for the validation and optimisation of the CFD, a 5th-order polynomial curve is fitted to the measurement points. The huge discrepancy between the CFD and the experiment starts at around x=-1.0m. This discrepancy indicates that the time-resolved flow field is not predicted well in the CFD. This deviation in the TKE gradient needs to be removed to ensure a good agreement between the numerical and experimental results. This will be the focus of the CFD optimisation. The optimisation of the time-resolved flow in general is the focus of this dissertation and the TKE gradient gives an efficient insight into the time-resolved flow field.

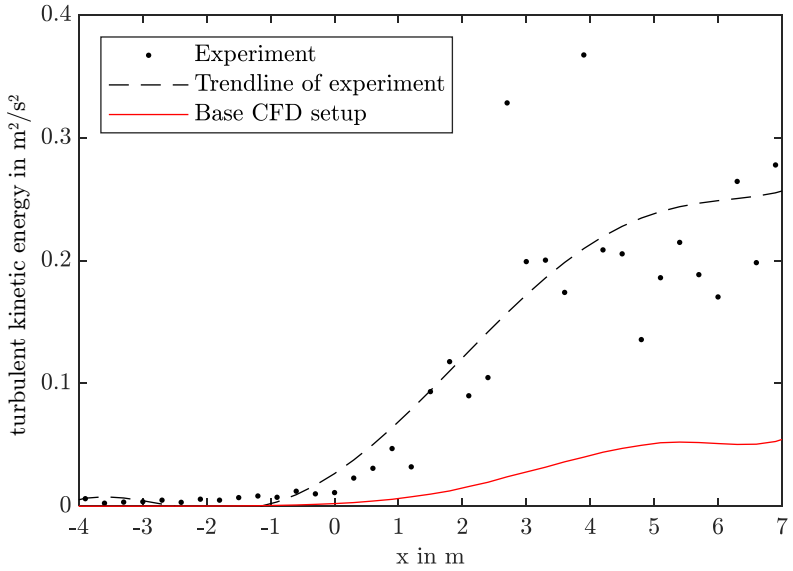

Figure 41: Turbulent kinetic energy distribution of the AAWT in y=0m and z=1.0m.

In Figure 41, it can be seen that for the TKE gradient of the AAWT experiment, the intensity of the fluctuations is relatively low and constant from the nozzle exit to the centre of the wind tunnel scale at x=0m. After the reference

point, an increase in TKE can be observed. This increase of TKE starts to level out at around x=4.5m. Shortly after this, section the collector inlet is positioned. The strong increase of TKE from x=0m until x=4.5m could be caused by the shear layer, which is gaining in size and turbulent energy downstream of the test section. At x=0m, the shear layer could be so wide and energetic that the vortical structures of the shear layer have an influence on the hot-wire measurement in the middle of the jet. That the increase of TKE discontinues shortly before the collector could also be related to the shear layer, which is stopped or decelerated at the collector inlet. This deceleration reduces the rate of the TKE increase. How the shear layer is evolving and what influence it has on the different gradients of the test section will be discussed in more detail later in this work. Nevertheless, the overall TKE level in the base CFD setup is lower compared to the experiment. This indicates that the CFD setup misses certain velocity fluctuations of the AAWT experiment. Additionally, since the increase of TKE from x=0m on is not that strong compared to the experiment, the shear layer of the simulation seems to be predicted with a deviation from the AAWT shear layer.

In Figure 41, for the CFD results, only the resolved TKE is given. The measured TKE of the experiment is strictly speaking comparable to the total TKE of the simulation, which contains the resolved and unresolved TKE. The unresolved TKE is the amount of TKE modelled by the turbulence model and will not be considered in the following CFD optimisation. The reason for that is that the amount of unresolved TKE is an order of magnitude smaller than the resolved TKE. The unresolved TKE for the given gradient in Figure 41 has a range from $0.0007 m^2/s^2$ up to $0.0014 m^2/s^2$. Especially in the crucial region from x=-1.0m to x=7.0m, where the highest deviation between the experiment and the CFD can be found, the TKE of the base CFD setup has values of up to $0.05 m^2/s^2$. The experiment has a TKE of up to $0.26 m^2/s^2$. Therefore, the unresolved TKE is orders of magnitude lower than the resolved TKE and has a negligible influence on the total TKE and on the reduction of the deviation between the numerical and experimental data. This is the reason why the unresolved TKE will not be considered for the optimisation but will be taken into account for the final solution.

Next to the TKE, which indicates how intense the fluctuations are, the temporal characteristics of the fluctuations are important as well. This will be evaluated with a FFT of the flow's velocity at the reference point x=0m. The FFT of the experiment and the base CFD setup is given in Figure 42.

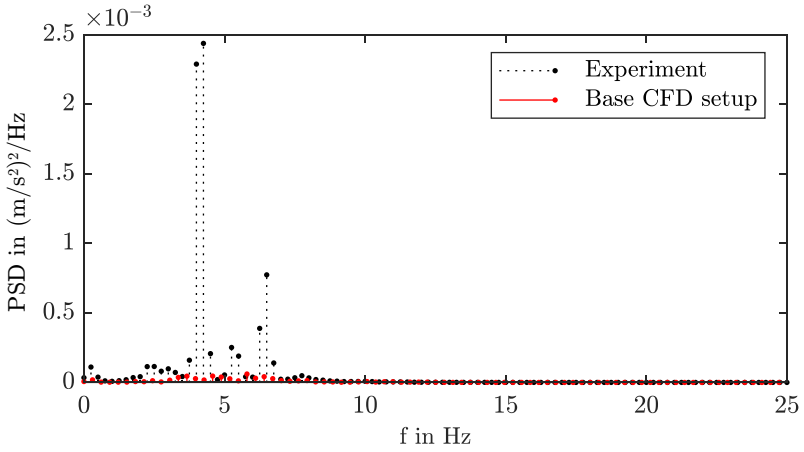

Figure 42: FFT of the flow measured by the hot-wire in the AAWT at x=0m, y=0m and z=1.0m.

In Figure 42, for both FFTs, the data is collected at the scale centre in z=1.0m. The velocity components of the CFD are scaled according to the hot-wire weighting factors from Table 2 to enable the comparison, like for the TKE comparison. Overall, in the empty test section of the AAWT at the measurement point, only low-frequency fluctuations are present in the flow. For the experimental data, a peak at 4.25Hz can be seen. A second peak is present at 6.5Hz. These peaks are in accordance with the investigations of Wickern et al. [15] and Evert et al. [20], who found peaks at similar frequencies in the empty test section of the AAWT. These peaks of the AAWT are the low-frequency eigenmodes of the wind tunnel flow. The additional peak of 2.4Hz from Wickern et al. [15] can be found in the FFT of the experimental data as well, but only with a small amplitude. It is worth mentioning that the previously mentioned ARC system is not active at a wind speed of 38.89m/s, which is the standard wind speed for the CFD optimisation.

To understand the mechanisms, which are causing the fluctuations, it is helpful to apply the resonance formulae of chapter 1.2. Using equation (1) to get the hydraulic nozzle diameter for the AAWT nozzle results in a diameter of D_h=3.27m. Combining the hydraulic nozzle diameter with the frequency of the main peak, namely 4.25Hz, with the wind speed of 38.89m/s, equation (2) gives a Strouhal number of St=0.36. This Strouhal number is very close to the Strouhal number observed by Wickern et al. [15], who suggested the vortex shedding at the nozzle exit to be at around St=0.34. Therefore, the main peak at 4.25Hz can be linked to the vortex shedding of the vortex ring at the nozzle exit. In [15], frequency peaks are observed, which are related to standing waves in the wind tunnel duct. Corresponding to these peaks are the peaks at 2.4Hz and 4.25Hz of this dissertation. Using equation (3) with a duct length L=120m, the second and third modes are at 2.86 Hz and 4.29Hz, respectively. In contrast to [15], the third mode of the standing duct resonance corresponds well to the measured 4.25Hz peak. The second mode of the duct resonance fits the measured 2.4Hz not so well

at the wind speed of 38.89m/s. Interestingly enough, the third mode of the duct resonance corresponds well with the vortex shedding frequency at the nozzle exit. The main peak of the CFD setup is at 3.66Hz and is not in correspondence with the experimental results. This could be caused by the absence of the whole wind tunnel duct in the CFD setup. Without the wind tunnel duct and an incompressible CFD solver, the duct resonance mechanism cannot be simulated and no lock-on effect that would result from it is present. According to the aforementioned literature, like [15] or [17], a lock-on and resonance effect of those resonance mechanisms is expected. This can be seen as a first evidence for the lock-on present, which is present in the wind tunnel experiment but not in the CFD. The frequency of the CFD vortex shedding is not equal to the experimental results because of the absence of the whole wind tunnel duct. The last main peak from the FFT of the experiment is the 6.5Hz peak. Using equation (6) for the edge-tone frequency, the tenth mode of the edge-tone feedback equation results in a frequency of 6.6Hz. The 6.5Hz peak could therefore be linked to the edge-tone feedback between the nozzle and the collector of the AAWT.

Comparing the overall spectrum of the FFT of the base CFD setup to the experimental results shows that not only the amplitudes of the CFD peaks are much lower, but also the frequencies are not equal to the experimental FFT. This could be caused by different reasons. As mentioned before, the frequency shift could be related to the missing lock-on effect resulting from the resonance mechanism of the whole wind tunnel duct. The CFD setup is only a partial model of the wind tunnel and parts of the wind tunnel duct are not included in the simulation. The absence of the whole wind tunnel duct leads to the problem that certain resonance effects of the duct cannot be simulated with the used CFD setup. The absence of certain resonance mechanisms could also be the explanation for the overall lower level of fluctuations in the flow of the numerical wind tunnel flow. In the TKE gradient, it was already shown that the intensity of the fluctuations is lower for the CFD result compared to the experiment, but now in the FFT, the amplitudes of the FFT peaks are lower as well. Furthermore, the base CFD setup is based on an incompressible solver, which means that aero-acoustic resonances cannot be simulated. All in all, the absence of resonance effects in the base CFD setup could explain the frequency shift and the lower amplitude of the FFT peaks compared to the experiment. The cause for these deviations and their reduction in an optimised CFD setup will be discussed in the following chapter in more detail.

The FFT results are very important for the CFD optimisation because they give an insight into not only the intensity of the fluctuations but also their frequencies and if they are shifted compared to the experiment. Especially the frequency shifts of the CFD are of high interest because, with this knowledge, transient wind tunnel interference and resonance effects can be investigated. Therefore, in the first step, a CFD setup is needed, which predicts the correct wind tunnel flow with fluctuation frequencies that fit the experimental ones.

The last flow characteristics to evaluate the quality and correctness of the predicted wind tunnel flow of the CFD are shear layer gradients. Collin [12] used shear layer gradients to validate the numerical results of his AAWT simulations. The shear layer gradients are based on the time-averaged wind speed across the shear layer. Collin showed in his work that the shear layer at different locations in the test section corresponds well with the experimental results. With the results, he draws the conclusion that the used AAWT geometry and boundary conditions of the CFD are able to predict the flow field. The prior results of the TKE gradient and the FFT spectrum show that certain parameters of the wind tunnel flow are not correctly predicted by the used boundary conditions. The shear layer gradients will be part of the CFD optimisation to evaluate the influence of new boundary conditions on the simulated shear layer. The goal is to keep the shear layer gradients like in Collin [12], where a good agreement to the wind tunnel measurements is shown.

The shear layer gradients are measured in different positions at x=-2.5m, x=0m and x=2.7m from the reference point in scale centre at x=0m. The shear layer in the y-direction is measured at a height of z=1.0m. The measurements are conducted with the hot-wire probe. The velocities are normalized to the wind speed u_∞ of 38.89m/s at scale centre. The shear layer gradient at x=-2.5m is depicted in Figure 43.

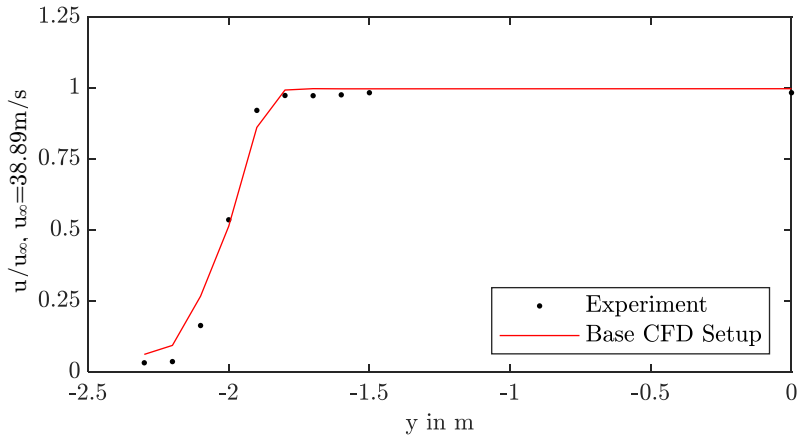

Figure 43: Shear layer gradient in the AAWT at x=-2.5m in z=1.0m from y=-2.3m to y=0m.

In the shear layer gradient at x=-2.5m, an overall good agreement of the simulated shear layer to the experimental measurements can be found. Nevertheless, a deviation between x=-1.8m and x=-2.3m remains. In this region, the simulated shear layer has a different velocity gradient. This needs to be addressed in the following optimisation.

A similar conclusion can be drawn from the other shear layer gradients at x=0m and x=2.7m, depicted in Figure 44 and Figure 45. The shear layer gradient

of the simulation, at the outside of the shear layer has higher normalized velocities compared to the AAWT measurements. Next to the higher velocities at the outside, the shear layer at x=0m in Figure 44 has too low velocities at the inside of the jet's shear layer in the region of y=1.6m to y=2.0m. The simulated shear layer gradient at x=2.7m, depicted in Figure 45, has similar deviations to the experiment as the other ones. The numerical simulated shear layer has an overall higher velocity compared to the experiment.

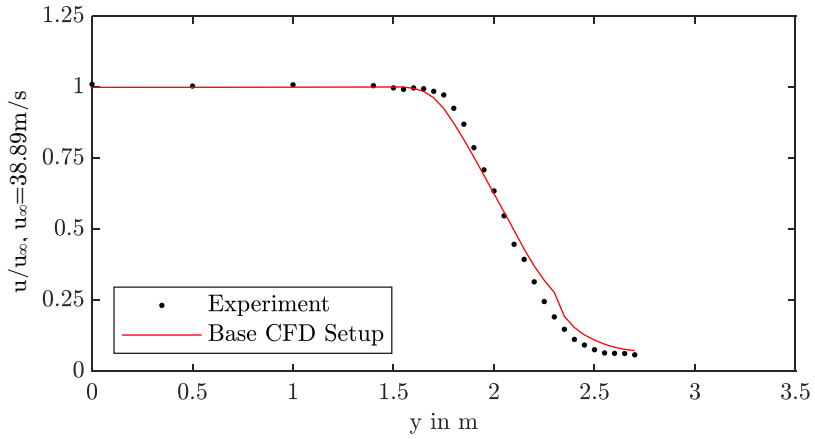

Figure 44: Shear layer gradient in the AAWT at x=0m in z=1.0m from y=0m to y=2.7m.

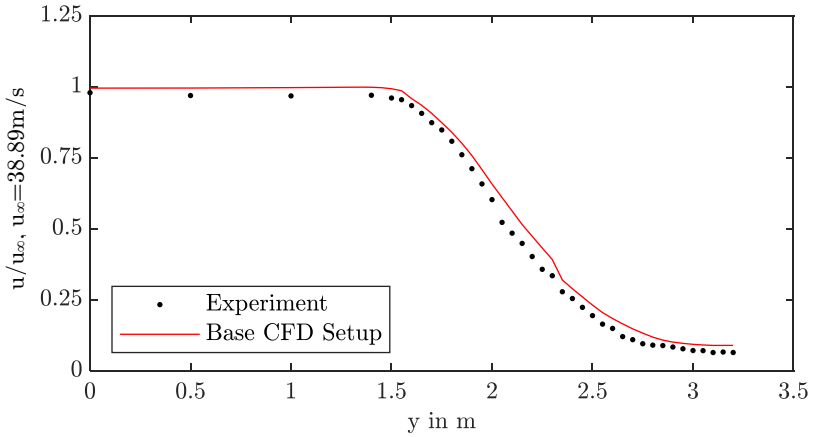

Figure 45: Shear layer gradient in the AAWT at x=2.7m in z=1.0m from y=0m to y=3.2m.

For the optimisation mainly the shear layer at x=2.7m will be used. The theory behind this decision lies in the spatial development of the shear layer. It is assumed that the shear layer is evolving streamwise of the jet. If there are errors at the beginning of the shear layer, the shear layer gradient downstream will be incorrect as well. The other way around, when the shear layer gradient

at a position downstream is correctly predicted by the CFD, it can be assumed that the shear layer upstream is also predicted correctly. For a final solution, all shear layer gradients have to be evaluated, but for the optimisation process, the focus is on the shear layer at x=2.7m.

The given gradients and the FFT spectrum in the scale centre are used for the optimisation of the CFD setup. It is shown that the base CFD setup deviates partially from the experimental results from AAWT measurements, especially for the time-resolved flow field. For the shear layer gradients, a deviation can be seen as well. To minimize these discrepancies in the CFD results, an optimisation is carried out in the following chapter.

3.2.3 CFD Setup Optimisation

The boundary conditions of the CFD setup must be adapted to reduce the discrepancies between the numerical and experimental results. Sebald et al. [38] give some first results on how to improve the numerical results with new boundary conditions. Their focus, however, is strongly on the improvement of the TKE gradient. In this dissertation, additional flow field characteristics are taken into account for the evaluation of the simulated flow. At first, they added a boundary condition at the inlet of the CFD domain, which generates synthetic turbulence. The level of turbulence decays quickly in the area of the settling chamber. According to [38], this is caused by the coarse mesh in this area. A coarse mesh is also present in the used CFD setup of the AAWT, depicted in Figure 37. The conclusion is that this boundary condition needs a mesh with a finer resolution so that the turbulence can be transported through the whole domain. This requires more computing capacity and is therefore not a suitable solution. Furthermore, the turbulence screens in front of the settling chamber eliminate vortical structures in the y- and z-direction. This makes it unnecessary to add three-dimensional turbulent structures to the CFD setup. Additional to the findings of [38], the synthetic turbulence boundary condition has a further disadvantage. The main point of the numerical deviations is the FFT spectrum compared to the experimental result. In the numerical setup, the eigenfrequencies of the AAWT are not simulated correctly due to the lack of the whole wind tunnel geometry and the incompressible solver used. The synthetic turbulence results in random velocity fluctuations, which cannot be compared with the wind tunnel eigenmodes. The synthetic turbulence would need additional information about the temporal characteristics of the fluctuations to enhance the numerical FFT result. This cannot be done with the synthetic turbulence boundary condition. Overall, this method is not effective in representing the eigenmodes of the wind tunnel in the CFD setup and in reducing the deviations between the numerical and experimental data.

Sebald et al. [38] also conclude that another method is required to optimise the numerical results. In the next step, they add the wind tunnel eigenfrequencies

to the CFD setup with a measurement signal from the experiment. Their goal is to replicate the flow conditions in the settling chamber of the AAWT with the CFD setup. The flow conditions in the settling chamber are chosen because the inlet of the CFD domain is in front of the settling chamber. Therefore, Sebald et al. [38] used a single-wire hot-wire probe to measure the time-resolved velocity in the settling chamber of the AAWT. This measurement signal is then used at the inlet for a time-varying velocity boundary condition. With this method, it should be achievable to simulate the eigenmodes of the AAWT in the CFD setup. The fluctuations are only applied in the x-direction. The assumption hereby is that the fluctuations in y- and z-direction are reduced and damped by the turning vanes of the wind tunnel and the screens inside of the settling chamber, see Figure 6. Additionally, resonance effects and standing waves in the whole wind tunnel duct are the main cause of the low-frequency fluctuations in the AAWT. These standing waves are mainly acting along the duct axis and therefore the x-direction. In [38], the method of applying the experimental measured hot wire signal on the CFD domain by a time-varying inlet boundary condition shows good results for the TKE gradient. This can also be seen in Figure 46.

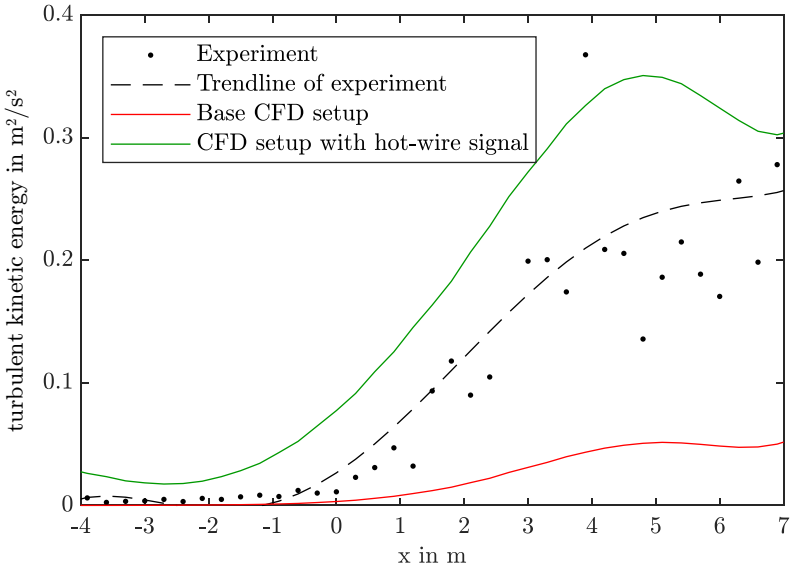

Figure 46: Turbulent kinetic energy distribution of the AAWT in y=0m and z=1.0m. With the hot-wire signal as inlet boundary condition.

In Figure 46, one can see, as in [38], that the TKE gradient of the CFD with the new boundary condition based on the hot-wire measurement has a better agreement with the experimental result as the base CFD setup. However, the TKE values are higher than the experimental TKE data. Still, it seems that adding the fluctuations measured in the wind tunnel settling chamber at the inlet of the CFD is an efficient way to enhance the time-resolved characteristics of the numerical flow compared to the experimental AAWT flow regarding the TKE

gradient. Furthermore, this method has no problems with the coarse mesh in the settling chamber area of the CFD wind tunnel and causes less computational effort compared to the synthetic turbulence method, which requires a fine mesh with an increased cell count. Because of these two advantages, Sebald et al. [38] concluded that this is a very efficient way to optimise the transient flow conditions for the simulated AAWT. Nevertheless, the TKE gradient is still not completely according to the experimental gradient of the AAWT and still needs to be optimised.

In [38], it is shown that not only for the TKE gradient, a good agreement can be found, but also for the pressure and velocity gradient. Additional to these three gradients of [38], the FFT spectrum and the shear layer gradient are evaluated in this study. Hence, the FFT spectrum at the scale centre for the CFD setup with the hot-wire signal as inlet boundary condition is given in Figure 47.

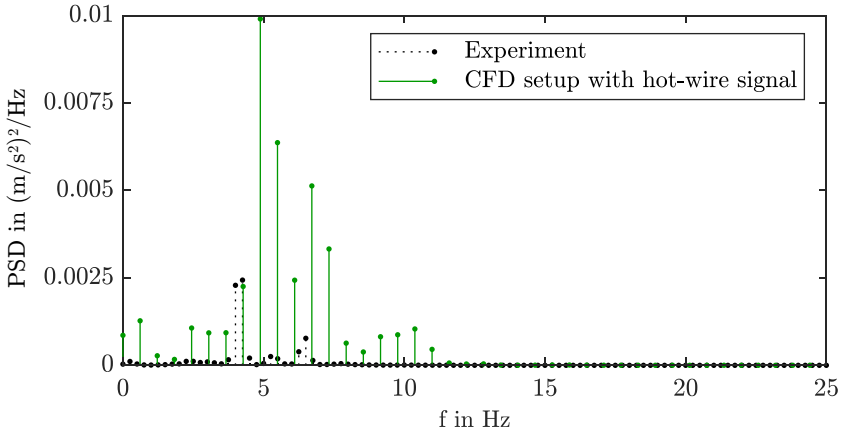

Figure 47: FFT of the flow in the AAWT at x=0m, y=0m and z=1.0m. With the hot-wire signal as inlet boundary condition.

In the FFT spectrum of Figure 47, it can be seen that the used hot-wire signal leads not only to too high TKE values but also to too high amplitudes for the main peaks of the FFT. The fluctuations resulting from the used hot-wire signal at the inlet are more intense than the fluctuations of the AAWT experiment. Therefore, the FFT amplitude and the TKE values from x=-4.0m to x=2.0m are too high. But still, the hot-wire signal enhances the frequency of the wind tunnel flow at the scale centre. Comparing the peaks of the base CFD setup FFT of Figure 42 with the FFT in Figure 47 of the hot-wire signal inlet setup, it can be seen that now the frequencies are shifted and correspond better to the experimental peaks. The peak of the AAWT experiment at 6.5Hz is also present in the CFD flow. The 4.25Hz peak of the experiment could correspond to the slightly shifted peak at around 5Hz of the simulated data. Adding the fluctuations of the settling chamber at the inlet of the CFD domain has an influence on the flow in the test section of the wind tunnel. This shows that in

contrast to the synthetic turbulence method, this method works with the coarse mesh in the settling chamber. It also shows that including the wind tunnel eigenmodes and fluctuations leads to an improvement of the time-resolved flow field characteristics. The TKE level of the CFD increases and is more in correspondence with the experimental results and the frequencies of the fluctuations in the scale centre are shifted towards the experimental peaks. In this first approach, the frequencies and their amplitudes are still not in accordance with the experiment and the method must be further optimised. But the first results indicate that it is necessary to take the wind tunnel eigenfrequencies into account to correctly predict the flow field in the CFD. The influence of this method on the time-averaged flow field characteristics is still to be investigated. Sebald et al. [38] show that for the pressure and velocity gradient in the test section, only a minor influence of the method can be seen. But the influence of this method on the shear layer needs to be evaluated. Therefore, the shear layer gradient at x=2.7m is depicted in Figure 48.

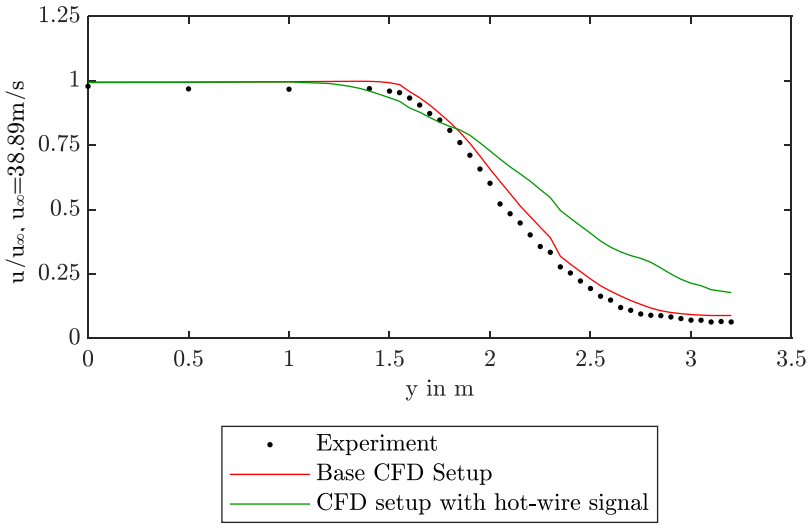

Figure 48: Shear layer gradient in the AAWT at x=2.7m in z=1.0m from y=0m to y=3.2m. With hot-wire signal as inlet boundary condition.

In Figure 48, the shear layer gradients at x=2.7m of the AAWT experiment, the base CFD setup and the CFD setup with the hot-wire signal as inlet boundary condition is depicted. As mentioned before, the shear layer gradient of the base CFD setup has, in the area from y=0m to approximately y=1.75m, a good agreement with the experiment. On the outer side, the shear layer of the base CFD setup has higher velocities than the experiment. However, the shear layer gradient of the CFD setup with the hot-wire signal has even higher velocities in the outside area from y=1.75m and an even greater deviation from the experimental shear layer gradient. For the inside of the shear layer at around

y=1.5m, the green shear layer gradient has slower velocities compared to the other gradients. Overall, the shear layer gradient for the hot-wire signal inlet is wider and the slope is less steep. This indicates that the mixing of the shear layer is greater, which leads to an expansion of the shear layer. The greater mixing could be caused by the excitation coming from the flow fluctuations of the hot-wire signal at the inlet. The fluctuations of the velocity at the inlet are causing an additional excitation at the vortex shedding of the nozzle exit on the one hand. And on the other hand, the fluctuations in the test section, in general, increase the mixing of the shear layer. The higher excitation caused by the additional fluctuations in the CFD domain can be seen in Figure 46 in the area from the nozzle exit at x=-4.0m on, where the TKE level is significantly higher compared to the base CFD setup without the added fluctuations and to the AAWT experiment. Also, the FFT spectrum at the scale centre for the CFD setup with the hot-wire signal at the inlet boundary condition has a higher amplitude of the low-frequency modes compared to the base CFD setup and experiment, which indicates that the added fluctuations are too intense. The phenomenon that additional fluctuations and excitation in the flow lead to a wider shear layer can be found in Wehrmann [16]. The fluctuations need to be reduced to solve the problem of the too-high excitation of the wind tunnel flow. This could help with the results of the TKE gradient, the FFT spectrum and the shear layer. In the first step, a lowpass Butterworth filter is applied to the hot-wire signal. In the hot-wire signal, minor high-frequency structures are included, as seen in Figure 55. For the investigation of the low-frequency wind tunnel eigenmodes, the high-frequency parts of the measurement signal can be excluded. Especially the high-frequency structures of the signal can be caused by small measurement noise or structural resonances of the hot-wire itself or the hot-wire stand. The most relevant eigenmodes of the AAWT are below 7Hz. This can be seen in the FFT spectrum in Figure 47. Therefore, the cut-off frequency of the Butterworth filter is set to 7Hz. With this filtered signal, the results depicted in Figure 49 can be derived.

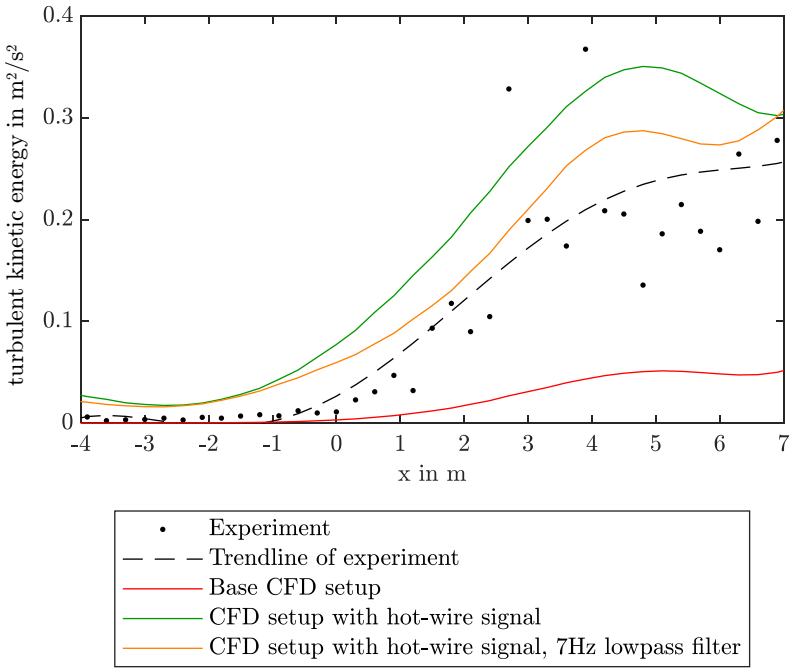

Figure 49: Turbulent kinetic energy distribution of the AAWT in y=0m and z=1.0m. With unfiltered and filtered hot-wire signal as inlet boundary condition.

In Figure 49, two different pre-processed hot-wire signals at the inlet boundary are compared. The original hot-wire signal in green and the hot-wire signal with a 7Hz Butterworth lowpass filter in orange are plotted. The TKE gradient of both hot-wire signal inlet variants have higher TKE values than the base CFD setup and have a higher agreement with the experimental data, especially in the area from x=0m onwards. The lowpass filter on the hot-wire signal affects the TKE gradient. Filtering out the higher frequency structures of the measurement signal helps to reduce the level of TKE in the empty test section from x=-1m onwards. With the filtered signal, the numerical TKE gradient agrees better with the experimental gradient. This indicates that the low-frequency modes of the measurement signal and the low-frequency eigenmodes of the wind tunnel, in general, are mostly responsible for the deviation between the experimental and numerical TKE gradient. Without the higher frequency modes of the signal, the TKE values remain at a high level. As mentioned before, the higher frequencies could cause the high excitation of the velocity fluctuations in the test section and could also cause a too-high excitation of the shear layer. The velocity fluctuations in the test section are now less overestimated by the CFD setup with the filtered hot-wire signal at the inlet. Next to the influence of the

filtered signal on the TKE gradient, its influence on the shear layer must be evaluated as well. This can be seen in Figure 50.

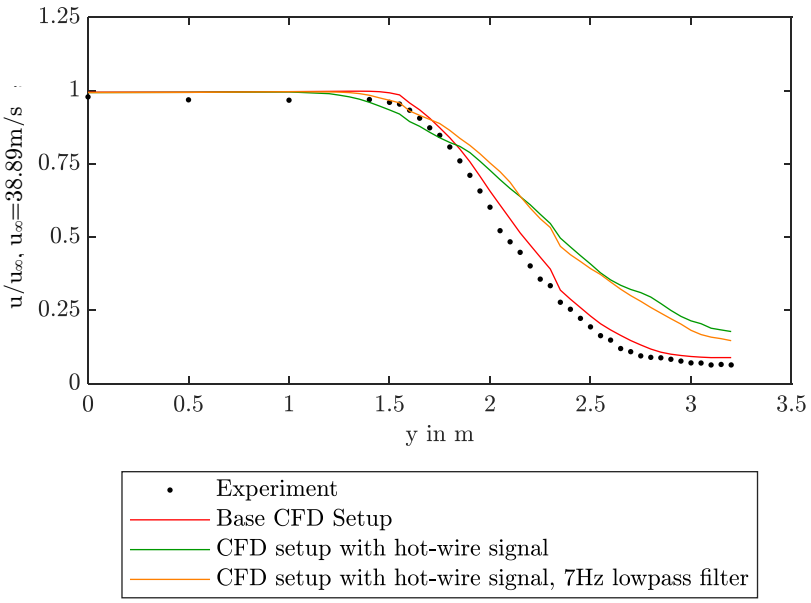

Figure 50: Shear layer gradient in the AAWT at x=2.7m in z=1.0m from y=0m to y=3.2m. With unfiltered and filtered hot-wire signal as inlet boundary condition.

In theory, the shear layer of the CFD setup with the filtered hot-wire signal should be narrower than the shear layer of the unfiltered signal. In [16], it is stated that a shear layer of an open jet becomes wider the more it is excited with additional fluctuations. This effect can also be seen for the shear layer of the AAWT between the unfiltered and filtered CFD setup in Figure 50. At the inside of the jet shear layer in the area from y=1.25m to y=2m, the shear layer of the filtered hot-wire signal setup is in better accordance with the experimental results. It is also narrower compared to the unfiltered shear layer. At the outside of the shear layer, both CFD setups with the hot-wire signal have similar velocity levels. But still, the CFD with the filtered hot-wire signal has lower velocities and is narrower than the CFD results with the unfiltered signal. This shows that without the high-frequency modes, the excitation of the shear layer is lower, and according to [16], the shear layer gets narrower. The level of fluctuations of the signal at the inlet have therefore two effects on the wind tunnel flow. The more fluctuations are at the inlet the higher are the TKE gradient values and the more the shear layer gets excited and wider. The filtering of the signal helps to get closer to the experimental gradients, but deviations remain.

Even after applying the lowpass filter with a cut-off frequency of 7Hz, the fluctuation level is still too high, which can be seen in the high TKE values and the wide shear layer. A further reduction of the fluctuations with a lowpass filter is not purposeful because reducing the cut-off frequency below 7Hz would mean that the eigenmodes of the AAWT are no longer included in the hot-wire signal. Therefore, an alternate method is used to reduce the fluctuations. From the measurement of the hot-wire, the mean value is subtracted to get only the fluctuations around the mean value. These fluctuations are then scaled to between 0.5 and 1.0 of the original fluctuation's intensity. With this method, the low-frequency eigenmodes of the AAWT remain in the signal, but their intensity can be regulated. The influence of the scaling can be seen in Figure 51.

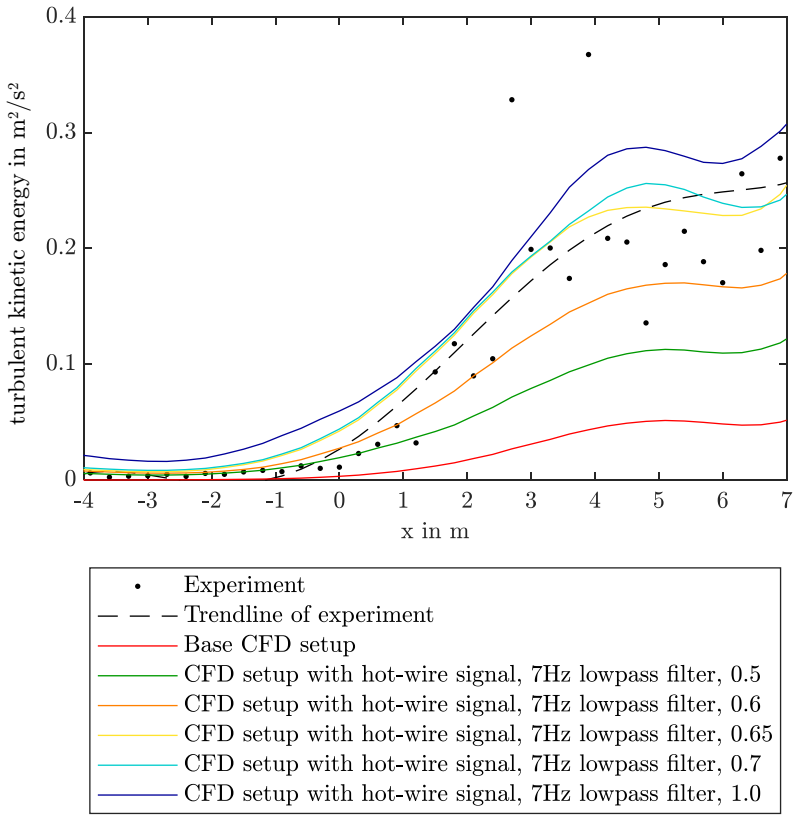

Figure 51: Turbulent kinetic energy distribution of the AAWT in y=0m and z=1.0m. With hot-wire signal as inlet boundary condition. Different intensities for the fluctuations from 0.5 to 1.0.

In Figure 51, the TKE gradients for the different scale factors of the measured fluctuations are depicted. All gradients are filtered with the 7Hz lowpass filter. The signal with 1.0 of the fluctuations has TKE values, which are higher than the experiment. Reducing the fluctuations at the inlet with scale factors results

in lower TKE in the test section. The lower the scale factor is, the lower the TKE values. Therefore, the gradient for the 0.5 scaled signal has the lowest TKE values but still greater values than the base CFD setup. The increase of the scale factor is not linear to the increase of TKE values in the test section. The gradient of the 0.5 signal is not in the centre between the TKE values of the 1.0 hot-wire setup and the base CFD setup. Also, the 0.7 signal is disproportionately higher than the 0.5 signal and close to the none scaled 1.0 version. By adapting the scale factor, a version can be derived which has good agreement with the experimental data. In this case, it is the version with a scale factor of 0.65. With this signal, the low-frequency eigenmodes of the AAWT measurements are still included in the CFD setup, while the TKE gradient has an enhanced agreement. The scaling of the fluctuations at the inlet has not only an influence on the TKE gradient but also on the time-averaged static pressure distribution. The pressure distribution for the differently scaled inlet signals is depicted in Figure 52.

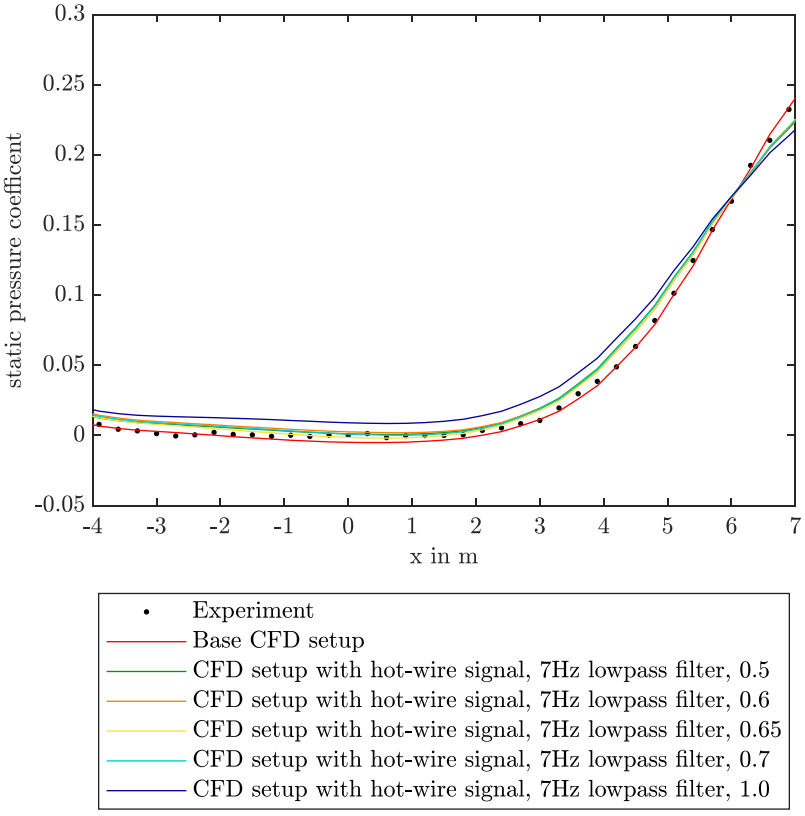

Figure 52: Static pressure distribution of the AAWT in y=0m and z=1.0m. With hot-wire signal as inlet boundary condition. Different intensities for the fluctuations from 0.5 to 1.0.

For the static pressure distribution, it can be said that the 1.0 signal has the greatest deviation from the experimental data and the base CFD setup. Therefore,

this signal cannot be used as a boundary condition for an enhanced CFD setup. The rest of the scaled signals have very similar pressure distributions and can only hardly be distinguished in Figure 52. For all scale factors between 0.5 and 0.7, the static pressure distribution matches the experimental data better than the 1.0 version, but a deviation remains between the experimental data and the base CFD setup. By reducing the fluctuations at the inlet, the pressure distribution is influenced and enhanced in the direction of the experimental data. Next to the pressure distribution, the flow field in the test section of the hot-wire CFD setup has further deviations. This can be seen by investigating the shear layer gradients for the different scale factors, which are depicted in Figure 53. It is crucial to correctly simulate the shear layer because of its impact on the whole flow field and pressure distribution in the test section. The goal is to minimize the errors of the shear layer for the hot-wire CFD setup since this setup has advantages for other flow field characteristics like the TKE gradient or the FFT.

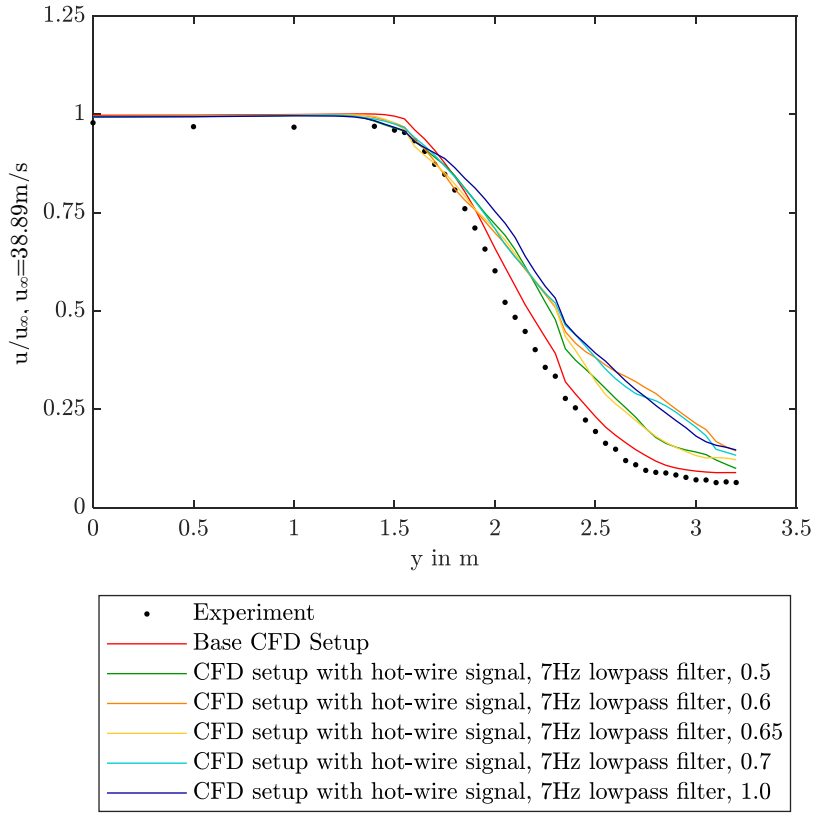

Figure 53: Shear layer gradient in the AAWT at x=2.7m in z=1.0m from y=0m to y=3.2m. With hot-wire signal as inlet boundary condition. Different intensities for the fluctuations from 0.5 to 1.0.

Like for the other gradients, the scaling of the fluctuations of the hot-wire signal has an influence on the shear layer. The signal with the 1.0 fluctuation intensity has the widest shear layer, especially in the area from y=1.5m to y=2.5m. At the outside of the shear layer at around y=3m, the signals with 0.6 and 0.7 scaled fluctuations have similar velocities to the 1.0 version. Overall, the narrowest shear layers beside the base CFD setup can be seen for the signals with 0.5 and 0.65 scale factors. Taking all the previously shown gradients into account, the hot-wire signal with the 7Hz lowpass filter and 0.65 scaled fluctuations produces the best CFD results compared to the AAWT measurements. The TKE gradient has a significantly higher agreement with the experimental data than the base CFD setup. Lastly, the temporal characteristic of the wind tunnel flow of the new CFD setup needs to be evaluated. The FFT spectrum of the AAWT experiment and the CFD setup with the hot-wire signal with a 7Hz lowpass filter and 0.65 scaled fluctuations at the inlet is shown in Figure 54.

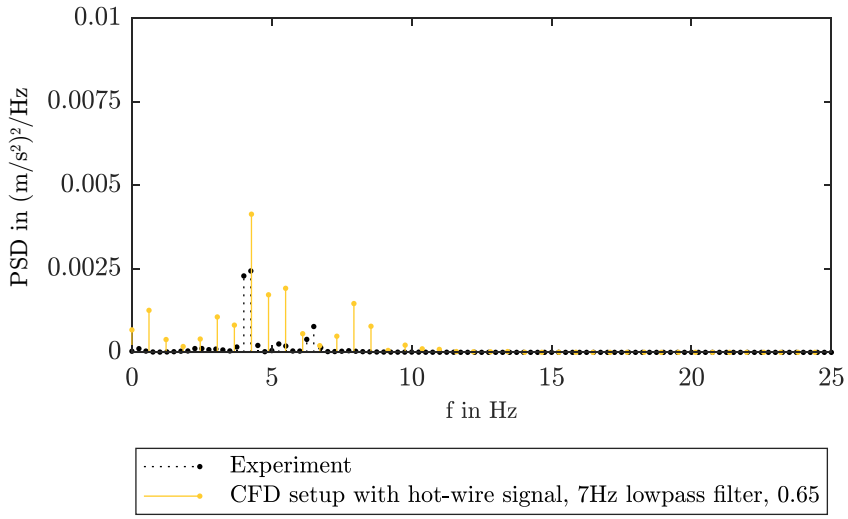

Figure 54: FFT of the flow in the AAWT at x=0m, y=0m and z=1.0m. With hot-wire signal as inlet boundary condition, 7Hz lowpass filter and fluctuation intensity of 0.65. Same scaling as in Figure 47.

The FFT spectrum in Figure 54 is plotted with the same scaling of the y axis as the FFT spectrum of Figure 47. In Figure 47, the original measured hot-wire signal is used, and in Figure 54, the filtered and 0.65 scaled hot-wire signal. Comparing these two FFT spectra shows that the lowpass filter and the scaling of the fluctuations reduce the amplitudes of the main peaks compared to the unfiltered and unscaled signal. With the reduced amplitudes of the main peaks, the CFD spectrum has a better agreement with the experimental result. Still, the amplitudes of the CFD setup remain higher compared to the experiment.

Therefore, additional filtering or scaling would be needed, but this would decrease the TKE values, as shown above. Overall, the CFD setup with the filtered and scaled hot-wire signal has the best agreement of the FFT and TKE gradient with the experimental data so far. Nevertheless, the static pressure distribution and the shear layer have increased deviations from the experimental measurements compared to the base CFD setup. The deviations for the time-averaged gradients, like pressure distribution and shear layers, need to be addressed in the following investigation.

So far, the method of using the experimental hot-wire data at the inlet boundary condition leads to the following conclusion. Adding fluctuations of the AAWT experiment, which are caused by the eigenmodes and resonance phenomena of the AAWT, widens the shear layer and leads to a deviating static pressure distribution. For the time-resolved flow field, it is beneficial to include the measured eigenmodes of the AAWT, but this concludes in too high TKE values and FFT amplitudes for the raw signal of the hot-wire. All these problems could be reduced by filtering the measurement signal and scaling the fluctuations down. Another problem with this method is, however, that the measurement signal must be prepared for the simulation. Especially the used time of the measurement signal must be adapted to the simulation time. This means that different parts from the hot-wire signal are used for different simulation durations. Additionally, the used hot-wire signal at the inlet is manipulated a lot with the lowpass filter and the scaled fluctuations. The characteristics that it has in common with the original signal are the temporal structures of the flow, hence the main peaks of the FFT spectrum.

To get a more generic method which can be applied to different simulations, the hot-wire signal cannot be used for further simulations. Instead, sine waves are used to include the eigenmodes of the AAWT in the CFD setup. This has the advantage that the fluctuations are present in the simulation and therefore, the time-resolved flow field characteristics are predicted correctly by the CFD. While for different simulation durations, no adaption of the input data is necessary. Analysing the temporal structures of the hot-wire signal in the settling chamber reveals five low-frequency main peaks, these are depicted in Figure 55. In Figure 55, the FFT spectrum of the AAWT flow in the settling chamber is depicted. This FFT spectrum is from the hot-wire measurement used for the hot-wire CFD setups. With the new generic method, the temporal structures of this signal need to be modelled with sine waves. The previous investigation has shown that the noise of the measurement and other small structures of the hot-wire measurement are causing deviations in the flow field because these structures excite the shear layer too much. The solution was to filter and scale the disturbing structures to get a better result. With the method of generic sine waves, this problem is also solved because only the important low-frequency eigenmodes of the AAWT will be modelled and the measurement noise will completely disappear.

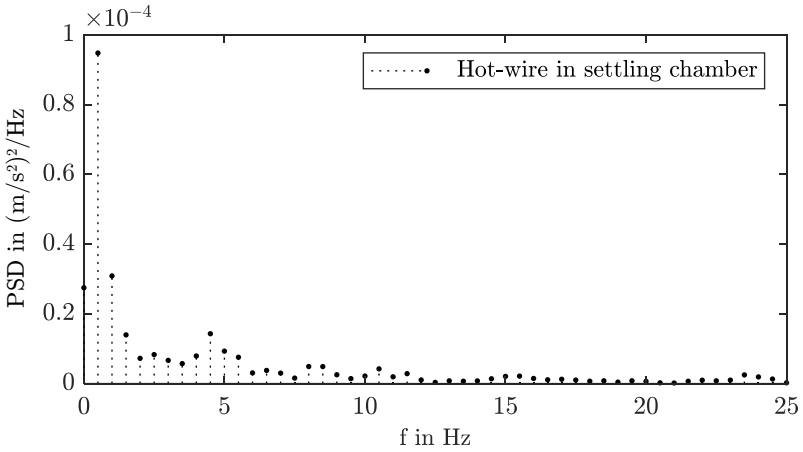

Figure 55: FFT of the flow in the settling chamber of the AAWT. Hot-wire measurement in y=0m, x=1.0m behind the turbulence screens and z=1.0m above the floor.

The most important information for adding the AAWT eigenmodes in the CFD setup is the frequency of the eigenmodes. The investigation has shown that the best results could be reached by using a 7Hz lowpass filter on the hot-wire signal and that the TKE gradient and the FFT results remain good. Therefore, for the generic modelling of the AAWT eigenmodes, only the low-frequency peaks of the hot-wire signal will be used. Looking at Figure 55, the following peak frequencies can be determined. Under 7Hz, four peaks at 0.5Hz, 2.5Hz, 4.5Hz and 6.5Hz can be seen. According to the previous results, these peaks could be enough to represent the AAWT eigenmodes in the simulation. Additional peaks at 5.25Hz, 8.0Hz and 10.5Hz are present in the FFT spectrum. Their influence on the flow field is also investigated since these peaks are also dominant in the FFT spectrum. Looking at the FFT spectrum at the scale centre of the experimental data in Figure 42, there is a dominant peak at 5.25Hz and hardly any peak at 8.0Hz or 10.5Hz. Especially the 5.25Hz peak is at scale centre in relation to the other peaks higher than in the settling chamber, see Figure 55. The flow structure related to the 5.25Hz peak seems to be present in the test section with higher amplitude than in the rest of the wind tunnel. For the first steps of optimisation, only the frequencies at 0.5Hz, 2.5Hz, 4.5Hz and 6.5Hz are used. The peaks at 8.0Hz and 10.5Hz have a minor influence on the test section flow on their own. They have very small amplitudes in the FFT of the test section flow and have only a small influence on the temporal characteristic of the flow field. Nevertheless, the 10.5Hz is used with very little amplitudes for all different variants with a constant amplitude of 0.001 and a phase shift of 0.0°. In the early phase of the optimisation, this has proven to be an efficient solution for the inlet boundary. In the final phase of the optimisation, the influence of the 5.25Hz modes is investigated.

Next to the frequency of the eigenmodes, the phase shift and the amplitude of the sine wave are also very important for the behaviour of the flow field. In a first approximation, the amplitude for the respective sine wave is derived from the amplitude of the FFT spectrum. The phase shift is set to 0° for all sine waves for the first step. The exact amplitudes and phase shifts will be optimised later based on the gradients and FFT spectrum in the empty test section of the AAWT. In Figure 56, the first result of the CFD setup with sine waves is depicted.

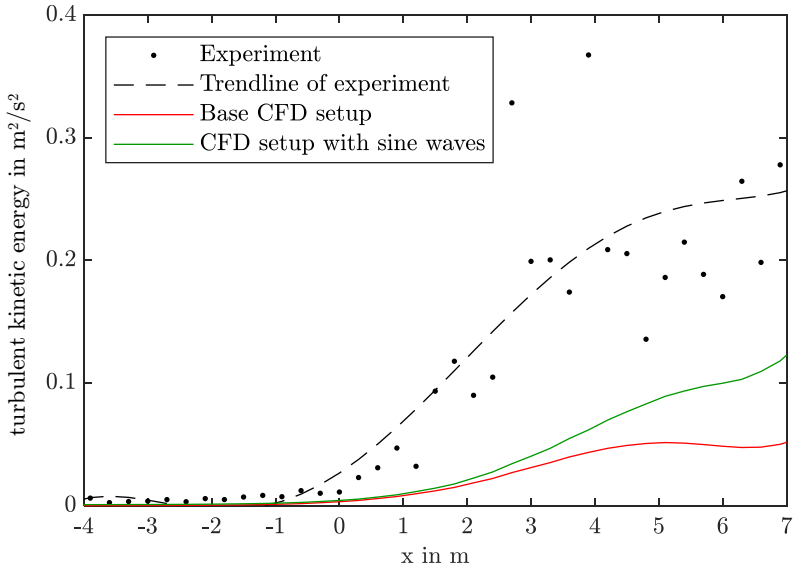

Figure 56: Turbulent kinetic energy distribution of the AAWT in y=0m and z=1.0m. With generic sine waves at the inlet of the CFD domain. Amplitudes approximated based on the FFT of the settling chamber measurement signal.

In Figure 56, the TKE gradient for the base CFD setup and a first approximation with generic sine waves is depicted. Adding the sine waves at the inlet of the CFD domain helps to increase the TKE values in the test section of the AAWT. The TKE values are higher compared to the base CFD setup, but they are still lower than the experimental data. Four sine waves with a specific frequency, which is derived from the FFT spectrum of the hot-wire measurement in the settling chamber, are used. Each sine wave has a specific amplitude. The phase shift of the sine waves is set to 0°. The used amplitudes can be seen in Table 5.

Table 5: Frequency and amplitude for the sine waves at the inlet.

Frequency	**0.5Hz**	**2.5Hz**	**4.25Hz**	**6.5Hz**
Amplitude	0.01	0.001	0.002	0.0005

With these amplitudes, an improvement of the TKE gradient can be seen, but an increase in amplitude could be needed to further increase the TKE values in the test section. In Figure 57, the FFT spectrum of the CFD setup with sine waves based on the AAWT eigenfrequencies has a slightly higher agreement with the experimental data than the base CFD setup. For the FFT spectrum, too, the amplitudes of the peaks are too low to match the experimental data. An increase in the sine wave amplitudes could be helpful to get a better agreement. Still, the sine waves with the AAWT eigenfrequencies enhance the frequency of the FFT peaks. With the sine waves, the FFT peaks are now more like the peaks of the experimental data and are no longer shifted, like in the base CFD setup. This effect should be more visible for the FFT spectrum with higher amplitudes for the sine waves.

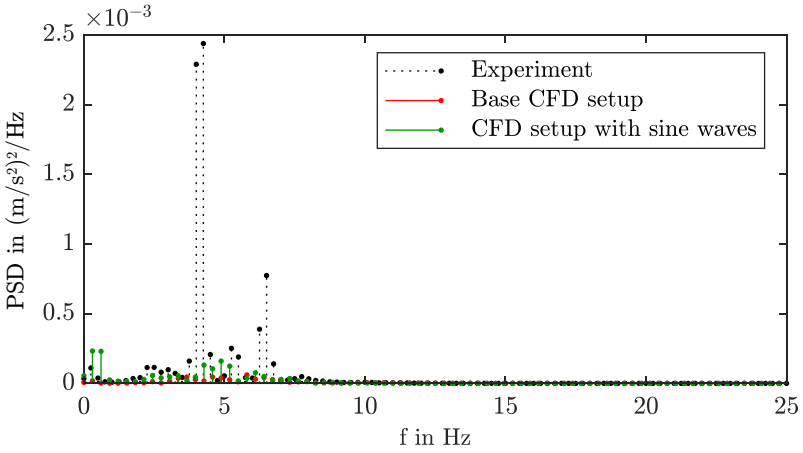

Figure 57: FFT of the flow in the AAWT at x=0m, y=0m and z=1.0m. With the first approximation of sine waves at the inlet.

In Figure 58, the influence of the sine waves at the inlet boundary condition on the shear layer can be seen. The shear layer of the CFD setup with sine waves has a higher agreement with the experimental shear layer compared to the base CFD setup. In chapter 1.2, it is shown that the eigenfrequencies of a wind tunnel have a huge influence on the shear layer and vice versa. So, it seems plausible that the shear layer is predicted with higher accuracy when the wind tunnel eigenmodes are present in the CFD setup as well. A more detailed look at the shear layer will be given at the end of the CFD optimisation when the amplitudes and phase shifts are correctly set.

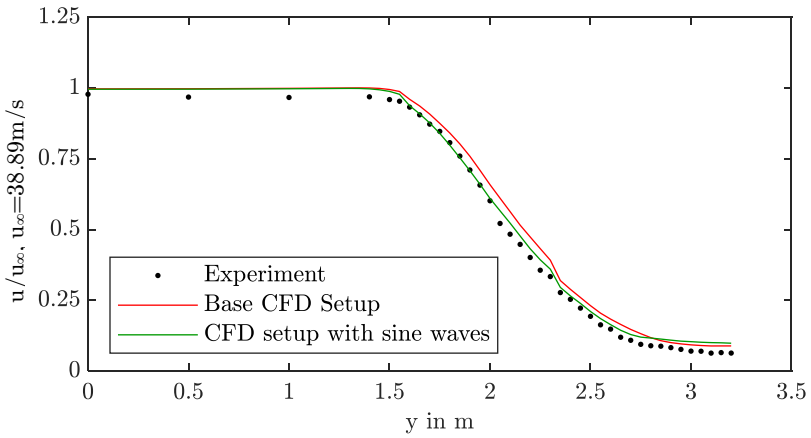

Figure 58: Shear layer gradient in the AAWT at x=2.7m in z=1.0m from y=0m to y=3.2m. With the first approximation of sine waves at the inlet.

The first results show that using a generic inlet method with sine waves leads in the right direction, but the amplitudes need to be adjusted. For the next step, various amplitudes are tested to find the result that best corresponds with the experimental data. The investigated amplitudes are shown in Table 6.

Table 6: Frequency and amplitude for the sine waves at the inlet. Four variations of the amplitudes.

Frequency	**0.5Hz**	**2.5Hz**	**4.25Hz**	**6.5Hz**
Amplitude 1	0.01	0.001	0.00200	0.0005
Amplitude 2	0.03	0.020	0.04000	0.0200
Amplitude 3	0.05	0.002	0.00500	0.0020
Amplitude 4	0.01	0.005	0.01025	0.0065

The amplitudes are set to generate different TKE gradients from very high amplitudes, like version 2, to the base amplitudes of version 1. This helps to find the amplitudes, which are necessary to correctly simulate the test section flow of the AAWT. The results are depicted in Figure 59.

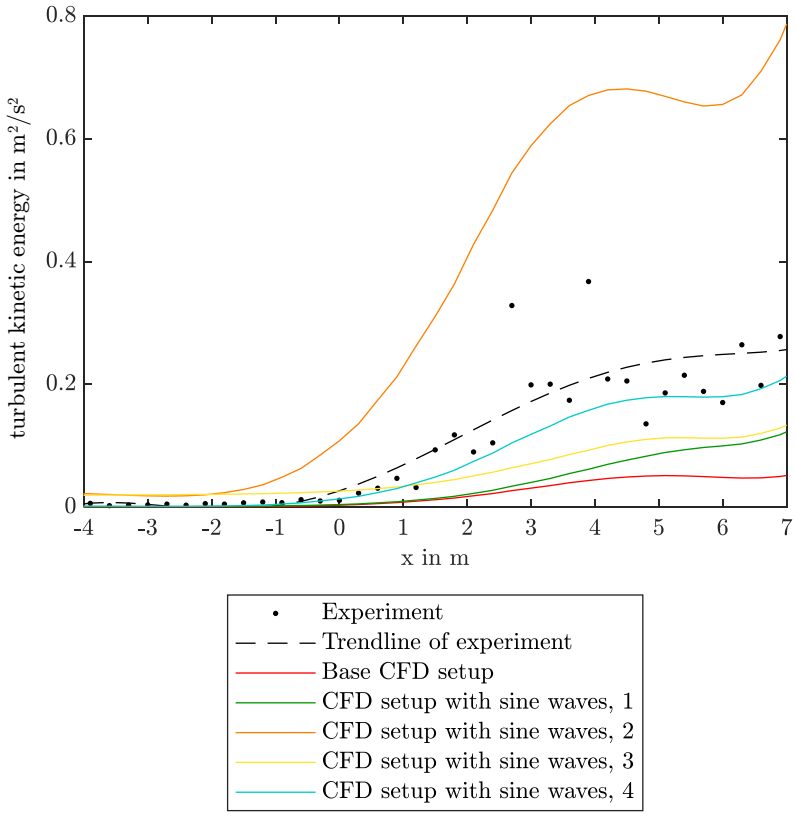

Figure 59: Turbulent kinetic energy distribution of the AAWT in y=0m and z=1.0m. With generic sine waves at the inlet of the CFD domain. Four versions of different amplitudes according to Table 6.

In Figure 59, the influence of different amplitudes on the TKE gradient is depicted. The orange gradient of version 2 shows the highest TKE values and has the highest amplitudes of the sine waves at the inlet. For versions 2 and 3, high TKE values in the area from x=-4.0m to x=0m can be seen. These values are not only higher than the other CFD versions but also higher than the experimental data. Comparing the amplitudes of the respective frequencies, the decisive difference for versions 2 and 3 is the amplitude of the 0.5Hz sine wave. It seems that in the front half of the test section, where the shear layer and its influence on the free stream of the jet is still small, the low-frequency fluctuation of the 0.5Hz sine wave generates a high level of fluctuation. The remaining amplitudes of versions 2 and 3 are partially lower and higher compared to the other versions, so the 0.5Hz sine wave is responsible for the high TKE values in the front part of the test section. Now looking at the remaining sine waves, the following conclusions can be drawn. Version 1 has overall the smallest amplitudes and therefore the smallest TKE values. In accordance, version 2 has, apart from

the 0.5Hz sine wave amplitude, the highest amplitudes and therefore the highest TKE values. Version 3 has a much higher amplitude for the 0.5Hz sine wave than version 4 and therefore higher TKE values in the front part compared to version 4. In the back part of the test section, version 4 has higher TKE values. This can be explained by the higher amplitudes of the 2.5Hz, 4.25Hz and 6.5Hz sine waves. It seems that these sine waves are more important for the TKE values in the back part of the test section. This assumption can also be seen by comparing versions 2 and 3. Both versions have high amplitudes for the 0.5Hz and therefore, in the front part, high TKE values. In the back part, version 2 has much higher TKE values and much higher amplitudes for the 2.5Hz, 4.25Hz and 6.5Hz sine waves. Summarized, it can be said that the 0.5Hz eigenmode generates a basis fluctuation level straight from the nozzle exit and the 2.4Hz, 4.25Hz and 6.5Hz sine waves, which are more linked to shear layer phenomena, have a bigger influence on the TKE level more downstream where the shear layer is already well developed.

Comparing the shear layers of the different versions reveals an expected behaviour. The shear layer gradients of the different versions are depicted in Figure 60.

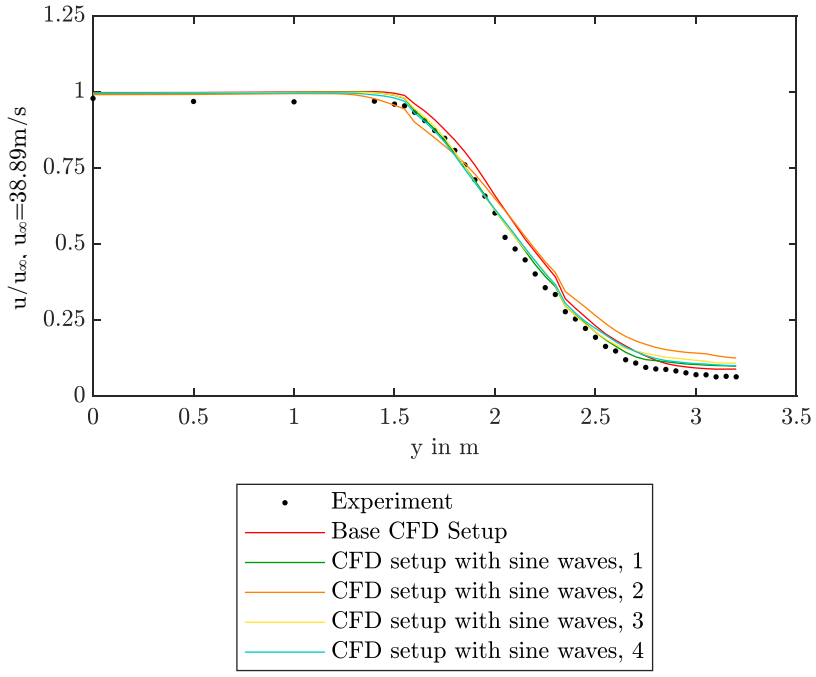

Figure 60: Shear layer gradient in the AAWT at x=2.7m in z=1.0m from y=0m to y=3.2m. With generic sine waves at the inlet of the CFD domain. Four versions of different amplitudes according to Table 6.

In Figure 60, it can be seen that the shear layer of version 2, which has the highest sine wave amplitudes and TKE levels, also has the widest shear layer. At the inside part of the shear layer, the orange gradient of version 2 starts with the decline of the time-averaged velocity first and has at the outside part of the shear layer also the highest velocities, therefore the widest shear layer of them all. This is in accordance with the findings of Wehrmann [16], where the shear layer of an excited jet is wider than that of a jet without excitation. In Figure 60, the version with the highest sine wave amplitudes at the inlet and therefore the version with the highest additional excitation of the flow has the widest shear layer. The other three versions, 1, 3 and 4, are very similar and with a higher agreement with the experimental shear layer than the base CFD setup. Nevertheless, small differences can be found for the shear layers. Version 1 has the narrowest shear layer, followed by version 3 and, lastly, version 4. Hence, for these three versions, the version with the lowest TKE levels has the narrowest shear layer and the version with the highest TKE values has the widest shear layer. Again, the hypothesis of Wehrmann [16] can be supported by the results of this investigation. The version with the highest agreement with the experimental data is chosen to investigate the influence of the sine wave amplitudes on the FFT spectrum. The highest agreement has version 4 and its FFT is depicted in Figure 61.

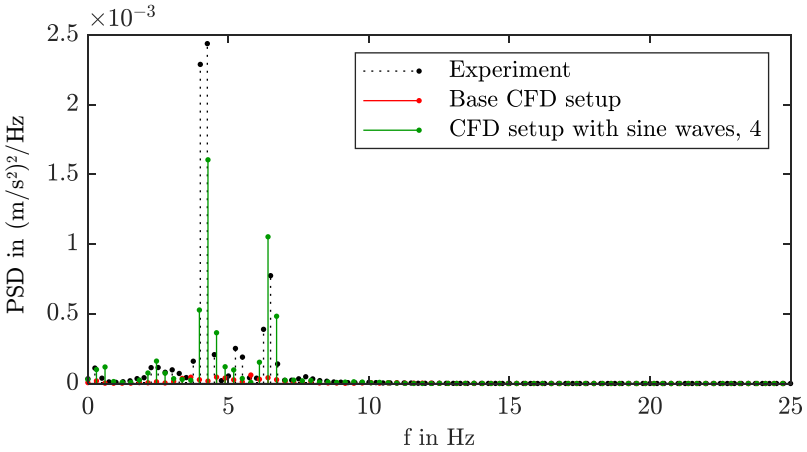

Figure 61: FFT of the flow in the AAWT at x=0m, y=0m and z=1.0m. With generic sine waves at the inlet of the CFD domain. Version 4 with amplitudes according to Table 6.

In Figure 61, the FFT spectrum at the scale centre for the experimental data, the base CFD setup and the sine wave version 4 are depicted. A huge improvement in the amplitude of the FFT peaks compared to the base CFD setup in Figure 42 or version 1 in Figure 57 can be seen. The amplitudes of the sine wave at the inlet of the CFD domain have a huge influence on the amplitudes of the FFT peaks in the scale centre of the AAWT. The CFD version 4 with the sine waves has a higher agreement with the experiment than the base CFD setup.

Overall, the amplitudes of the sine wave at the inlet influence the TKE values in the test section, the width of the shear layer and the FFT spectrum in the scale centre. The remaining parameter which needs to be investigated is the phase shift for the specific sine waves. In Table 7, various versions with different phase shifts are given, which will be investigated in the following. The amplitudes are derived from version 4, which so far has the highest agreement with the experimental data. The influence of the phase shift can be seen in Figure 62.

Table 7: Frequency and phase shift for the sine waves at the inlet. Four variations of the phase shifts based on the amplitudes of version 4.

Frequency	**0.5Hz**	**2.5Hz**	**4.25Hz**	**6.5Hz**
Phase 4	0.0°	0.0°	0.0°	0.0°
Phase 5	180.0°	90.0°	90.0°	180.0°
Phase 6	180.0°	90.0°	180.0°	180.0°
Phase 7	180.0°	90.0°	0.0°	180.0°

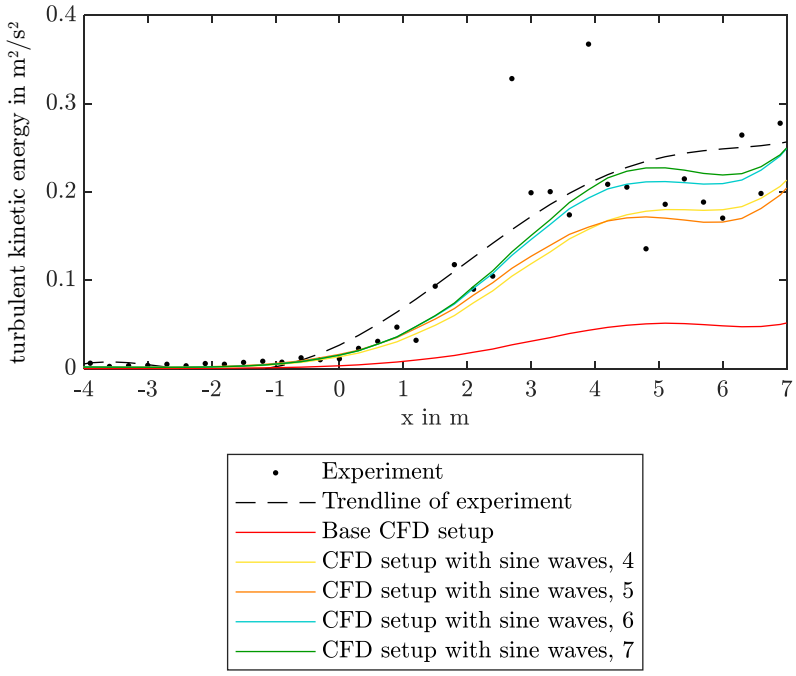

Figure 62: Turbulent kinetic energy distribution of the AAWT in y=0m and z=1.0m. With generic sine waves at the inlet of the CFD domain. Four versions of different phase shifts according to Table 7.

The phase 4 configuration has the same parameters as version 4 of the amplitude investigation. In phase 5, also seen as version 5, phase shifts of 90.0° and 180.0° are added to the sine waves, according to Table 7. In Figure 62, only a small influence of the added phase shifts on the TKE gradient for versions 4 and 5 can be seen. A bigger influence can be seen for versions 6 and 7. The difference between these versions is the phase shift of the 4.25Hz sine wave. As for the amplitude, the phase shift of the strongest eigenmode of the AAWT with the highest amplitude has the greatest influence on the TKE gradient. The two versions 6 and 7, where the 4.25Hz sine wave has a phase shift of 0.0° and 180.0°, have higher TKE values in the back part of the test section compared to version 5 with 90.0°. An obvious explanation for this phenomenon cannot be stated. It could be caused by the fact that the 90.0° phase shift "disturbs" the shear layer vortex shedding at the nozzle exit and the shear layer evolution in general and therefore the fluctuations of the test section being less excited, which results in lower TKE values. Version 7 has the highest TKE values with a 0.0° phase shift. According to the aforementioned assumption, the 4.25Hz sine wave with 0.0° phase shift "disturbs" the shear layer evolution the least, which results in the highest TKE values.

Also, looking at the shear layer gradients in Figure 63, only small differences between the different versions of phase shifts can be seen. Especially at the inside of the shear layer, which is the most important part of the flow characteristics of the wind tunnel jet, no differences can be seen. On the outside versions 4 and 7 have the best agreement with the experimental shear layer. Combining this result with the result of the TKE gradient in Figure 62, version 7 has the best agreement with the experimental data.

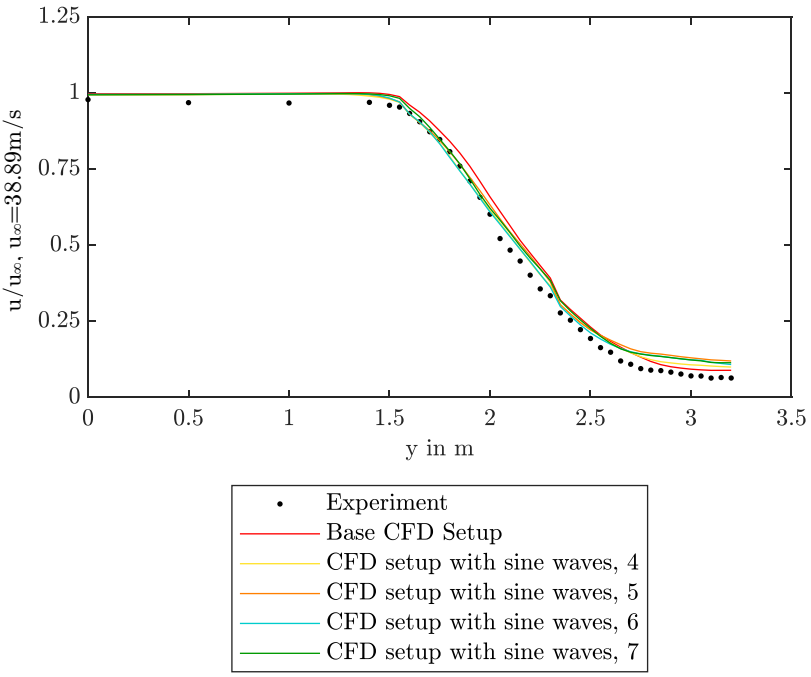

Figure 63: Shear layer gradient in the AAWT at x=2.7m in z=1.0m from y=0m to y=3.2m. With generic sine waves at the inlet of the CFD domain. Four versions of different phase shifts according to Table 7.

Overall, the influence of the amplitude of the sine waves at the inlet of the CFD domain is greater than the influence of the phase shift. The phase shift influence needs to be investigated in further detail. But for now, version 7 is a huge improvement for all flow field characteristics compared to the base CFD setup. In Figure 64, the FFT spectrum of version 7 is depicted.

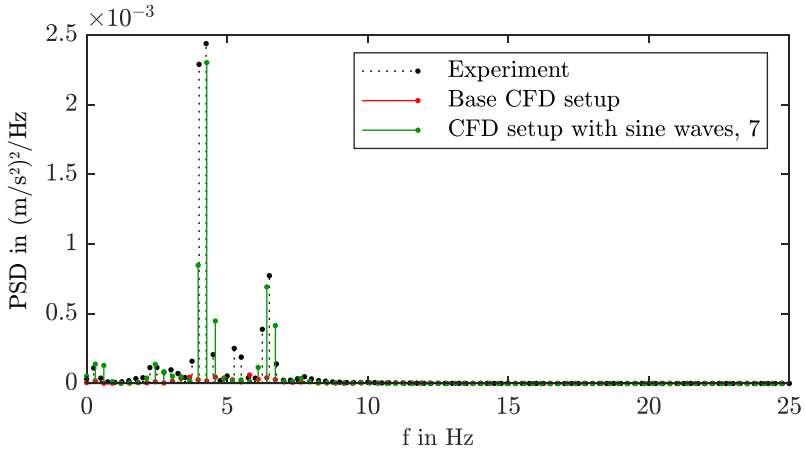

Figure 64: FFT of the flow in the AAWT at x=0m, y=0m and z=1.0m. With generic sine waves at the inlet of the CFD domain. Version 7 with amplitudes according to Table 7.

In the FFT spectrum of version 7 in Figure 64, a better agreement with the experimental data compared to the base CFD setup can be seen. The frequencies and amplitudes of the peaks match the experimental data well. Only the peak at around 5.25Hz is not present in version 7. This is caused by the missing 5.25Hz sine wave at the inlet of the CFD domain. In the last optimisation step, a sine wave with a frequency of 5.25Hz is added at the inlet boundary. The results for this last step can be seen in Figure 65 for version 8.

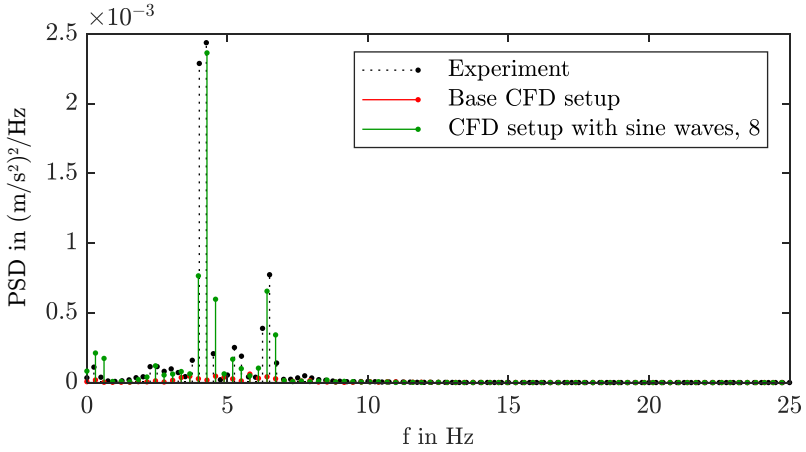

Figure 65: FFT of the flow in the AAWT at x=0m, y=0m and z=1.0m. With generic sine waves at the inlet of the CFD domain. Version 8, based on version 7 with amplitudes according to Table 6 and added 5.25Hz sine wave.

With the added 5.25Hz sine wave at the inlet, the FFT spectrum at the scale centre also shows a peak at 5.25Hz in accordance with the experimental data. Now all major peaks of the experiment are present in the CFD flow and therefore

the time-resolved flow characteristics have a better agreement with the optimised inlet boundary condition compared to the base CFD setup. This also shows that this method is very efficient at adapting to new flow characteristics. By simply adding another sine wave at the inlet, the flow in the test section can be optimised to the experimental flow. For other wind tunnels with different eigenfrequencies, this method can be used as well and only the sine wave parameters have to be adapted. For now, version 8 will be considered the best approximation of the CFD flow to the experimental wind tunnel flow in terms of the FFT result. As a last step, the remaining gradients will be evaluated to get the overall quality of the CFD flow of version 8. These gradients are depicted in Figure 66, Figure 67, Figure 68, Figure 69, Figure 70 and Figure 71.

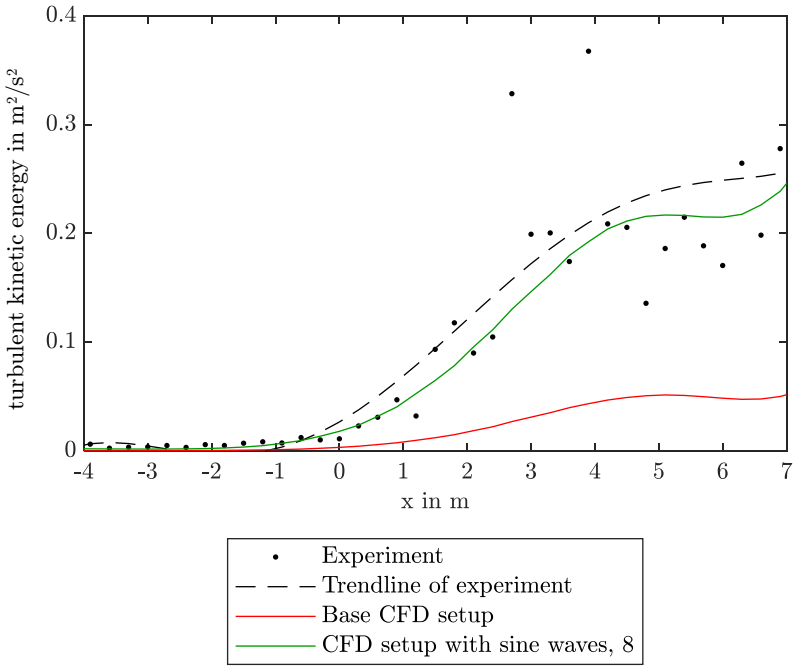

Figure 66: Turbulent kinetic energy distribution of the AAWT in y=0m and z=1.0m. With generic sine waves at the inlet of the CFD domain, version 8.

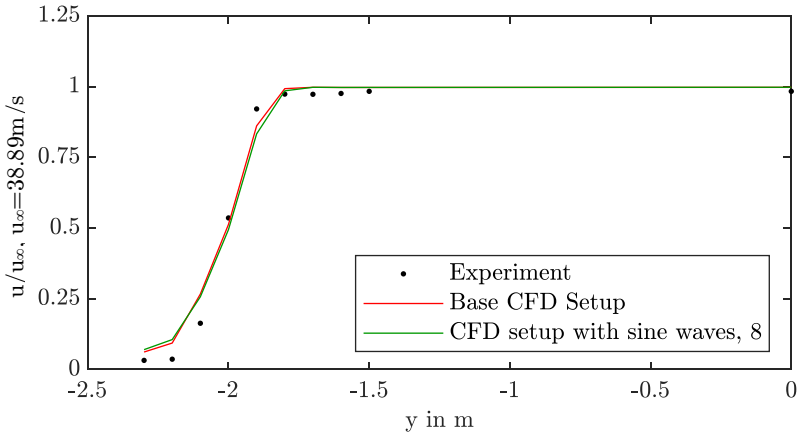

Figure 67: Shear layer gradient in the AAWT at x=-2.5m in z=1.0m from y=-2.3m to y=0m. With generic sine waves at the inlet of the CFD domain, version 8.

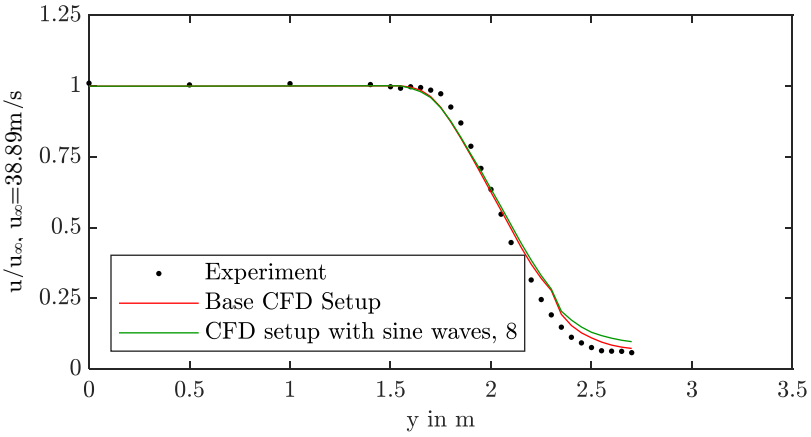

Figure 68: Shear layer gradient in the AAWT at x=0m in z=1.0m from y=0m to y=2.7m. With generic sine waves at the inlet of the CFD domain, version 8.

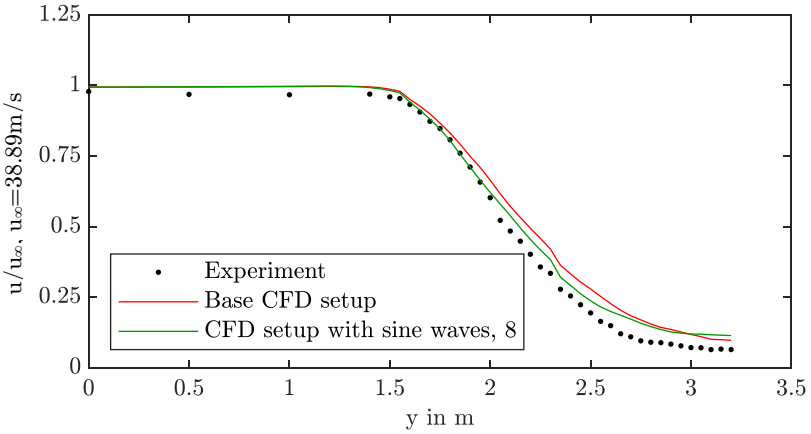

Figure 69: Shear layer gradient in the AAWT at x=2.7m in z=1.0m from y=0m to y=3.2m. With generic sine waves at the inlet of the CFD domain, version 8.

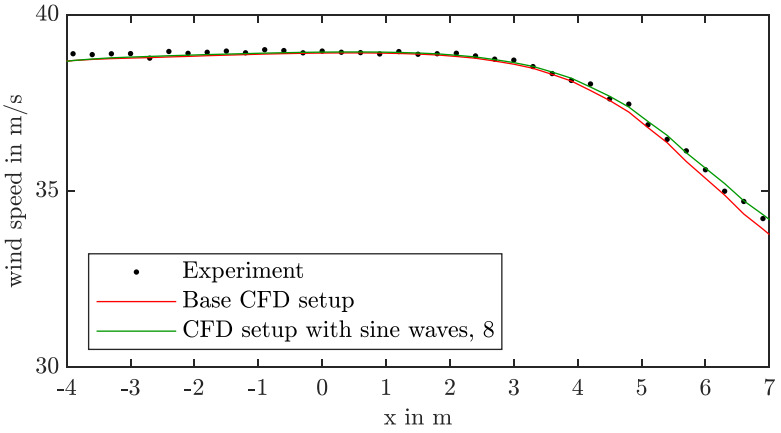

Figure 70: Wind speed in the test section of the AAWT in y=0m and z=1.0m. With generic sine waves at the inlet of the CFD domain, version 8.

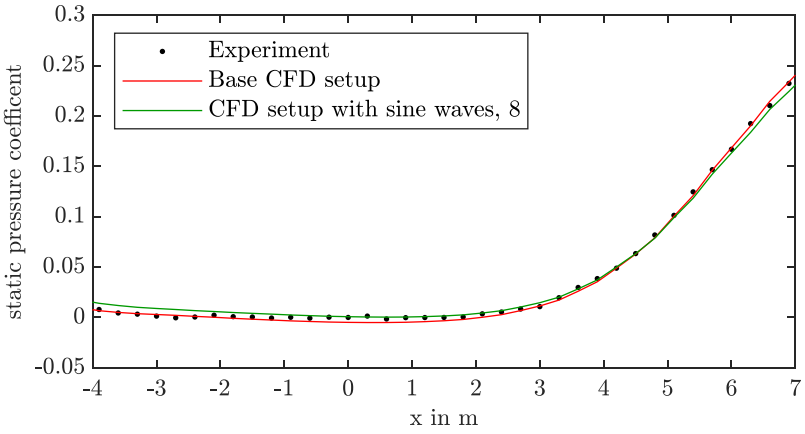

Figure 71: Pressure distribution of the AAWT in y=0m and z=1.0m. With generic sine waves at the inlet of the CFD domain, version 8.

In Figure 66, it can be seen that the TKE gradient for the CFD setup version 8, with the new inlet boundary condition, has a higher match with the experimental data points and trendline than the base CFD setup. From the nozzle to the collector of the AAWT, a very good agreement between the CFD setup version 8 and the experimental data can be seen. The shear layer gradients of Figure 67 and Figure 68 are very similar to the base CFD setup. Only at the outside of the shear layer, the optimised CFD setup has slightly higher velocities. The shear layer gradient of the optimised CFD setup in Figure 69 has a better agreement with the experimental result compared to the base CFD setup. Nevertheless, a deviation from the experimental gradient for the region from y=2.0m to y=3.2m remains. In this region, both CFD gradients deviate from the experiment, but the optimised CFD shows less deviation. Only for the area from y=3.0m to y=3.2m, the base CFD setup has slightly better matching values compared to the optimised setup. Taking into account that the shear layer gradients of the optimised CFD setup match the experimental data at the inside of the shear layer better than the base CFD setup, it still can be seen as an improvement. This is due to the importance of the inside of the shear layer for the flow condition at the vehicle in the test section of the wind tunnel. An improvement of the CFD flow can also be seen in Figure 70, where the wind speed in the test section at y=0m matches the experimental wind speeds better than the base CFD setup. The pressure gradient in Figure 71 shows mixed results. For the area from approx. x=-2.0m to x=7.0m, the pressure gradient of the optimised CFD setup matches the experimental data as well as the base CFD setup. Only for the area right after the nozzle exit, the optimised CFD setup has higher pressure values than the experimental pressure gradient. The pressure values in the area where the vehicle is positioned in the test section from x=-2.5m to x=2.5m and beyond have a good agreement with the experimental data.

The optimised CFD setup of version 8 can be considered an overall suitable solution to correctly predict the time-averaged and -resolved flow field of the AAWT.

The static pressure coefficient right after the nozzle exit and the outside of the shear layer gradient remains the only small deviations of the optimised CFD setup version 8 from the experimental data. Especially for the time-resolved flow field, the optimised CFD setup has great improvements. For the TKE gradient and the FFT spectrum in the AAWT, huge improvements can be derived from the new inlet boundary condition. Deviations which are present in the base CFD setup can be strongly reduced and a better correspondence to the experimental wind tunnel flow can be achieved. Additionally, the time-averaged characteristics like the shear layer gradient or the wind speed distribution in the test section at y=0m are also improved by the optimised CFD setup.

With all the improvements in the CFD wind tunnel flow, the CFD setup version 8 is now used to simulate the flow around a vehicle. With the new CFD setup, results with a better agreement with the wind tunnel results could be expected. Also, the influence of the wind tunnel eigenfrequencies on the flow field around the vehicle can be investigated by comparing the base CFD setup results with the results derived from the optimised CFD setup. This helps to get an insight into the importance of representing the wind tunnel eigenmodes in the CFD and how they influence the vehicle flow. That representing the wind tunnel eigenfrequencies in the CFD is important can be seen by looking at the previous figures and how good the agreement of the CFD gradients and spectra is for the CFD setups with the wind tunnel eigenmodes.

4 Consequences for the Numerical Vehicle Aerodynamics

In the following chapter, the influence of the new optimised CFD setup on the flow field around a vehicle will be investigated. The new CFD setup shows good results and a better agreement between the numerical and experimental results of the empty test section. It is assumed that this tendency can also be seen in the aerodynamic results and flow field characteristics of a vehicle. Therefore, integrated forces, the time-averaged and time-resolved flow field of a vehicle, will be used to analyse the quality of the new CFD setup. Furthermore, the influence of the wind tunnel eigenmodes, which are newly introduced into the CFD domain by the optimised CFD setup, on the flow field around the vehicle will be investigated.

4.1 Vehicle Simulation Setup

The simulations of the vehicle are carried out in two different CFD domains. The Box CFD setup is the simulation in a big box, as described in chapter 2.3. This ensures that no wind tunnel interference effects are present in this CFD setup. Therefore, the results of this setup are seen as ideal CFD results. These ideal CFD results will be compared to the numerical results with a wind tunnel geometry. The setup with wind tunnel geometry uses the partial model of the AAWT, see Figure 37 and chapter 2.2.2, which is used in chapter 3.2 for the empty test section simulations. In this CFD setup, the basic time-averaged wind tunnel interference effects of the AAWT are represented and their influence on the flow field of the vehicle can be evaluated. More detailed information about the CFD setups can be found in Table 3.

The DrivAer model from chapter 2.1.2 will be used for the following investigation. To correctly represent the vehicle geometry of the wind tunnel tests in the CFD, 3D laser scans are made to ensure that the CAD data is in accordance with the physical DrivAer model. For the investigation, the model is used with and without tires. Both configurations are modelled to correspond to the physical vehicle of Figure 7 and Figure 8. The CAD model of the vehicle without wheels is depicted in Figure 72 and the model with wheels is depicted in Figure 73. The wheels are causing a disturbance in the flow and more vortical structures arising from the wheels are present in the flow. This makes it harder to distinguish dominant vortical structures. Hence, the vehicle without wheels is used to get first insights into the simplified transient flow field and then the vehicle with wheels is used to evaluate if the findings can be transferred to a realistic vehicle setup with wheels.

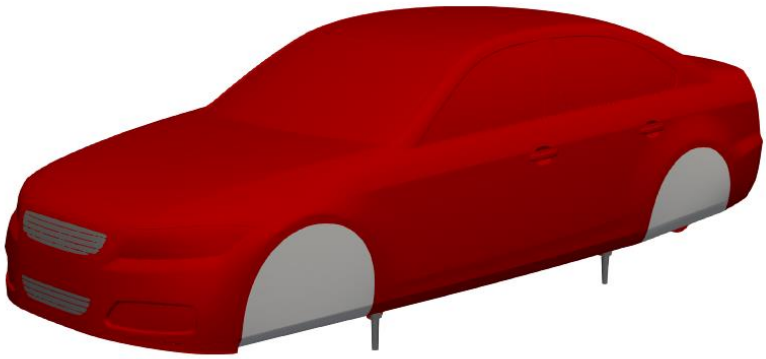

Figure 72: CFD model of the DrivAer without wheels and closed wheel arches.

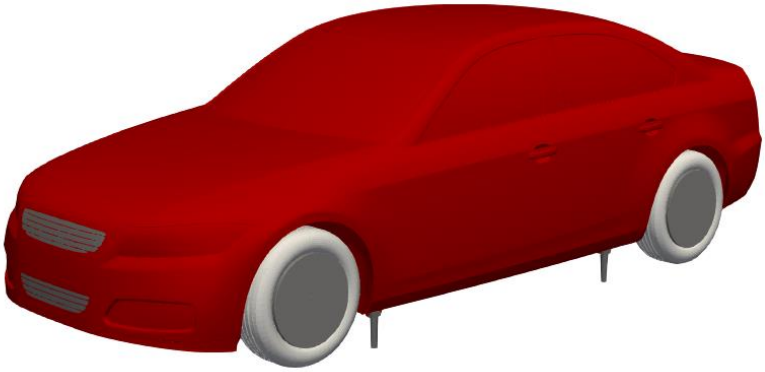

Figure 73: CFD model of the DrivAer with aluminum wheels and closed rims.

In the Box CFD setup, the DrivAer model is positioned in the middle of the box with a static ground. With the inlet area of A_I=2160m^2 and the frontal area of the DrivAer of A_F=2.12m^2, the blockage ratio of the Box CFD setup is at 0.1%. The refinement regions of the Box CFD setup are only around the vehicle. These regions are identical to the vehicle refinement regions in the AAWT CFD setup and will be described there.

With the nozzle outlet cross-section of the AAWT of A_N=11m^2 the blockage ratio for the AAWT CFD setup is 19%. In Figure 74, the side view of the partial model of the AAWT with the DrivAer model positioned in the test section can be seen together with the velocity distribution at y=0m. It is the same wind tunnel geometry with the same refinement regions for the shear layer as described in chapter 3.2.1 for the empty test section investigation. Also, the boundary conditions are equal to the empty test section setup.

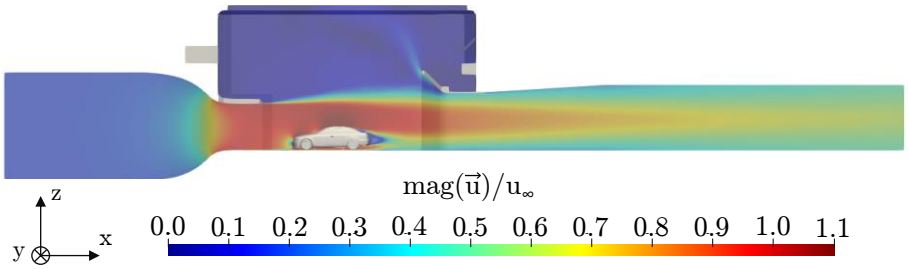

Figure 74: Side view of the CFD domain of the AAWT with the DrivAer in the test section. Distribution of the velocity magnitude at y=0.

In Figure 75, a 3D view of the DrivAer model in the AAWT CFD setup is shown. In this figure, the velocity distribution and the numeric mesh at y=0m depicted are depicted as well. Next to the refinement regions for the shear layer, the refinement regions around the vehicle can be seen. The refinement regions are shaped to get a meaningful numerical result for the flow around the vehicle. Still, it is a trade-off between numerical accuracy and the available computational resources. The refinement regions are mainly extended behind the vehicle to resolve the wake within a finer mesh. In the following chapter, experimental and numerical results are used to validate the used CFD setup with its refinement regions. The described CFD setups will be used in the following chapter to investigate not only the influence of the AAWT geometry on the aerodynamic results but also the influence of the new inlet boundary condition on the time-averaged and time-resolved data.

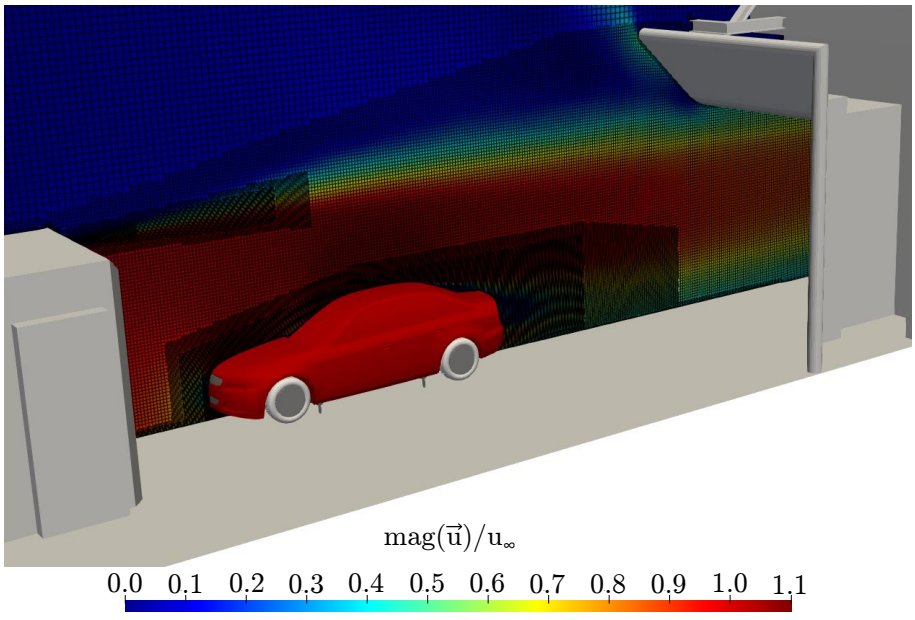

Figure 75: DrivAer in the AAWT test section. Distribution of the velocity magnitude and numerical mesh with refinement regions at y=0.

4.2 Simplified DrivAer Model

The results of the empty test section lead to the assumption that the prediction of the numerical flow field around the vehicle can also be improved by using the new optimised CFD setup. To evaluate this assumption, different wind tunnel tests and data are compared to numerical results. It is well known that including the wind tunnel geometry in the CFD setup is crucial for a comparison of wind tunnel and CFD results. Mostly this is done to represent the pressure gradients of the wind tunnel or, in general, to represent all wind tunnel interference effects in the CFD setup. In the following, this influence will be considered by comparing the CFD results of the ideal box setup with the AAWT CFD setup. Novel insights will be generated by comparing these results with the optimised CFD setup, which not only represents the wind tunnel interference effects like pressure gradients or shear layer influences but also includes the wind tunnel eigenmodes of the AAWT. With these three CFD setups, a lot can be learned. With the assumption that the ideal box setup provides an ideal flow around the vehicle, these results are the basis for the comparison and it can be analysed how the AAWT geometry influences the flow around the vehicle. After analysing the influence of the AAWT geometry, the influence of the wind tunnel eigenmodes can be evaluated with the help of the newly introduced optimised CFD setup. The last step then is to compare the CFD result with the AAWT geometry and the AAWT eigenmodes with experimental data from the AAWT. Ideally, the results of the different CFD setups should incrementally bring the numerical results closer to the experimental data.

In the first step, the DrivAer model without wheels, see Figure 7 and Figure 72, will be used to compare the numerical and experimental results. This has the advantage that only a simple bluff body is investigated. This should lead to a simpler flow field with fewer vortical structures compared to the DrivAer model with wheels. This is due to the wheels, which would cause additional vortical structures. With this simplified vehicle geometry, it should be easier to identify dominant coherent structures in the wake of the DrivAer. This will be important for the comparison of the time-resolved flow field data and how the frequencies of vortical structures are influenced by the different CFD setups. The background of this investigation will be explained in more detail later. Also, the simplified DrivAer model without wheels and closed wheelhouses helps to reduce deviations between the experimental and numerical vehicle models. Therefore, the time-averaged flow field data is easier to compare because fewer geometry deviations are expected.

The integrated forces, respectively, the force coefficients, are a good indicator of the quality of CFD results. Comparing them with the wind tunnel results allows a first insight into the quality of the simulated flow. In Table 8, the delta force coefficients of the different CFD setups compared to the wind tunnel experiment are given.

Table 8: Delta force coefficients of the DrivAer model without wheels for the different CFD setups compared to the wind tunnel results.

Setup	Δc_d	Δc_{lf}	Δc_{lr}
Wind Tunnel	-	-	-
Box CFD	+0.008	-0.032	+0.015
AAWT CFD	+0.001	-0.024	+0.023
AAWT CFD with eigenmodes	+0.001	-0.020	+0.023

In Table 8, the delta values of the drag and lift coefficients are given in respect to the wind tunnel results. For the drag coefficient, it can be seen that the highest delta can be found for the Box CFD setup. In the Box CFD setup, the drag coefficient is c_d=0.008 higher compared to the AAWT experiment. This deviation can be explained by the absence of the AAWT geometry in the simulation. Without the AAWT geometry, the pressure gradient of the wind tunnel is not acting on the vehicle and therefore, the resulting forces are different. By adding the wind tunnel geometry to the CFD setup, the delta is reduced. Both AAWT CFD setups have a smaller deviation with only Δc_d=0.001. This shows that by adding the AAWT geometry, a better agreement between the numerical and experimental drag coefficients can be achieved. This can be explained by the different wind tunnel interference effects, which are now also present in the CFD setup. This underlines the importance of the wind tunnel geometry being represented in the CFD setup for validation investigations. Furthermore, it can be seen that the AAWT setup with the wind tunnel eigenmodes has no influence on the drag coefficient compared to the AAWT setup with a constant inlet velocity boundary condition. Hence, a first conclusion can be that the eigenmodes have only little to no influence on the time-averaged drag coefficient of the DrivAer model without wheels.

Looking at the front lift coefficient, similar conclusions can be drawn. The delta becomes smaller by adding the wind tunnel geometry and gets even smaller by adding the wind tunnel eigenmodes to the CFD domain. The reason why the wind tunnel eigenmodes have an influence on the front lift but not on the drag coefficient cannot be fully explained. No major differences in the flow field in the front half of the DrivAer model could be observed. The reason for the different lift values for the constant inlet and the inlet with the wind tunnel eigenmodes must be investigated in further studies.

Lastly, the rear lift coefficient shows different results. In the rear, the deviation for both AAWT CFD setups is greater than the Box CFD setup. Again, the wind tunnel eigenmodes have no influence on the rear lift coefficient and for

both AAWT setups, the deviation is at Δc_{lr}=0.023 compared to the wind tunnel experiment. The result for the Box setup is slightly better with Δc_{lr}=0.015. One should not pay too much attention to these results because, in the Box CFD setup, the pressure gradient from the AAWT is not simulated and therefore, the pressure distribution around the vehicle is not equivalent to the experiment. This means that different pressure forces are acting on the car in the AAWT compared to the Box CFD setup. That the deviation for the Box CFD setup is smaller compared to both AAWT setups, where the correct pressure distribution in the test section is simulated, could be just a coincidence.

For the DrivAer model with the notchback geometry, CFD codes based on Spalart-Allmaras DDES often have problems correctly predicting the flow over the rear window. This can be seen in the work of Hupertz et al. [74], where different CFD codes with Spalart-Allmaras DDES are compared to experimental data with the result that many codes cannot predict the experimental result. This is a general problem for all the used CFD setups in this investigation. This can be seen in the surface pressure on the top of the DrivAer model, which is depicted in Figure 76.

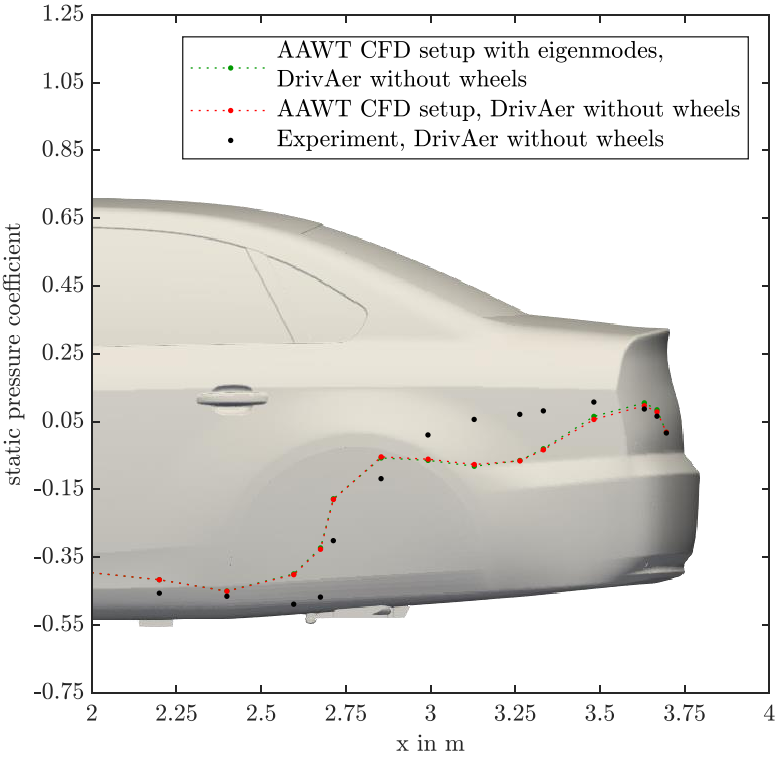

Figure 76: Static pressure distribution on the surface of the DrivAer model without wheels in y=0m on top of the vehicle.

In Figure 76, the surface pressure on top of the vehicle is depicted for the numerical and experimental results. More surface pressure results of this vehicle can be found in Appendix B. The static pressure coefficients of the wind tunnel measurement are displayed as black dots and the CFD results are plotted in red. The pressure is measured with the surface pressure probes of Figure 9, specifically with the probe points in y=0m. In the CFD setup, the pressure is measured at the same positions as in the wind tunnel experiment with specific probe points to enable a good comparison. Between each CFD data point, a dotted line is plotted, which helps for the visualization of the pressure distribution along the y=0m line. To further increase the comparability of the numerical and experimental results, the AAWT setup is used in the CFD, which ensures a comparable pressure distribution in the test section around the vehicle for the experiment and the simulation. In Figure 76, the problem of the notchback DrivAer can be seen. The static pressure coefficients in the back of the vehicle from x=3.6m onwards have a good correlation between the numerical and experimental results. Also, the results in front of x=2.5m are quite comparable. Between x=2.5m and x=3.6m, deviations between the numerical and experimental pressure data are present. In Figure 76, the DrivAer geometry is plotted in the background to better see at which point of the geometry the deviations are starting. Looking at the geometry, it can be seen that at the start of the increasing curvature from the roof to the rear window, at around x=2.5m, the deviation between the wind tunnel and CFD result is starting. The CFD predicts at this curvature a greater pressure coefficient compared to the wind tunnel result. This could be explained by a different flow separation behaviour in the CFD from the roof at this curvature compared to the flow in the wind tunnel. Because of the flow separation at the roof curvature, the pressure distribution on the rear window and the trunk lid is also different to the experimental results. It can also be seen that the AAWT CFD setup with eigenmodes has nearly no influence on the pressure distribution on the surface of the DrivAer. It would be expected that the added fluctuations generate a higher level of turbulence which helps the flow to stay attached to the rear window for longer. Since this is not the case, something is stopping the added turbulence from getting to the boundary layer. This could be explained by the fact that the boundary layer is solved by RANS, where transient fluctuations or vortical structures are not simulated. Therefore, the added eigenmodes have no influence on the boundary layer at the rear window, respectively, the pressure distribution on the surface. This deviation of the flow on the top of the vehicle in the back half is one explanation for the deviations in the rear lift coefficients. Later the problem of the flow separation at the roof curvature will be seen in different plots of the flow field as well.

To summarize the comparison of the force coefficients, it can be said that the drag coefficients have fewer deviations from the experiment by adding the wind tunnel geometry. A little influence of the wind tunnel eigenmodes on the front lift can be observed and a general deviation of the flow over the back of the vehicle is stated.

In the next step, the flow field in the wake of the DrivAer model is analysed. Hot-wire measurements in the wake of the DrivAer model are used to investigate the flow field behind the vehicle. A specific measurement plane behind the vehicle is used. This plane is placed 0.75m behind the vehicle and 0.285m above the ground. The plane for the DrivAer without wheels is 0.9m high and 1.2m wide, reaching from y=0m to y=-1.2m. The measurement plane and its relation to the vehicle are depicted in Figure 77.

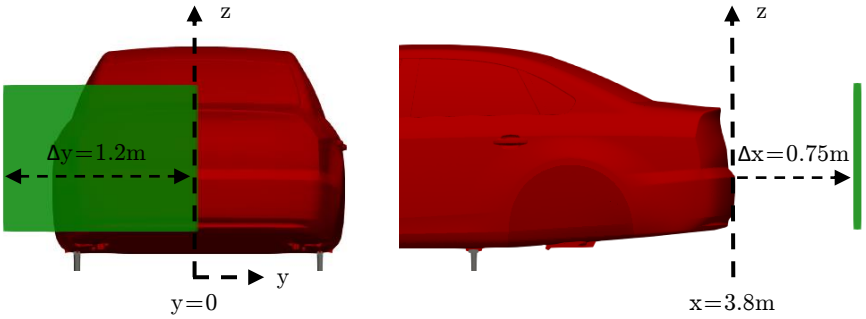

Figure 77: Measurement plane of the hot-wire measurements in the wake of the DrivAer geometry without wheels. x=0.75m behind the vehicle, from y=0m to y=-1.2m and from z=0.285m to z=1.185m.

The green measurement plane has been divided into an equidistant grid with a distance of 0.05m between the grid points. On each point, the wind speed is measured by the hot-wire for six seconds, equal to the simulated time. With the measurements of all grid points, a flow field can be interpolated for the plane. For the numerical results, probe points in the simulation are used to sample the simulated wind speeds at the same position as the hot-wire in the wind tunnel experiment. On the sampled numerical results, the hot-wire weighting factors for each direction of the flow, see Table 2, are applied. In combination with the same postprocessing and interpolation method as for the experimental data, the given results in Figure 78 can be compared without any discrepancies regarding the spatial or temporal resolution of the data-gaining process. The results of the interpolated flow field for different setups can be seen in Figure 78. There, results are plotted from experimental and numerical investigations plotted.

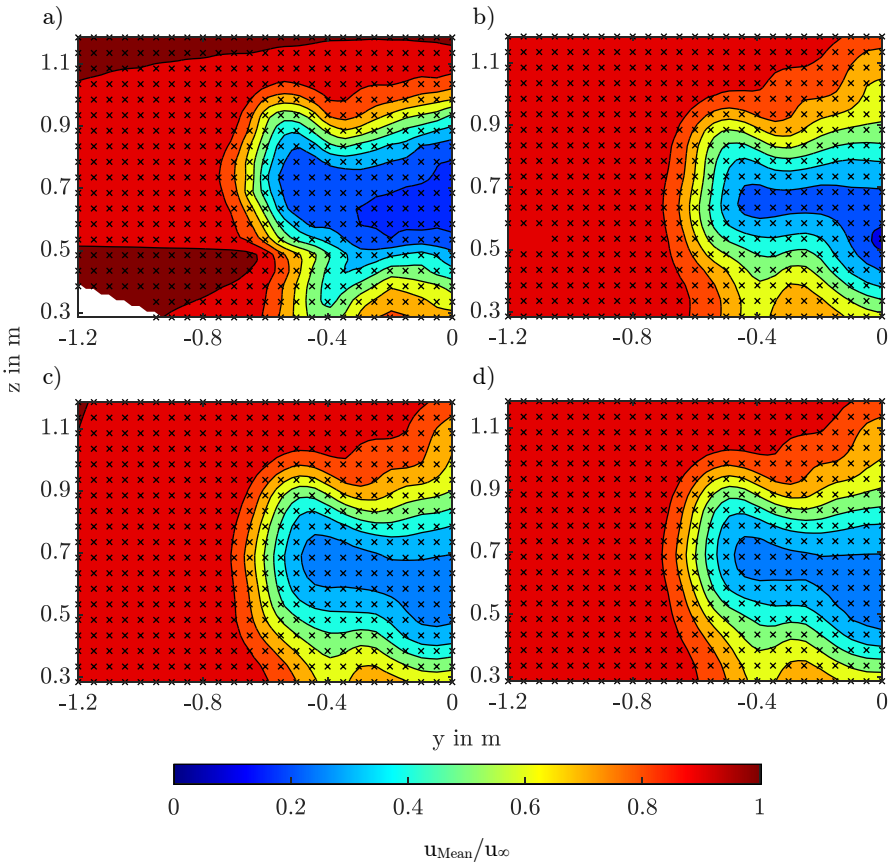

Figure 78: Time-averaged velocity distribution in the wake of the DrivAer without wheels at y=0.75m behind the vehicle. Normalized with u_∞=38.89m/s. a) wind tunnel experiment, b) Box CFD setup, c) AAWT CFD setup, d) AAWT with eigenmodes CFD setup.

In Figure 78, four different measurements of the time-averaged velocity distribution in the DrivAer wake are depicted. The reference for the comparison is the hot-wire measurement in the AAWT, shown under a). The remaining three plots are all numerical results with different domain geometries. The Box CFD setup is given under b), the AAWT CFD setup with a constant inlet velocity is given under c) and the AAWT CFD setup with the AAWT eigenmodes at the inlet is given under d). The black crosses represent the measurement points of the wind tunnel experiment a) and the sampling points in the CFD b) - d). All the CFD results are similar and all are different to the experimental result. One major difference is the free stream velocity. In the wind tunnel measurement, a) some regions in the free stream have slightly higher wind speeds compared to the same region in the CFD results. This velocity difference can be caused by the way the wind tunnel wind speed is set and controlled. The wind speed in the wind tunnel is controlled on the basis of the nozzle method, which uses a pressure difference in the wind tunnel nozzle. Pressure probes with two different positions

in the x-direction are in the wind tunnel nozzle. Between these two positions, the pressure difference is measured. With a calibration curve, a distinctive pressure difference can be used to set a specific wind speed in the test section centre. This calibration curve is determined for the empty test section. With a vehicle in the test section, a pressure build-up in front of the vehicle could cause an increase of pressure in certain parts of the wind tunnel nozzle, see chapter 1.2. With the increased pressure in the nozzle and the calibration of the wind tunnel, slightly higher wind speeds can be expected in the test section. In the CFD setups, a constant mean velocity is defined at the inlet boundary condition and therefore the pressure build-up in the nozzle has no influence on the wind speed in the test section. Collin [12] shows differences in the flow field between methods to control the wind speed in the wind tunnel and the CFD. According to these results, the method for the AAWT experiment and the CFD setup of the current investigation have a good correlation and can be used for the upcoming comparisons.

The next major difference between the experimental and numerical results can be seen in the upper part of the wake near y=0m. In the three CFD results, the shear layer between approximately z=0.8m and z=1.2m is very wide compared to the shear layer of the experimental wake in the same region. This deviation is caused by the wrongly predicted flow separation at the transition from the vehicle roof to the rear window. This phenomenon has already been explained with the surface pressure distribution in Figure 76. The wrongly predicted flow separation of the CFD at the roof and rear window causes differences in the measurement plane of the wake. Like mentioned before, neither the domain geometry, namely Box or AAWT, nor the setup with or without eigenmodes have an influence on the flow separation problem and therefore the deviation in the upper shear layer can be seen for all three CFD setups of Figure 78.

The wind tunnel geometry has the strongest influence on the velocity distribution in the wake of the CFD results. Comparing the results of the Box CFD setup in b) with both AAWT CFD setups in c) and d) shows that the overall shape of the wake is very similar for all CFD setups, but the minimum wind speed in the wake of the Box setup is a little lower compared to the AAWT setups. One explanation could be that the shear layer of the test section on the AAWT setups has an influence on the wake at this position behind the vehicle and that the added flow energy from the shear layer induces higher wind speeds into the wake due to some cross flows inside the test section flow and therefore a higher mixing in the shear layer of the vehicle's wake. Due to the spatial averaging based on the single-wire hot-wire weighting factors, specific flow directions cannot be investigated and the exact cause for the slightly higher wind speeds in the wake in the AAWT CFD setups cannot be stated. The addition of the AAWT eigenmodes at the inlet of the AAWT CFD setup has little to no influence on the wake of the DrivAer.

According to the findings from the force coefficients and the surface pressure, also for the time-averaged velocity distribution, it can be seen that domain geometry has the strongest influence on the results. The influence of the added eigenmodes of the AAWT is only very small. In the following, the influence of the different CFD setups on the time-resolved flow field will be investigated.

For the investigation of the time-resolved flow field, a FFT analysis is applied on the measurements in the wake of the DrivAer. The measurement plane, see Figure 77, and the grid resolution of the time-averaged velocity distribution investigation, see Figure 78, are used for the evaluation of the time-resolved flow field. The measurement on each grid point has a duration of six seconds. For the FFT analysis, all measurement points are used to form an averaged FFT plot for all measurement points combined. Sebald et al. [38] introduced this method of averaging the power spectral density (PSD) for each frequency of the FFT analysis to get an combined FFT result over the whole measurement plane. This means that each hot-wire signal is processed to get a FFT result and then all PSD values from the single measurements are averaged for the respective frequency. This gives a good overview of the main transient structures in the measurement plane. The flow structures for a big area can be evaluated within one FFT plot. It is easy to investigate the major differences between the CFD setups and the wind tunnel experiment. This method is applied to the experimental hot-wire measurements and the CFD data with equal FFT parameters. Therefore, a comparison of the time-resolved numerical and experimental data can be made.

At first, in Figure 79, the averaged FFT plot of the wind tunnel experiment is depicted. In this investigation, the focus is on the low-frequency range and therefore the frequencies between 0Hz and 25Hz are plotted. In chapter 1.2, the eigenmodes of open-jet wind tunnels and their cause are explained. In chapter 3.2, the eigenmodes of the empty test section of the AAWT are given, namely 2.4Hz, 4.25Hz, 5.25Hz and 6.5Hz. Therefore, the analysis is focused on the low-frequency region of up to 25Hz.

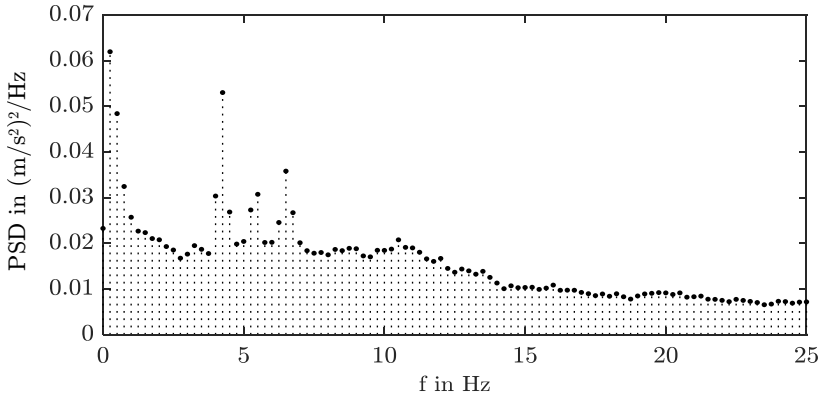

Figure 79: Spatially averaged FFT in the wake of the DrivAer without wheels at y=0.75m behind the vehicle, wind tunnel experiment in the AAWT.

Evaluating the FFT plot in the wake of the DrivAer without wheels of the wind tunnel experiment reveals that there are also some peaks for some distinct frequencies. The high values near 0Hz are coming from the zero mode and the constant term of the hot-wire signals. The main peaks can be found at 4.25Hz, 5.5Hz and 6.5Hz. These frequencies are according to the wind tunnel eigenmodes of the AAWT. Interestingly, there is a small shift for the 5.25Hz mode of the empty test section, which is now at 5.5Hz in the wake of the vehicle. This could be related to a lock-on phenomenon between the wind tunnel and vehicle wake modes. Such a phenomenon is also suspected by Sims-Williams et al. in [45]. Furthermore, the 2.4Hz mode is not present in the FFT result. Instead, a small peak at 3.25Hz can be seen. The last noteworthy peak is at 10.5Hz, which is also an eigenfrequency of the AAWT empty test section. This eigenmode can be seen in Figure 55 in the FFT result of the hot-wire measurement in the settling chamber with an empty test section. It can be said that in the wake of the DrivAer without wheels, mainly wind tunnel eigenmodes are present in the spatially averaged FFT plot. However, some frequencies are now shifted compared to the eigenmodes of the empty test section. It can be assumed that the high proportion of wind tunnel eigenmodes in the FFT result is caused by the relatively big free stream area in the measurement plane. But also, the wind tunnel eigenmodes are resonance effects, which lead to global pressure fluctuations in the whole test section of the wind tunnel. These resulting fluctuations in the wind tunnel flow can also be measured by the hot-wire. Additionally, the frequencies of the DrivAer could coincidently be similar to the AAWT eigenmodes and therefore the wind tunnel and vehicle eigenmodes are summed up to the same peaks. Obviously, the DrivAer model in the test section is causing a frequency shift for some of the wind tunnel eigenmodes. At the vehicle, the flow separation from the body causes vortical structures in the wake with specific frequencies comparable to the wake of a cylinder. It is assumed that the vortical structures of the vehicle and their frequencies interact with the eigenmode frequencies of the wind tunnel, especially when their frequencies are similar to the wind tunnel eigenmodes.

The FFT result of the Box CFD setup in Figure 80 is used to analyse frequencies of the vortical structures coming from the DrivAer model without wheels in ideal conditions without wind tunnel interferences.

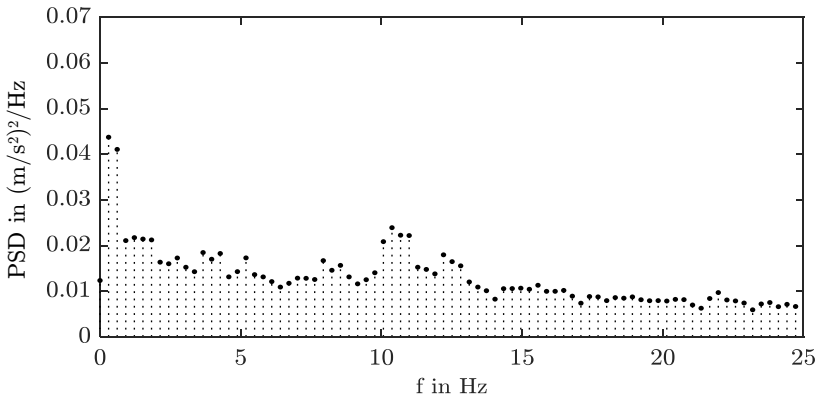

Figure 80: Spatially averaged FFT in the wake of the DrivAer without wheels at y=0.75m behind the vehicle, Box CFD setup.

In Figure 80, the FFT result of the DrivAer wake for the Box CFD setup is depicted. The FFT analysis is conducted with the same spatial averaging and the same parameters as the experimental FFT. In the FFT results of Figure 80, one can see some distinct frequencies. The main peaks are at 2.8Hz, 3.7Hz, 4.3Hz, 5.2Hz, 7.9Hz, 8.6Hz, 10.4Hz and 12.2Hz. In the Box CFD setup, it is assumed that the flow around the vehicle is ideal in the way that no wind tunnel interference effects are present. Hence, the transient flow structures in the FFT should only be caused by vortical structures which are arising from the vehicle itself. Therefore, comparing the main frequencies of the Box CFD setup with the experimental FFT result provides insight into how the frequencies of the vortical structures of the vehicle and the wind tunnel eigenmodes interact. Interestingly, the DrivAer model without wheels has dominant vortical structures in the wake at around 4.3Hz, 5.2Hz and 10.4Hz. These frequencies coincide with the eigenmodes of the AAWT or, rather, are very similar to the AAWT eigenmodes. Therefore, it can be assumed the peaks in the FFT of the wind tunnel experiment are amplified due to the superposition of the frequencies and, potentially, the vortical structures coming from the vehicle itself are amplified. The vortical structures with the frequencies of 7.9Hz and 8.5Hz are not really visible in the FFT results of the wind tunnel experiment, see Figure 79. These structures do not coincide with major wind tunnel eigenmodes and apparently are not present with a high PSD in the experimental data. Lastly, the 2.8Hz and 3.7Hz could cause an interesting effect. In the experimental FFT result, the 2.4Hz of the empty test section seems to be shifted to 3.2Hz for the measurements with the DrivAer model. The superposition of the 2.4Hz wind tunnel eigenmodes with the vortical structures of the DrivAer with 2.8Hz and 3.7Hz could cause the frequency to be shifted to the observed 3.2Hz of the wind tunnel experiment. Therefore, a lock-on effect between the vehicle vortical structures and the wind tunnel eigenmodes could be present. The analysis of the Box CFD setup gives a good insight into the vehicle frequencies for an ideal flow without wind tunnel interference effects, but to better understand the frequency shifts between the

Box CFD setup and the experimental results, the influence of the AAWT geometry and thus the wind tunnel interference effects must be evaluated.

In the next step, the FFT result for the AAWT CFD setup with a constant velocity boundary condition is analysed. This adds, as a first step, the AAWT geometry and therefore time-averaged interference effects like the pressure gradient. The result can be seen in Figure 81.

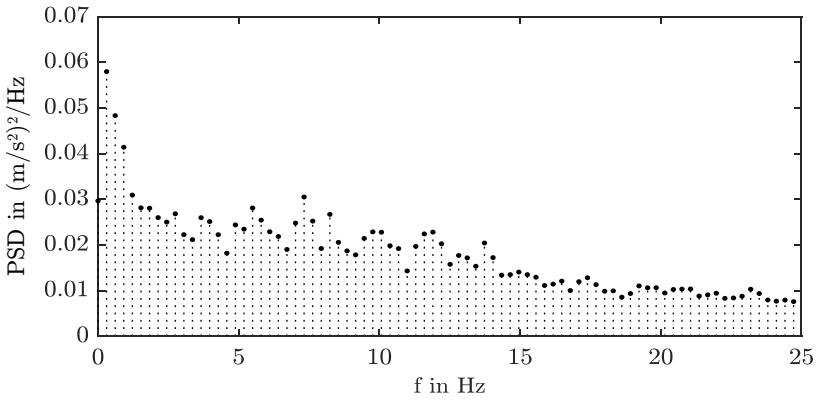

Figure 81: Spatially averaged FFT in the wake of the DrivAer without wheels at y=0.75m behind the vehicle, AAWT CFD setup.

In Figure 81, the FFT result for the DrivAer model in the AAWT CFD setup is depicted. Like before, there are some dominant vortical structures present in the wake of the vehicle, which leads to dominant peaks in the FFT. The dominant peaks are at 2.8Hz, 3.7Hz, 5.5Hz, 7.3Hz, 8.2Hz, 10.0Hz and 11.9 Hz. The low-frequency modes at 2.8Hz and 3.7Hz seem to be the same as for the Box CFD setup and no influence of the AAWT geometry on these structures can be observed. For the peaks at 8.2Hz, 10.0Hz and 11.9Hz as well, only a small difference to the Box CFD setup can be seen. The 4.3Hz mode of the experiment and the Box CFD setup is not present in the FFT result of the AAWT CFD setup. This is not as expected since the 4.25Hz is a wind tunnel eigenmode and the Box CFD setup shows a 4.3Hz vehicle structure, and now, by combining the wind tunnel flow with the vehicle flow, this mode doesn‘t seem to be present anymore. One explanation could be that by the superposition of the only partially correct simulated wind tunnel flow of the AAWT CFD setup with the vehicle flow, this mode is somehow cancelled out. Partially correct wind tunnel flow means that the wind tunnel eigenmodes are not yet added to the CFD setup. But since the AAWT geometry is simulated with the nozzle, the shear layer of the AAWT is still simulated. This adds some of the transient effects taking place in the test section of the AAWT. Furthermore, a slight shift of the peak at 7.3Hz can be assumed compared to the Box CFD setup, where a peak nearby at 7.9Hz is present. This shift could be caused by the wind tunnel flow of the AAWT geometry. A small shift can also be seen for the 5.5Hz mode compared to the 5.2Hz mode in the Box CFD setup. This peak is also very dominant in the FFT

result of Figure 81. This can be explained by the fact that the wind tunnel eigenmode coming from the shear layer of the AAWT geometry and vehicle mode at around 5.2Hz are superimposed and amplified. The reason for the slight shift needs to be investigated. Overall, in contrast to the time-averaged investigations, the wind tunnel geometry itself has only a small influence on the flow field. With the constant velocity boundary condition, it seems that the time-resolved flow field is not predicted correctly. So it is of great interest to evaluate the flow field for the AAWT CFD setup with eigenmodes to see how the new boundary condition influences the time-resolved flow field.

In Figure 82, the FFT result of the AAWT CFD setup with eigenmodes for the wake of the DrivAer without wheels is depicted. It can be seen that the amplitude and frequency of the FFT peaks are different to the AAWT CFD setup in Figure 81, where the AAWT eigenmodes are not added to the flow.

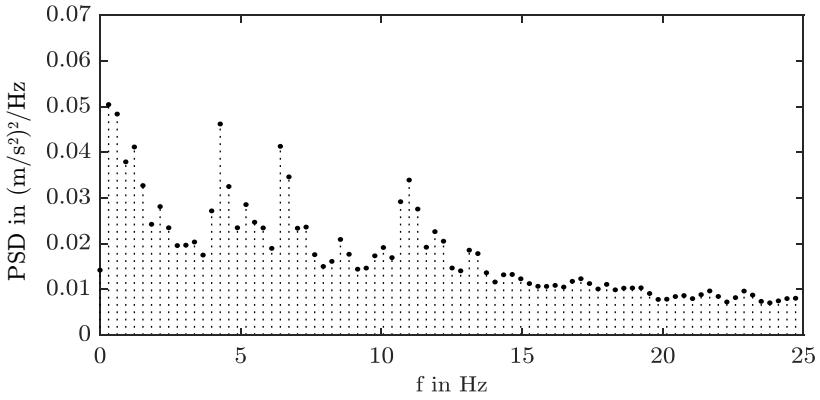

Figure 82: Spatially averaged FFT in the wake of the DrivAer without wheels at y=0.75m behind the vehicle, AAWT CFD setup with eigenmodes.

In Figure 82, the FFT should include not only the vortical structures of the vehicle wake and some structures and eigenmodes of the AAWT, like in Figure 81 but also the amplified eigenmodes of the AAWT resulting from the new inlet boundary condition. Comparing the overall amplitudes of the FFT result shows that the amplitudes for the AAWT CFD setup with the added eigenmodes are higher than the amplitudes of the AAWT CFD setup without added eigenmodes. Now the amplitudes of the CFD result are much more similar to the amplitudes of the experimental FFT result in Figure 79. Therefore, it can be said that for the amplitudes alone, adding the eigenmodes at the inlet of the CFD domain is necessary to get numerical results comparable to the wind tunnel experiment. FFT peaks in Figure 82 show that there are peaks at 4.3Hz, 5.2Hz, 6.4Hz, 7.3Hz, 8.6Hz, 10.1Hz, 11.0Hz and 11.9Hz. The first peaks at 4.3Hz, 5.2Hz and 6.4Hz are not only similar to the wind tunnel eigenmodes of the AAWT but can also be found in the FFT result of the Box CFD setup. Therefore, these vortical structures from the vehicle are superimposed with wind tunnel eigenmodes with similar frequencies, which leads to the given FFT results. In this result, the

frequencies are slightly shifted and have a greater amplitude. Both can be caused by the superposition of the wind tunnel eigenmodes and the vortical structures from the vehicle having very similar frequencies. Also, the frequency of these three peaks and their amplitude of the FFT result of the AAWT CFD setup with eigenmodes have good agreement with the experimental result. The following peaks at 7.3Hz and 8.6Hz are very distinct in the CFD FFT result of Figure 82 but are not really present in the experimental FFT result of Figure 79. These frequencies should refer to vortical structures coming from the vehicle because similar peak frequencies can be found for the Box CFD setup, where only vehicle structures should be present in the FFT result. These peaks with a slight frequency shift are present in the AAWT CFD setup with eigenmodes. The frequency shift can be caused by the wind tunnel eigenmodes in this CFD setup. The next three peaks at 10.1Hz, 11.0Hz and 11.9Hz are also very interesting and probably a mix of vehicle structures and wind tunnel eigenmodes. The 10.5Hz peak can be found in the empty test section as a wind tunnel eigenmode and is also present in the FFT result of the experiment. In the case of the AAWT CFD setup with eigenmodes, the 11.0Hz is very dominant and could be referred to as the 10.5Hz eigenmode in combination with the vehicle frequencies of 10.4Hz and 12.2Hz of the Box CFD setup. These two vehicle frequencies can still be found in the FFT result of Figure 82 with similar frequencies, namely 10.1Hz and 11.9Hz. Overall the FFT result of the AAWT CFD setup with eigenmodes has a good agreement with the experimental FFT result and applying the wind tunnel eigenmodes as an inlet boundary condition helps to close the gap between the numerical and experimental FFT result.

The FFT peaks with the highest PSD amplitude are the peaks where the vehicle vortical structures coincide with the AAWT eigenmodes. Where these two flow phenomena are combined, intense fluctuations in the flow field can be observed. Furthermore, it can be observed that vehicle frequencies may lock on to wind tunnel eigenmodes and their natural frequency is thereby shifted. It is crucial to take this into account for time-resolved investigations on the vehicle wake. It can also be seen that for the FFT peaks, where vehicle and wind tunnel modes are in resonance or locked on, a very sharp peak is present in the FFT. That peaks in resonance becoming sharper is in accordance with the hypothesis of [15].

Concluding the investigation with the DrivAer model without wheels, the following findings can be drawn. The new time-varying boundary condition has only a very small influence on the averaged integrated forces and their force coefficients. This is also the case for the time-averaged flow field. The geometry of the AAWT has a bigger influence than the wind tunnel eigenmodes. To get comparable results between the AAWT experiment and the CFD, it is important to use the AAWT geometry in the CFD. This ensures that all the time-averaged wind tunnel interference effects, like pressure gradients in the test section, are represented in the CFD setup. These interference phenomena are the main effects of time-averaged results. The time-resolved interference effects, like wind tunnel

eigenmodes, are important for investigations based on time-resolved data. Therefore, the new time-varying boundary condition, which brings the wind tunnel eigenmodes into the CFD domain, is important for the investigation of vortical structures in the wake of the vehicle. It can be seen that the new boundary condition has a huge influence on the CFD results and only by adding the wind tunnel eigenmodes to the CFD flow the FFT results of the CFD and the AAWT experiment can be compared. Furthermore, with the new boundary condition, it can be shown that the CFD is able to predict the vortical structures in the wake of the vehicle with the frequencies and amplitudes like in the AAWT experiment. With this correct simulation of the time-resolved flow field, it is now possible to distinguish between wind tunnel eigenmodes and vehicle modes. This can be done by comparing the results of the Box CFD setup, where only vortical structures caused by the vehicle are present, with the results of the AAWT CFD setup with eigenmodes, where the vortical structures of the vehicle and the AAWT eigenmodes are superimposed. In the case of the DrivAer without wheels, it can be seen that some vortical structures coming from the vehicle have similar frequencies to the AAWT eigenmodes and some vehicle frequencies are separate from the AAWT eigenmodes. This insight into the time-resolved flow field is only possible due to the correct simulation of the time-resolved wind tunnel flow based on the new boundary condition. With the wind tunnel eigenmodes, the time-resolved flow can be validated with results from the AAWT experiment. This ensures that the frequencies predicted by the CFD agree with the measured frequencies of the wind tunnel experiment. With the AAWT CFD setup alone, the time-resolved flow field does not agree with the AAWT experiment. It is important to represent the wind tunnel eigenmodes in the CFD setup. With these, the influence of the wind tunnel eigenmodes on the vehicle can be investigated because only now the time-resolved wind tunnel flow is simulated correctly. Lastly, this investigation shows that the natural frequencies of the vortical structures in the wake of a vehicle can be influenced by wind tunnel eigenmodes, especially when the frequencies are similar. A lock-on effect and therefore a frequency shift of the vehicle frequencies is the consequence.

4.3 Complete DrivAer Model

The general influence of the new boundary condition on the DrivAer model without wheels has been shown in detail. Now it will be discussed how the DrivAer model with wheels reacts to the new CFD setup with AAWT eigenmodes and how the results may differ from the previous investigation without wheels. The used model for the wind tunnel experiments is depicted in Figure 8 and the virtual model for the CFD runs is depicted in Figure 73. First of all, the force coefficients for all CFD setups in reference to the wind tunnel experiment are compared. These can be seen in Table 9.

Table 9: Delta force coefficients of the DrivAer model with wheels for the different CFD setups compared to the wind tunnel results.

Setup	Δc_d	Δc_{lf}	Δc_{lr}
Wind Tunnel	-	-	-
Box CFD	+0.016	-0.014	+0.003
AAWT CFD	+0.005	-0.011	+0.011
AAWT CFD with eigenmodes	+0.005	-0.010	+0.013

In Table 9, the deltas of the force coefficients for each CFD setup in reference to the wind tunnel experiment are given. Starting with the drag coefficient, similar trends as for the DrivAer without wheels can be seen. The wind tunnel geometry itself has the biggest influence on the drag coefficient. For the Box CFD setup without the wind tunnel geometry, the delta is at Δc_d=0.016. Adding the wind tunnel geometry in the AAWT CFD setup reduces the delta to the experiment to Δc_d=0.005. The drag coefficient stays at the same value for the AAWT CFD setup with eigenmodes as for the investigation with the DrivAer without wheels. Again, for the time-averaged drag coefficient, it is more important to include the wind tunnel geometry itself than the wind tunnel eigenmodes. The presence of the correct pressure gradient around the vehicle in the AAWT CFD setup helps to predict the drag coefficient in higher accordance with the AAWT experiment. Similar findings can be drawn for the front lift coefficient. Without the wind tunnel geometry in the Box CFD setup, the delta is at Δc_{lf}=-0.014 and is reduced to Δc_{lf}=-0.011 by adding the wind tunnel geometry in the AAWT CFD setup. Like in the investigation without wheels, a small influence of the eigenmodes on the lift coefficient can be seen and the delta for the AAWT CFD setup with eigenmodes is reduced to Δc_{lf}=-0.010. For the rear lift coefficient, contrary effects can be observed. There, the deltas get bigger by adding the wind tunnel geometry and, ultimately, by adding the eigenmodes. Namely from Δc_{lr}=+0.003 for the Box setup and Δc_{lr}=+0.011 for the AAWT setup to even Δc_{lr}=+0.013 for the AAWT setup with eigenmodes. That the rear lift coefficients should not be taken into account too much can be explained by the wrong prediction of the pressure distribution over the rear window of the DrivAer, depicted in Figure 76. The CFD is not able to predict the flow over the rear window correctly. This explains not only the deviations in the rear lift coefficients but also the other force coefficients and their remaining deviations from the wind tunnel experiment. Overall, similar trends, like in the investigation of the DrivAer model without wheels, can be seen. The eigenmodes have only a smaller influence on the force coefficients, but the wind tunnel geometry has a

bigger influence and should be present in the CFD setup when comparing numerical and experimental data.

In the next step, the flow field behind the DrivAer model with wheels will be analysed. Therefore a similar measurement plane, like in the investigation without wheels, is used. This measurement plane is depicted in Figure 83.

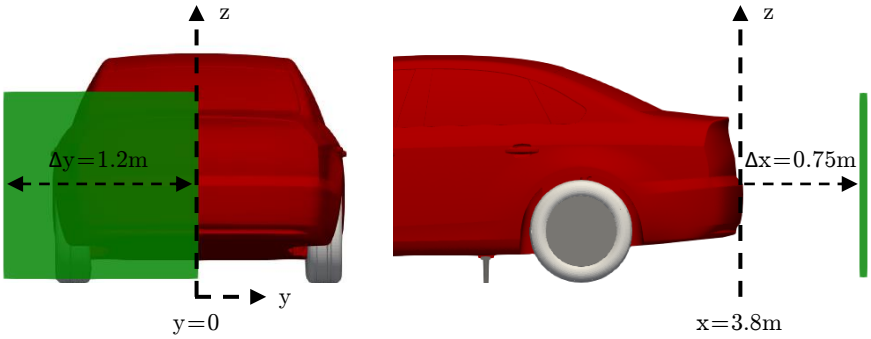

Figure 83: Measurement plane of the hot-wire measurements in the wake of the DrivAer geometry with wheels. x=0.75m behind the vehicle, from y=0m to y=-1.2m and from z=0.035m to z=1.185m.

The green measurement plane of Figure 83 is identical to the previous measurement plane of the DrivAer without wheels relating to the x-position behind the vehicle and the y-position. Also, the distance between the measurement points is identical, with 0.005m. The only difference is that the plane extends more towards the ground and starts there at 0.035m above the ground. This is necessary to measure the flow behind the wheels. All the other parameters, like the measurement time of the hot-wire and the postprocessing of the experimental data, are kept the same.

At first, the time-averaged velocity distribution behind the DrivAer model with wheels is investigated. The velocity distribution for the wind tunnel experiment and the three CFD setups are depicted in Figure 84.

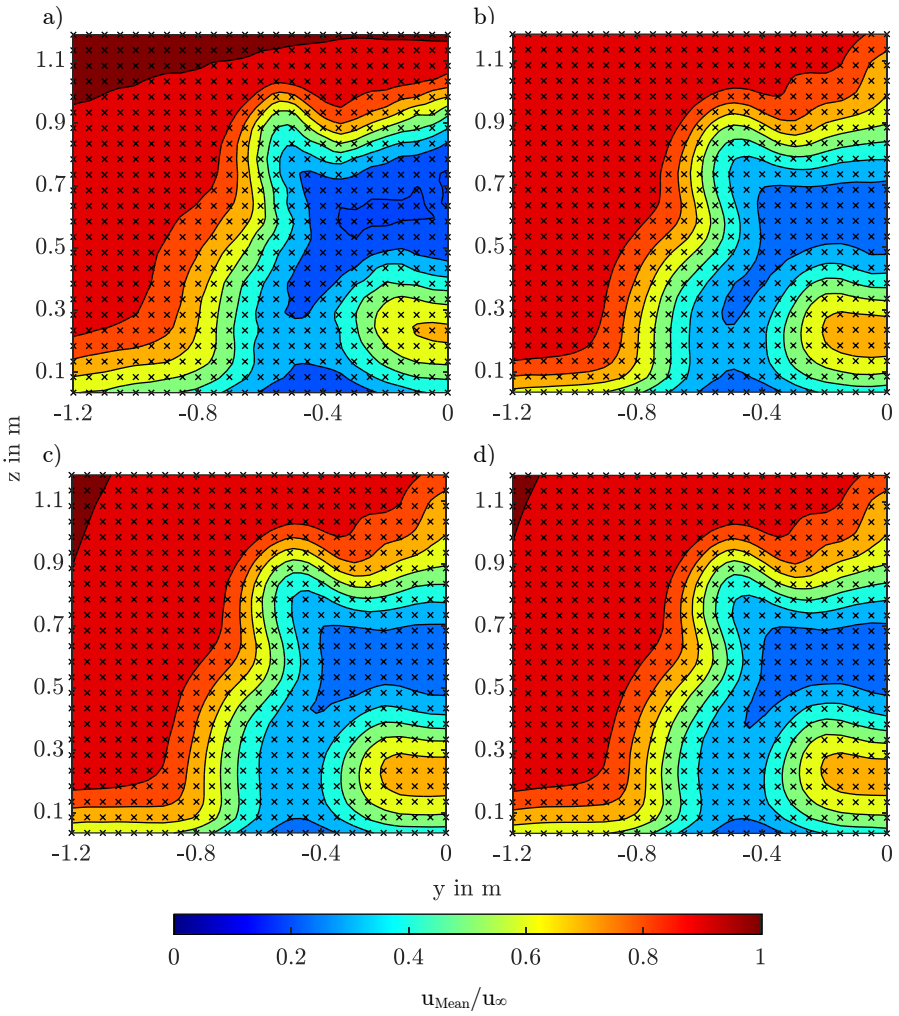

Figure 84: Time-averaged velocity distribution in the wake of the DrivAer with wheels at y=0.75m behind the vehicle. Normalized with u_∞=38.89m/s. a) wind tunnel experiment, b) Box CFD setup, c) AAWT CFD setup, d) AAWT with eigenmodes CFD setup.

In Figure 84, the four different velocity distributions can be seen. In a) the results of the wind tunnel experiment can be seen. In b) the result of the Box CFD setup, in c) the result for the AAWT CFD setup and in d) the result for the AAWT CFD setup with eigenmodes are depicted. Overall, similar findings, like in the investigation without wheels, can be seen. First of all, the free stream velocity in the wind tunnel experiment a) is different to the CFD results. In the wind tunnel experiment result, a bigger area of higher velocity is present. As aforementioned, this could be explained by the way the wind speed is set in the wind tunnel experiment. Still, for both AAWT CFD setup results in c) and d), a similar free stream velocity distribution compared to the wind tunnel experiment can be seen. This shows that adding the AAWT geometry to the

CFD setup helps to create a more comparable flow field in the CFD. The region with high velocities in the top left corner in c) and d) is comparable to the top left corner of the experiment in a). This region is different in the Box CFD setup of b), where the wind tunnel geometry is not present. This region in the Box CFD setup is different because there is no jet of the wind tunnel with the shear layer, which is causing the velocity distribution in the top left corner. The shear layer is only there in the experiment a) and the AAWT CFD setups c) and d).

The major deviation between all CFD setups and the experiment is the region at y=0m between z=0.8m to z=1.185m in Figure 84. In this region, like in the investigation without the wheels, the flow separation at the DrivAer model at the rear window is not predicted correctly in all CFD setups. This phenomenon is explained in more detail in the investigation without wheels in chapter 4.2 based on Figure 76. Because of the wrongly predicted flow separation at the rear window, the flow field downstream of the vehicle has also a deviation from the wind tunnel experiment.

Another interesting finding from the comparison of the four different velocity distributions in Figure 84 is that the lowest velocities of the CFD setups in the wake of the vehicle are found in b) for the Box CFD setup. This phenomenon is also explained in more detail in the investigation without wheels in chapter 4.2. Nevertheless, the wake behind the wheels, which is at around y=-0.3m to y=-0.7m and z=0m to z=0.4m, is predicted most correctly by the Box CFD setup in b). This is mainly due to the lower wind speeds in this area of the measurement plane, which is due to the absence of the shear layer in the Box CFD setup.

Concluding the findings shows that for the CFD results, the wind tunnel geometry has the biggest influence on the time-averaged velocity distribution in the wake of the DrivAer model with wheels. Between the CFD setups, the biggest differences can be found between the Box CFD setup and the AAWT CFD setup. The AAWT CFD setup with eigenmodes has nearly no difference from the standard AAWT CFD setup. This observation is in accordance with the previous findings from the DrivAer model without wheels and the investigation of the force coefficients.

To finalize the investigation of the DrivAer model with wheels, the time-resolved flow field needs to be analysed. In the following investigation, the FFT results of the spatial averaged FFT are used, like in the investigation of the DrivAer model without wheels in chapter 4.2.

First of all, the FFT result of the AAWT wind tunnel experiment is investigated with a focus on the difference to the result of the DrivAer model without wheels. This difference shows the influence the wheels have on the flow field and the vortical structures in the wake of the vehicle. In Figure 85, the experimental results of the DrivAer model with wheels are depicted.

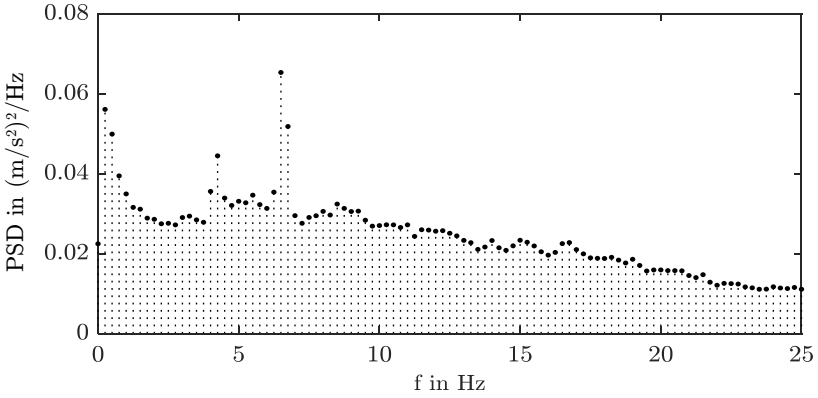

Figure 85: Spatially averaged FFT in the wake of the DrivAer with wheels at y=0.75m behind the vehicle, wind tunnel experiment in the AAWT.

The FFT result of Figure 85 from the DrivAer model with wheels shows many similarities to the FFT result of Figure 79 from the DrivAer model without wheels. Especially, the low-frequency peaks below 10Hz are very similar to the results of the investigation without wheels. The only difference here is that the amplitudes of the peaks are slightly different, but this could be caused by the different sizes of the used measurement plane. The measurement plane reaches down to the floor for the DrivAer model with wheels and therefore has a bigger area not only behind the vehicle but also on the free stream area. This could mean that some vortical structures are measured in more measurement points, which could cause a higher amplitude for the spatially averaged FFT results. Regardless of these small differences, a greater deviation between the FFT results can be seen for the peaks at 14.0Hz, 15.0Hz and 16.8Hz. These peaks are not present in the FFT result of the DrivAer model without wheels. Therefore, it is possible that these additional peaks are caused by the wheels. These peaks are not known as wind tunnel eigenmodes and should be related to the vehicle. To clarify the origin of the peaks, the DrivAer model with wheels is analysed in the Box CFD setup, depicted in Figure 86.

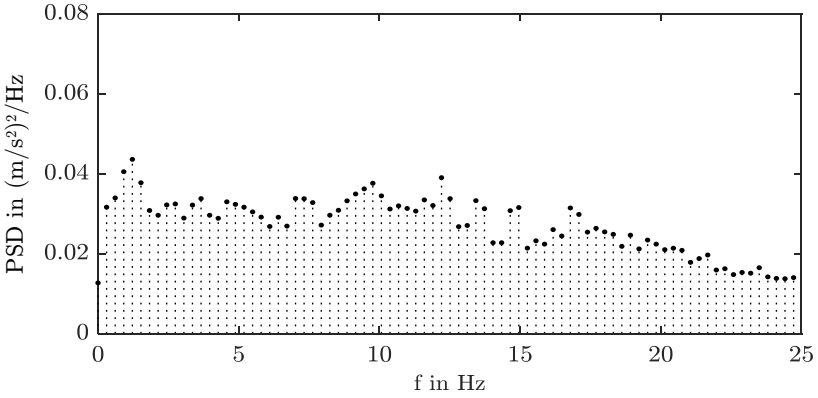

Figure 86: Spatially averaged FFT in the wake of the DrivAer with wheels at y=0.75m behind the vehicle, Box CFD setup.

In Figure 86, the FFT result of the Box CFD setup for the DrivAer model with wheels is depicted. Comparing this result with the FFT result with the vehicle without wheels shows that, again, the low-frequency range is very similar apart from some amplitude differences, which could be caused by the different measurement planes. The main differences are the added peaks at 13.4Hz, 15.0Hz and 16.8Hz. Apart from the 13.4Hz peak, which is slightly shifted compared to the 14.0Hz peak of the wind tunnel experiment, these are the exact peaks which are also new in the FFT result of the wind tunnel experiment. Relying on the fact that in the Box CFD setup, only vortical structures originating from the vehicle are present, it seems obvious that these three peaks are caused by the added wheels. The other peak at 12.2Hz can also be found in the FFT result of the DrivAer model without wheels simulated in the Box CFD setup in Figure 80 and is also a dominant vortical structure caused by the vehicle. In the next step, the influence of the AAWT geometry is investigated in Figure 87.

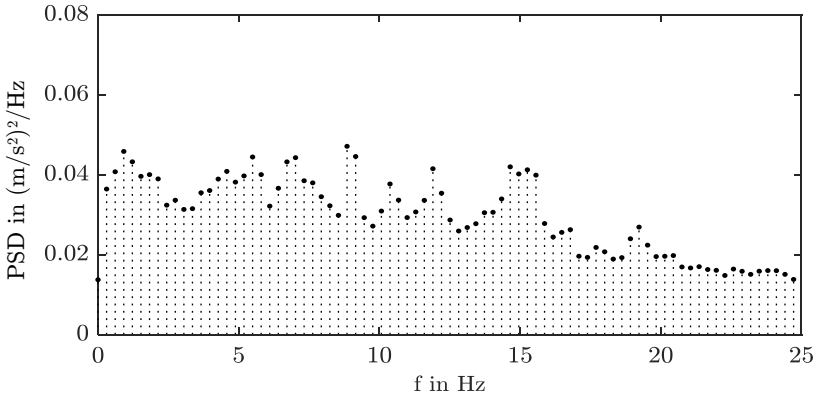

Figure 87: Spatially averaged FFT in the wake of the DrivAer without wheels at y=0.75m behind the vehicle, AAWT CFD setup.

In Figure 87, the FFT result of the DrivAer model with wheels in the AAWT CFD setup is depicted. It shows that it has huge deviations to the experimental result of Figure 85 and adding the wind tunnel geometry does not fix the deviations between the numerical and experimental FFT result, like in the investigation of the DrivAer model without wheels. Nevertheless, it is interesting that the 12.2Hz mode from the vehicle in this FFT result is shifted to 11.9Hz, like in the investigation of the vehicle without wheels. A broad peak between 14.7Hz and 15.6Hz can be observed. This could be a reference to the peaks of 14.0Hz, 15.0Hz and 16.8Hz. Why this broad peak is now present in this CFD setup cannot be explained entirely, but it also shows that only adding the wind tunnel geometry does not help to correctly predict the time-resolved flow field.

Lastly, the FFT for the AAWT CFD setup with eigenmodes is evaluated, depicted in Figure 88.

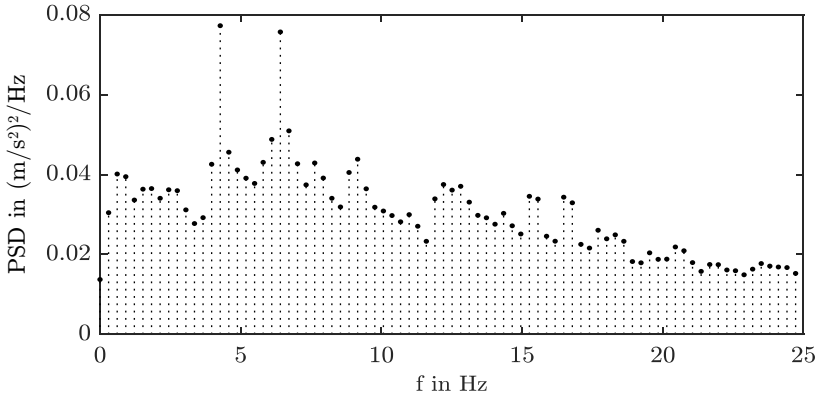

Figure 88: Spatially averaged FFT in the wake of the DrivAer with wheels at y=0.75m behind the vehicle, AAWT CFD setup with eigenmodes.

In Figure 88, the FFT result of the AAWT CFD setup with eigenmodes of the DrivAer model with wheels is depicted. In general, the FFT result of this CFD setup matches the experimental FFT result the best. Again, the addition of the wind tunnel eigenmodes to the CFD setup is crucial to correctly simulate the time-resolved flow field of a vehicle in the wind tunnel. In this FFT result, it can be seen that for the lower frequencies, the peaks and amplitudes are not only very similar to the result of the vehicle without wheels but are also very similar to the experimental result. It shows the right vehicle and wind tunnel modes in the lower frequency range. Also, the 12.2Hz mode is present in the FFT result, reassuring that this vehicle-derived vortical structure is present in the flow field with added wind tunnel eigenmodes. Also, three additional peaks can be observed in this FFT result compared to the result of the vehicle without wheels, namely the peaks at 14.3Hz, 15.3Hz and 16.5Hz. These peaks are similar but slightly shifted to the peaks found in the previous CFD FFT results for the DrivAer with wheels and are especially very similar to the experimental results. This shows again that with the added eigenmodes at the inlet boundary condition

in combination with the wind tunnel geometry, it is possible to simulate the time-resolved flow field around a vehicle in the wind tunnel. Furthermore, the three added peaks, which can be seen in the experimental FFT result and the Box CFD setup and the AAWT CFD setup with eigenmodes, must be linked to the wheels of the vehicle. It could be investigated in future studies on the time-resolved flow field of the DrivAer model with wheels what exactly is causing these vortical structures.

To conclude this investigation, it remains to say that different findings are made in this investigation compared to the investigation of the DrivAer model without wheels of chapter 4.2. First of all, the findings for the model with and without wheels are very similar and the addition of the wheels only shows some additional vortical structures in the wake, visible as additional peaks in the FFT results. Overall, tendencies and phenomena are very similar for both vehicle configurations. For both vehicles, the added eigenmodes of the AAWT CFD setup with eigenmodes only have a huge influence on the time-resolved flow field, like in the comparison of FFT results. On time-averaged characteristics, the eigenmodes only have little to no influence. The time-averaged velocity distribution in the wake of the vehicle and the time-averaged force coefficient are not really influenced by the wind tunnel eigenmodes. The wind tunnel geometry itself has a much greater influence. Therefore, it is important to add the wind tunnel geometry for comparisons of time-averaged experimental and numerical data and to add the wind tunnel eigenmodes in the CFD to compare time-resolved experimental and numerical data. Especially because with the novel boundary condition, it can be shown that there is a lock-on phenomenon between the vehicle and wind tunnel modes. This leads to the problem that the natural frequencies of the vortical structures from the vehicle can be shifted by the wind tunnel modes, particularly when the vehicle and wind tunnel frequencies are similar. Therefore, for time-resolved investigations in the wind tunnel, it needs to be analysed how the wind tunnel eigenmodes could affect the vehicle flow. This is especially relevant for vehicles with natural frequencies close to the wind tunnel eigenmode frequencies.

5 Conclusion and Outlook

Summing up this dissertation, all results of the conducted investigations and the major findings are described. Afterwards, an outlook on new potential research topics for future studies is given.

5.1 Conclusion

At first, in this dissertation, an overview of wind tunnel interference effects and their importance for evaluating experimental test results is given. Especially the wind tunnel interference caused by aeroacoustics resonance effects is an important part of this study. Early research focuses on the origin of the resonance effects and their influence on the structural integrity of the test facilities. Later the influence on measurement results is gaining interest. Many hypotheses are elaborated and some basic flow phenomena are investigated. This work builds on this research and tries to clarify in more detail potential interference effects between the wind tunnel resonance effects and the flow field around the vehicle.

The first basic and generic results for the resonance effects and interference effects like lock-on phenomena are observed in a cylinder test case. Two different cylinders are measured in different wind tunnels. In one wind tunnel, the wind tunnel eigenmodes are not similar to the natural frequencies of the vortical structures in the cylinder wake. In the other, the wind tunnel eigenmodes are similar to the cylinder frequencies. It can be seen that the frequencies of the vortical structures lock-on to the wind tunnel modes in the case of the wind tunnel with similar eigenmode frequencies. The whole frequency spectrum in the cylinder wake differs from the cylinder without lock on effect. The Strouhal number is shifted and the peaks in the frequency spectrum are sharper. Cleary, a lock-on effect is present. By trying to simulate the cylinder flow, it turns out that the result of the wind tunnel measurements, where the eigenmodes are far from the cylinder modes, a good accordance for the experiment and the numerical simulation can be achieved. In the case of the cylinder with the lock-on effect, the numerical results differ from the experimental data. The accordance for the cylinder with lock-on can be improved by adding the two most dominant wind tunnel eigenmodes as sine waves at the inlet boundary of the CFD. Then also, different shapes of the cylinder wake with and without wind tunnel eigenmodes can be seen in the CFD. With these results, it is crucial to simulate the wind tunnel eigenmodes for time-resolved investigations, where the natural frequencies of an object are near to wind tunnel eigenmodes.

The new findings are then used to enhance the CFD setup, where the geometry of the AAWT is already used as the simulation domain. The geometry ensures that flow phenomena like pressure gradients in the test section of the wind tunnel are predicted correctly. Still, a deviation to wind tunnel

measurements can be overserved for time-resolved flow phenomena. Not only that the intensity of the velocity fluctuations in the CFD is smaller than in the experiment, but also the characteristic frequencies of the experimental wind tunnel flow cannot be reproduced by the standard CFD setup with a constant velocity inlet boundary condition. Likewise to the cylinder test case, the inlet boundary of the AAWT CFD setup is changed to a time-varying boundary condition. At first, time-resolved hot-wire measurement data from the settling chamber of the AAWT is used to simulate the correct transient flow. First results seem sufficient because the intensity of the fluctuations can be increased and the eigenmodes of the AAWT measured from the hot-wire are also present in the CFD AAWT setup. But some deviations remain. Then these deviations are minimised by filtering and scaling the hot-wire signal. Measurement noise remains in the hot-wire signal and the signal would need to be adapted to different simulations time. To solve these problems, the solution of the cylinder test case is used, where sine waves with specific frequencies are added at the inlet boundary. The most dominant eigenfrequencies of the AAWT are used at the inlet. The amplitude and phase shift of the sine waves are stepwise optimised to get a good agreement between the time-resolved experimental and numerical wind tunnel flow. During the optimisation, it can be shown how different phase shifts and amplitudes of the sine waves influence the wind tunnel flow. Previous research hypotheses also can be reproduced with this new boundary condition e.g. the higher the amplitude of the frequency coming from the nozzle vortex shedding, the higher the entrainment of the shear layer. The optimised AAWT CFD setup with the wind tunnel eigenmodes now enables investigation of the influence of the wind tunnel eigenmodes on the vehicle flow. This influence is assumed based on the results of the generic cylinder test case.

Comparing the experimental results from wind tunnel measurements of the DrivAer model without wheels with different CFD setups reveals interesting findings. The different CFD setups are a Box CFD setup, the AAWT CFD setup and the AAWT CFD setup with eigenmodes. Summed up, it can be said that for time-averaged investigations like time-averaged force coefficients and velocity fields to compare the numerical results with the experimental data, it is necessary to include the wind tunnel geometry. For time-resolved investigations or comparisons to experimental data, adding the wind tunnel eigenmodes to the CFD setup is crucial. In FFT analyses, it can be seen that the wind tunnel eigenmodes influence the frequencies of the vortical structures in the wake of the DrivAer. Even a lock-on effect and frequency shift can be observed. This is due to the similarity of the natural frequencies of the DrivAer‘s vortical structures to the wind tunnel eigenmodes. The natural DrivAer frequencies can be analysed with the Box CFD setup, where no interference from the wind tunnel is present. With the added wind tunnel eigenmodes, the FFT results of the numerical and experimental data have high accordance. The same conclusions can be drawn for the DrivAer model with wheels. The only difference is that additional frequencies in the FFT can be seen. These added peaks are caused by the added wheels of the DrivAer model.

The novel boundary condition not only helps to close the gap between the time-resolved experimental and numerical flow fields but also opens the way for new research. For example, by comparing the correctly predicted wind tunnel flow of the AAWT CFD setup with eigenmodes to the Box CFD setup, it can be analysed which frequencies are caused by the vehicle, if they are close to the wind tunnel eigenmodes and if a lock-on effect can be expected. Furthermore, it can be simulated how big the wind tunnel eigenmodes influence the vehicle flow.

Overall, this dissertation shows huge deviations between the wind tunnel experiment and the numerical simulation when the aeroacoustic resonance effects of the wind tunnel are not taken into account. The dissertation then presents a sufficient solution to overcome this problem in an efficient way and achieves a high accordance between the experimental and numerical data. This shows that with the used CFD setup and the newly introduced boundary condition, it is possible to correctly predict the time-resolved wind tunnel flow.

5.2 Outlook

For the empty test section of the AAWT, major enhancements can be seen for the time-resolved numerical flow field with the novel boundary condition. Some small deviations remain and these could be eliminated by further optimising the parameters of the inlet boundary, like the amplitude and phase shift of the sine waves. New optimisation steps based on e.g. DoE or AI methods could be helpful to further reduce the deviation between the experimental and numerical flow field. This enables an even better prediction of the flow around the vehicle in wind tunnel tests.

The next step for this research topic should be to further analyse the dependencies between the wind tunnel eigenmodes and the frequencies of a vehicle. Therefore it is of high interest to better understand which length scale on a vehicle is causing what frequency. With this knowledge, it would be possible to identify crucial length scales on a vehicle. Together with the known frequencies of the wind tunnel eigenmodes, it can be estimated how similar the vehicle frequencies are to the wind tunnel frequencies and how big their influence is on the vehicle flow. With the new method and the possibility to compare experimental data with CFD setups like the Box CFD setup and the AAWT CFD setup with eigenmodes, different vehicle shapes and sizes can be analysed and characteristic length scale could be derived.

With the newly gained knowledge about the time-resolved wind tunnel interference effects, it could be sensible to use not only a single-wire hot-wire probe but a hot-wire probe with better spatial discretization. This could help to better understand the vortical structures in the wind tunnel flow and behind the vehicle. With the higher spatial resolution, it would be possible to analyse how vortical structures are spatially evolving.

Furthermore, with the newly introduced methodology, which correctly predicts the time-resolved flow field, new developments on the vehicle can be achieved. Developing new methods to reduce the aerodynamic drag of a vehicle could result in transient active flow control measures. Such active measures rely on manipulating the vortical structures arising from the flow separation of the vehicle. In an early phase of vehicle development, CFD investigations are often the only tool to develop the aerodynamics of the vehicle. To be able to develop these active drag reduction solutions with the CFD, it is crucial to predict the vortical structures and their temporal evolution like in the wind tunnel. With the updated AAWT CFD setup with eigenmodes, such developments to further reduce the drag of a vehicle should be possible.

The insights regarding the dependency between the wind tunnel eigenmodes and the vehicle flow field can also be helpful for investigations on on-road turbulences. As mentioned in chapter 1.2, a lot of research has been conducted to optimise the aerodynamic characteristics in on-road situations with turbulence phenomena coming from cross-wind or the wake of other vehicles. The new boundary condition and the first results of this dissertation enable further research regarding on-road flow situations. The different transient phenomena can be modelled using the newly introduced wind tunnel setup.

In this dissertation, a DDES method is used to simulate the time-resolved flow field of the wind tunnel and the DrivAer model. In general, this method produces sufficient results and especially with the updated inlet boundary condition, it is possible to correctly simulate the wind tunnel with a high accordance to the experiment. A great deviation of the numerical results of the DrivAer model from the experimental measurements remains in the area of the rear window, see Figure 76. Even with the updated AAWT CFD setup, this deviation cannot be eliminated. The described problems and the potential reason for this lie in the boundary layer of the vehicle, which is simulated with RANS. RANS cannot take time-resolved fluctuations of the wind tunnel into account, which is the main reason why the addition of the wind tunnel eigenmodes does not influence the flow over the rear window. Since the results for the LES region of the DDES are very accurate, the next step in developing the CFD setup should be to optimise the boundary layer simulation. One way could be to get rid of the RANS in general and use a pure LES approach instead of the DDES method. Since a pure LES requires a very fine mesh to resolve all vortical structures, this solution is very expensive regarding the computational effort. To overcome this problem, a LES with wall-stress modelling could be feasible. With this, the time-resolved flow phenomena in the near-wall region must be taken into account by the wall model. This would keep the advantages of the LES region of the DDES but may bring some advantages in the near-wall regions as well. And also, near-wall time-resolved vortical structures could be simulated or modelled. The wall-stress modelled LES and the added wind tunnel eigenmodes, could greatly impact the overall prediction accuracy.

List of Figures

List of Tables

References

[1] A. Cogotti, "Generation of a Controlled Level of Turbulence in the Pininfarina Wind Tunnel for the Measurement of Unsteady Aerodynamics and Aeroacoustics," in SAE International, 2003.

[2] C. N. H. Lock, "The Inference of a Wind Tunnel on a Symmetrical Body," ARC, Reports and Memoranda No. 1275, 1929.

[3] H. Glauert, "Wind Tunnel Interference on Wings, Bodies and Airscrews," ARC, Reports and Memoranda No. 1566, 1933.

[4] E. Mercker and J. Wiedemann, "On the Correction of Interference Effects in Open Jet Wind Tunnels," in SAE International, 1996.

[5] E. Mercker, G. Wickern and J. Wiedemann, "Contemplation of Nozzle Blockage in Open Jet Wind-Tunnels in View of Different 'Q' Determination Techniques," in SAE International, 1997.

[6] G. Wickern and B. Schwartekopp, "Correction of Nozzle Gradient Effects in Open Jet Wind Tunnels," in SAE International, 2004.

[7] E. Mercker, K. R. Cooper, O. Fischer and J. Wiedemann, "The Influence of a Horizontal Pressure Distribution on Aerodynamic Drag in Open and Closed Wind Tunnels," in SAE International, 2005.

[8] E. Mercker and K. R. Cooper, "A Two-Measurement Correction for the Effects of a Pressure Gradient on Automotive, Open-Jet, Wind Tunnel Measurements," in SAE International, 2006.

[9] G. Wickern, S. Dietz and L. Luehrmann, "Gradient Effects on Drag Due to Boundary-Layer Suction in Automotive Wind Tunnels," in SAE International, 2003.

[10] G. Wickern, "A Theoretical Approach towards the Self-Correcting Open Jet Wind Tunnel," in SAE International, 2014.

[11] G. Wickern, "Recent Literature on Wind Tunnel Test Section Interference Related to Ground Vehicle Testing," in SAE International, 2007.

[12] C. Collin, Interference Effects in Automotive, Open Jet Wind Tunnels, Munich: Technischen Universitaet Muenchen, 2019.

[13] H. Holthusen and J. W. Kooi, "MODEL AND FULL SCALE INVESTIGATIONS OF THE LOW FREQUENCY VIBRATION PHENOMENA OF THE DNW OPEN JET," in AGARD-CP-585, 1997.

[14] S. A. Arnette, T. D. Buchanan and M. Zabat, "On Low-Frequency Pressure Pulsations and Static Pressure Distribution in Open Jet Automotive Wind Tunnels," in SAE International, 1999.

[15] G. Wickern, W. von Heesen and S. Wallmann, "Wind Tunnel Pulsations and Their Active Suppression," in SAE International, 2000.

[16] O. Wehrmann, "Akustische Steuerung der Turbulenten Anfachung im Freistrahl," Jahrbuch 1957 der WGL, pp. 102-108, 1957.

[17] M. Rennie, "Effect of Jet Length on Pressure Fluctuations in œ-Open Jets," in Motor Industry Research Association Vehicle Aerodynamics 2000 Symposium, 2000.

[18] J. Lacey, "A Study of the Pulsations in a 3/4 Open Jet Wind Tunnel," in SAE International, 2002.

[19] M. Rennie, M.-S. Kim, J.-H. Lee and J.-D. Kee, "Suppression of Open-Jet Pressure Fluctuations in the Hyundai Aeroacoustic Wind Tunnel," in SAE International, 2004.

[20] F. Evert and H. Miehling, "Active Suppression of Buffeting at the Audi AAWT: Operational Experiences and Enhancements of the Control Scheme," in SAE International, 2004.

[21] X. Amandolese and C. Vartanian, "Reduction of 3/4 open jet low-frequency fluctuations in the S2A wind tunnel," JournalofWindEngineering and IndustrialAerodynamics, no. 98, pp. 568-574, 2010.

[22] Y. Wang, Z. Yang and Q. Li, "Methods to control low frequency pulsation in open-jet wind tunnel," Applied Acoustics, no. 73, pp. 666-672, 2012.

[23] D. Bao, Q. Jia and Z. Yang, "Effect of Vortex Generator on Flow Field Quality in 3/4 Open Jet Automotive Wind Tunnel," in SAE International, 2017.

[24] L. Jin, Y. Gu, X. B. Deng, H. Sun, T. Yue and J. Zhang, "Standing wave and its impact on the low-frequency pressure fluctuation in an open jet wind tunnel," Journal of Wind Engineering & Industrial Aerodynamics, no. 208, p. 104413, 2021.

[25] Q. Jia, L. Huang, Y. Zhu, M. M. Rashidi, J. Xu and Z. Yang, "Experimental research of active control optimization on a 3/4 open-jet wind tunnel's jet section," Alexandria Engineering Journal, no. 60, pp. 2265-2278, 2021.

[26] L. Jin, X. B. Deng, X. Wang, Y. Gu, Y. Liang and Z. Lian, "Standing waves in the plenum of an open jet wind tunnel: Resonance and self-excited oscillation," AIP Advances, no. 12, p. 025105, 2022.

[27] C. Schoenleber, T. Kuthada, N. Widdecke, F. Wittmeier and J. Wiedemann, "Investigation of Time-Resolved Nozzle Interference Effects," Progress in Vehicle Aerodynamics and Thermal Management, pp. 110-131, 2018.

[28] Q. Jia, Y. Zhu, D. Bao, M. M. Rashidi and Z. Yang, "On the Low Frequency Pressure Fluctuation in a 3/4 Open Jet Automotive Wind Tunnel," Journal of Applied Fluid Mechanics, pp. 1359-1369, 2019.

[29] C. Schoenleber, F. Wittmeier and J. Wiedemann, "Influence of Open-Jet Effects on Vehicle Wind Tunnel Measurements," in SAE International, 2021.

[30] J. Mayer, M. Schrefl and R. Demuth, "On Various Aspects of the Unsteady Aerodynamic Effects on Cars Under Crosswind Conditions," in SAE International, 2007.

[31] J. Wojciak, P. Theissen, K. Heuler, T. Indinger, N. Adams and R. Demuth, "Experimental Investigation of Unsteady Vehicle Aerodynamics under Time-Dependent Flow Conditions - Part2," in SAE International, 2011.

[32] D. C. Forbes, G. J. Page, M. A. Passmore and A. P. Gaylard, "A Fully Coupled, 6 Degree-of-Freedom, Aerodynamic and Vehicle Handling Crosswind Simulation using the DrivAer Model," in SAE International, 2016.

[33] D. Stoll, C. Schoenleber, F. Wittmeier, T. Kuthada and J. Wiedemann, "Investigation of Aerodynamic Drag in Turbulent Flow Conditions," in SAE International, 2016.

[34] T. Yamashita, T. Makihara, K. Maeda and K. Tadakuma, "Unsteady Aerodynamic Response of a Vehicle by Natural Wind Generator of a Full-Scale Wind Tunnel," in SAE International, 2017.

[35] D. Stoll and J. Wiedemann, "Active Crosswind Generation and Its Effect on the Unsteady Aerodynamic Vehicle Properties Determined in an Open Jet Wind Tunnel," in SAE International, 2018.

[36] X. Fei, C. Jessing, T. Kuthada, J. Wiedemann and A. Wagner, "The Influence of Different Unsteady Incident Flow Environments on Drag Measurements in an Open Jet Wind Tunnel," Fluids, p. 178, 2020.

[37] J. Sebald, J. Reiß, M. Kiewat and T. Indinger, "Comparison of Time-Resolved Experimental and Numerical Data in the Wake of a Full-Scale Passenger Car," International Journal of Automotive Engineering, vol. 11, no. 4, pp. 185-192, 2020.

[38] J. Sebald, J. Reiss, M. Kiewat and T. Indinger, "Experimental and Numerical Investigations on Time-Resolved Flow Field Data of a Full-Scale Open-Jet Automotive Wind Tunnel," in SAE International, 2021.

[39] E. G. Duell and A. R. George, "Experimental Study of a Ground Vehicle Body Unsteady Near Wake," in SAE International, 1999.

[40] D. Sims-Williams, D. Marwood and A. Sprot, "Links between Notchback Geometry, Aerodynamic Drag, Flow Asymmetry and Unsteady Wake Structure," in SAE International, 2011.

[41] D. Barros, J. Borée, B. R. Noack and A. Spohn, "Resonances in the forced turbulent wake past a 3D blunt body," Physics of Fluids, p. 065104 , 2016.

[42] B. R. Gilhome, J. W. Saunders and J. Sheridan, "Time Averaged and Unsteady Near-Wake Analysis of Cars," in SAE International, 2001.

[43] M. Kawakami, O. Murata and K. Maeda, "Improvement in Vehicle Motion Performance by Suppression of Aerodynamic Load Fluctuations," in SAE International, 2015.

[44] B. Bock, "Coherent structures in the wake of a SAE squareback vehicle model," arXiv:2008.03783, 2020.

[45] D. B. Sims-Williams, R. G. Dominy and J. P. Howell, "An Investigation into Large Scale Unsteady Structures in the Wake of Real and Idealized Hatchback Car Models," in SAE International, 2001.

[46] S. Mack, T. Indinger, N. A. Adams and P. Unterlechner, "The Ground Simulation Upgrade of the Large Wind Tunnel at the Technische Universität München," in SAE International, 2012.

[47] G. Wickern and N. Lindener, "The Audi Aeroacoustic Wind Tunnel: Final Design and First Operational Experience," in SAE International, 2000.

[48] A. I. Heft, T. Indinger and N. A. Adams, "Introduction of a New Realistic Generic Car Model for Aerodynamic Investigations," in SAE International, 2012.

[49] S. Ahmed, G. Ramm and G. Faltin, "Some Salient Features Of The Time-Averaged Ground Vehicle Wake," in SAE International, 1984.

[50] S. Mack, T. Indinger, N. A. Adams, S. Blume and P. Unterlechner, "THE INTERIOR DESIGN OF A 40% SCALED DRIVAER BODY AND FIRST EXPERIMENTAL RESULTS," in Proceedings of the ASME 2012 Fluids Engineering Summer Meeting, 2012.

[51] F. Wittmeier and T. Kuthada, "Open Grille DrivAer Model - First Results," in SAE International, 2015.

[52] B. Hupertz, L. Krueger, K. Chalupa, N. Lewington, B. Luneman, P. Costa, T. Kuthada and C. Collin, "Introduction of a New Full-Scale Open Cooling Version of the DrivAer Generic Car Model," Progress in Vehicle Aerodynamics and Thermal Management, pp. 35-60, 5 December 2017.

[53] J. Reiss, J. Sebald, L. Haag, V. Zander and T. Indinger, " Experimental and Numerical Investigations on Isolated, Treaded and Rotating Car Wheels," in SAE International, 2020.

[54] A-TECH INSTRUMENTS LTD., "ESP-32HD, Miniature Pressure Scanner," [Online]. Available: https://www.a-tech.ca/Product/Series/128/ESP-32HD˙Miniature˙Pressure˙Scanner/?tab=1. [Accessed 8 February 2022].

[55] DMT Druckmesstechnik GmbH, "DTC INITIUM SYSTEM," [Online]. Available: https://dmt-gmbh.com/produkt/dtc-initium-system/. [Accessed 8 February 2022].

[56] MKS Instruments, "MKS Type 670B High Accuracy Signal Conditioner," [Online]. Available: https://www.mksinst.com/mam/celum/celum˙assets/resources/670Bman.pdf. [Accessed 11 February 2022].

[57] MKS Instruments, "Differential Pressure Transducer, 45C, 100 Torr, 0.05%, Unidirectional," [Online]. Available: https://www.mksinst.com/p/698A12TRA. [Accessed 11 February 2022].

[58] SET GmbH - Smart embedded Technologies, "SET Pressure Modules," [Online]. Available: https://www.smart-e-tech.de/en/products/crio-modules/set-pressure-modules/. [Accessed 9 February 2022].

[59] Dantec Dynamics, "MiniCTA and Multichannel CTA - Solution Sheet," [Online]. Available: https://www.dantecdynamics.com/wp-content/uploads/2020/03/0560˙v1-1˙SS-MiniCTA-Multichannel-CTA-systems.pdf. [Accessed 9 February 2022].

[60] S. Becker, Lokale Messverfahren und deren Anwendung zur Bestimmung der Stroemungs- und Turbulenzeigenschaften wandgebundener Stroemungen, Erlangen: Friedrich-Alexander-Universität Erlangen-Nürnberg, 2009.

[61] P. Spalart, W.-H. Jou, M. Strelets and S. Allmaras, "Comments on the Feasibility of LES for Wings, and on a Hybrid RANS/LES Approach," in Advances in DNS/LES, 1997.

[62] F. R. Menter and M. Kuntz, "Adaptation of Eddy-Viscosity Turbulence Models to Unsteady Separated Flow Behind Vehicles," Springer, 2004.

[63] P. R. Spalart, S. Deck, M. L. Shur, K. D. Squires, M. K. Strelets and A. Travin, "A new version of detached-eddy simulation, resistant to ambiguous grid densities," Springer, 2006.

[64] P. R. Spalart and S. R. Allmaras, "A one-equation turbulence model for aerodynamic flows," in AIAA 30th Aerospace Sciences Meeting and Exhibit, 1992.

[65] T.-H. Shih, L. A. Povinelli, N.-S. Liu and K.-H. Chen, "Generalized Wall Function for Complex Turbulent Flows," in 38th Aerospace Sciences Meeting and Exhibit, 2000.

[66] P. R. Spalart, "Detached-Eddy Simulation," Annual Review of Fluid Mechanics, no. 41, pp. 181-202, 2009.

[67] ESI-OpenCFD, "OpenCFD Release OpenFOAMff v2012 (20 12)," [Online]. Available: https://www.openfoam.com/news/main-news/openfoam-v20-12. [Accessed 11 February 2022].

[68] M. Islam, F. Decker, E. De Villiers, A. Jackson and J. Gines, "Application of detached-eddy simulation for automotive aerodynamics development," in SAE International, 2009.

[69] C. Barbi, D. P. Favier, C. A. Maresca and D. P. Telionis, "Vortex shedding and lock-on of a circular cylinder in oscillatory flow," Journal of Fluid Mechanics, pp. 527-544, 1986.

[70] E. Konstantinidis and C. Liang, "Dynamic response of a turbulent cylinder wake to sinusoidal inflow perturbations across the vortex lock-on range," Physics of Fluids, p. 075102, 2011.

[71] L. H. Feng and J. J. Wang, "Circular cylinder vortex-synchronization control with a synthetic jet positioned at the rear stagnation point," Journal of Fluid Mechanics, pp. 232-259, 2010.

[72] Y. Jiang, Y. Chen, W. Xie and H. Friz, "Improvement for the Validation of the Aerodynamic Simulation and Wind Tunnel Test for the FAW-VW T-ROC," in SAE International, 2021.

[73] E. Josefsson, T. Hobeika and S. Sebben, "Evaluation of wind tunnel interference on numerical prediction of wheel aerodynamics," Journal of Wind Engineering & Industrial Aerodynamics, p. 104945, 2022.

[74] B. L. N. Hupertz, C. Mocket, N. Ashton and L. Duan, "Towards a Standardized Assessment of Automotive Aerodynamic CFD Prediction Capability - AutoCFD2: Ford DrivAer Test Case Summary," in SAE International, 2022.

[75] W. Nitsche and A. Brunn, "Geschwindigkeitsmessung," in Strömungsmesstechnik, Berlin, Springer-Verlag, 2006, pp. 50-51.

Appendix

Appendix A: Calibration of the single-wire hot-wire probe

In Figure 89, a calibration curve of the hot-wire probe is depicted. Ten different wind speeds are used to get the calibration curve. In this graph the output voltage of the *MiniCTA* is plotted over the corresponding wind speed. With this curve the parameters of the King's Law [75], which is given in equation (9), can be approximated.

$$U^2=A+Bu^n \tag{9}$$

In this equation U corresponds to the output voltage of the *MiniCTA*, u is the wind speed and A is the square value of the output voltage for no flow over the hot-wire. The parameters B and n must be approximated by fitting the curve to the measured calibration curve. In this case the following values can be derived: A=6.27V², B=2.557V²m/s and n=0.472.

With the determined parameters and the King's Law for all output voltages the corresponding wind speed can be calculated.

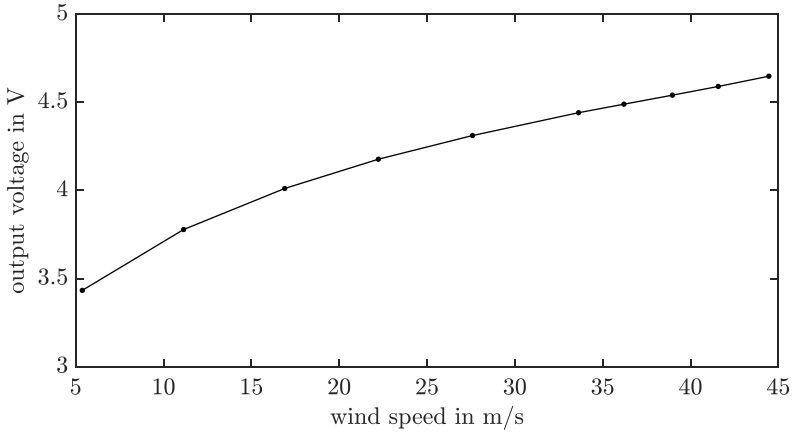

Figure 89: Calibration curve of the single-wire hot-wire probe. Output voltage of the MiniCTA over the wind speed.

Appendix B: Surface Pressure Results of DrivAer Model

In chapter 4.2, the surface pressure of the simplified DrivAer model in the area of the rear window at y=0m is shown to analyse the difference between the numerical and experimental results. The AAWT CFD setup and the AAWT CFD setup with eigenmodes is compared with the experimental wind tunnel result. The remaining surface pressure results at different positions on the vehicle are shown in the following.

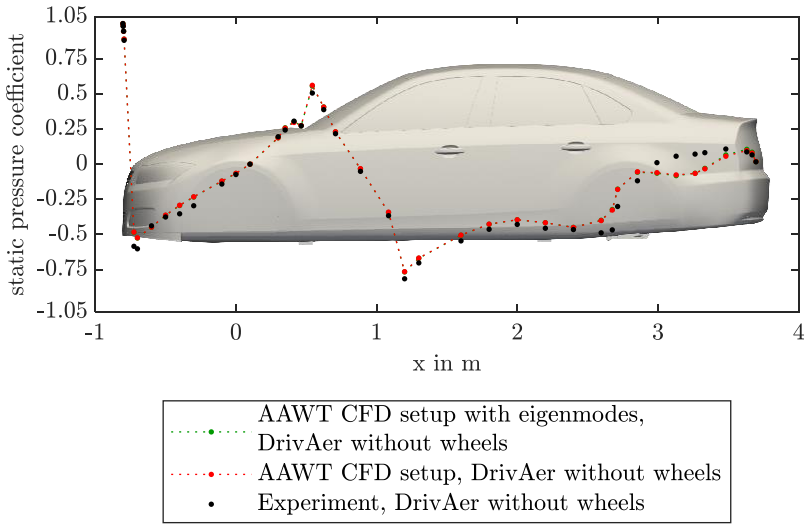

Figure 90: Static pressure distribution on the surface of the DrivAer model without wheels in y=0m on top of the vehicle.

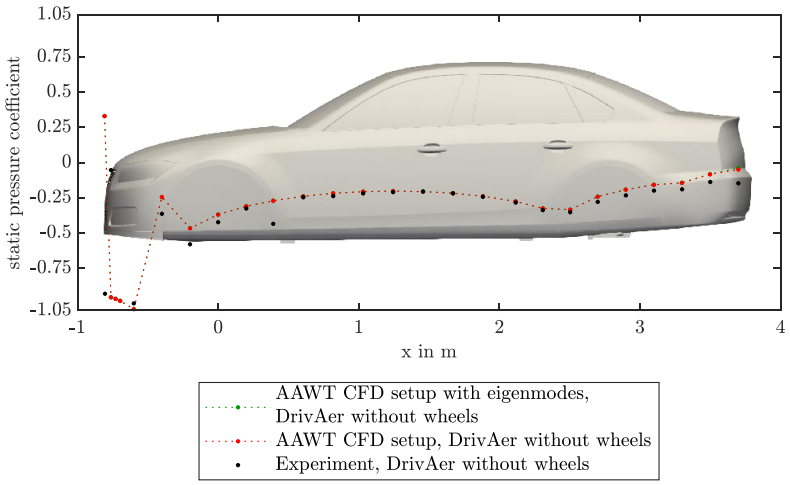

Figure 91: Static pressure distribution on the surface of the DrivAer model without wheels in y=0m on the bottom of the vehicle.

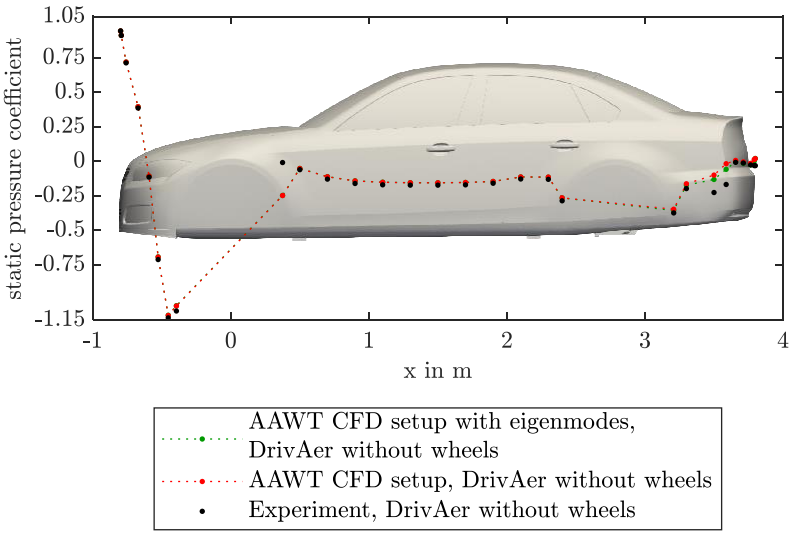

Figure 92: Static pressure distribution on the surface of the DrivAer model without wheels on the left side of the vehicle.